Stony Brook University

Anelastic Behavior of Thermal Spray Coatings and Associated Relationships with Processing Conditions

A Dissertation Presented

by

Yajie Liu

to

The Graduate School

in Partial Fulfillment of the

Requirements

for the Degree of

Doctor of Philosophy

in

Mechanical Engineering

Stony Brook University

August 2007

Stony Brook University

The Graduate School

Yajie Liu

We, the dissertation committee for the above candidate for the
Doctor of Philosophy degree,
hereby recommend acceptance of the dissertation.

Professor Toshio Nakamura, Advisor
Department of Mechanical Engineering

Professor Chad S. Korach, Chair
Department of Mechanical Engineering

Professor Teng-fong Wong, Member
Department of Mechanical Engineering &
Department of Geosciences

Professor Andrew Gouldstone, Outside Member
Department of Materials Science and Engineering

Dr. Curtis A. Johnson, Outside Member
General Electric Company

This dissertation is accepted by the Graduate School

Lawrence Martin
Dean of the Graduate School

Abstract of the Dissertation

Anelastic Behavior of Thermal Spray Coatings and Associated Relationships with Processing Conditions

by

Yajie Liu

Doctor of Philosophy

in

Mechanical Engineering

Stony Brook University

2007

Thermal sprayed ceramic coatings are fabricated with melted or semi-melted particles that solidify on substrates. The successive spray generates a unique lamellar microstructure with pores and cracks. Low-temperature thermal cycling of plasma sprayed zirconia coatings via curvature measurements revealed their in-plane nonlinear behavior. This feature arises from the unique layered, porous and cracked morphology of thermal sprayed ceramic materials. A robust procedure based on an inverse analysis to evaluate nonlinear properties of thermally sprayed ceramic coatings is introduced. Such a method is valuable particularly for thermal sprayed coatings since each may possess unique properties that are dependent on processing conditions. Traditionally, their

responses have been assumed as linear elastic except in very high temperature environments where softening may occur. However, recent inspections revealed their properties to be more accurately characterized as nonlinear elastic. It appears their distinctive morphology consisting of cracks and interfaces are responsible for this behavior. In this work, a versatile procedure to identify the nonlinear constitutive relation of thermally sprayed coatings is developed. First, a suitable stress-strain model is proposed and then a nonlinear bimaterial beam solution is derived. Afterward, an inverse analysis procedure is introduced to process curvature-temperature measurements to extract unknown parameters. Prior to implementing in actual specimens, a detailed simulation study is performed to verify the method's accuracy as well as robustness. This computational analysis closely replicates deposition processes of thermal spray coatings. With successful outcome, the curvature measurements of actual thermal spray yttria stabilized zirconia (YSZ) coatings are used to determine its mechanical properties. The estimated results clearly reveal significant nonlinearity of YSZ coatings. The main advantage of this procedure is that it requires no special specimen preparation and allows continuous measurements after coating deposition. Furthermore the data interpretation does not require complex computational models and calculations such as finite element analysis. This streamlined process make the present method attractive in elucidating various effects associated with thermal spray processing variables. This method is also applicable for extracting parameters of nonlinear films on substrates.

Coating mechanical properties are highly dependent on powder properties and processing parameters during spraying. The properties of powders are expressed by their sizes, morphology and compositions. The spray process parameters control particle

temperature, velocity, plasma power, spray distance, speed and angle. The variations in feedstock size distributions affect not only the particle state but the splat morphology and deposit characteristics as well, different feedstock morphologies give rise to different thermo-mechanical performance of TBCs, and variations in in-flight particle temperature and velocity are highly dependent by torch conditions and . The proposed novel method was applied to analyze the effects of different feedstock and processing parameters on ceramic coating nonlinear properties. Results are interpreted in the context of microstructural changes in the plasma sprayed coatings due to differences in particle state upon impact and coating build-up. The implications of this study are significant for thermo-mechanical design of strain-tolerant ceramic coatings in thermal barrier applications. Desired or specific properties can be obtained by varying powders and processing parameters.

From curvature measurements during thermal cycles, some specimens exhibit clearly different paths during heating and cooling phases. This cyclic hysteresis is likely to be caused by crack face sliding and associated frictions, and the properties of thermal sprayed ceramic coatings are more accurately described as ‘anelastic’. In the present study, the mechanisms of such behaviors were studied from curvature-temperature measurements, analytical analysis and finite element simulation through modeling the microstructure of YSZ coating. Computational models contain numerous distributed microcracks with various sizes, aspect ratios, locations and orientations. The effects of such attributes of microcracks on coating anelastic behavior were studied by the simulations of curvature change during thermal cycles.

To my parents and my husband

For their endless love and support

Table of Contents

List of Figures

List of Tables

Acknowledgements

The road to pursue a doctoral degree in graduate school has been an unforgettable journey for me during the past five years. I am deeply grateful to my advisor, Professor Toshio Nakamura, who leads me to the world of Solid Mechanics and always encourage me to conduct an independent and creative research. His broad knowledge and creative passion in science and engineering are invaluable to the success of my research projects and will definitely benefit me greatly in my future careers. He is not only excellent scientists but compassionate humans with a genuine concern for the well being of his students. Besides my advisor, I would like to thank the rest of my dissertation committee, Professor Chad Korach, Professor Teng-fong Wong, Professor Andrew Gouldstone and Dr. Curtis A. Johnson, who gave me insightful comments and reviewed my work on a very shot of notice. Special thanks go to Professor Sanjay Sampath, Professor Andrew Gouldstone and Dr. Vasudevan Srinivasan in the Department of Material Science and Engineering for the close collaboration and helpful discussions during my research. I would also like to thank all the faculty and staff in the Department of Mechanical Engineering, for their help with my studies and financial support from NSF GOALI-FRG program under award CMMI 0605704 and US Army Research Office.

These years at the Computational Mechanics Lab and Thermal Spray Center have left me so many wonderful memories. I am indebted to my senior colleagues: Dr. Yu Gu, Dr. Zhiqiang Wang, Dr. Pavankiran Vaddadi, Dr. Bhavesh Girish Kumar, Dr. Yuhong Wu, Dr. Anirudha Vaidya, for their generous help. I also want to thank all my fellow group colleagues: Narayanan Ramanujam, Jian Yao, Weiguang Chi, Brian Choi, Swet Chandan,

Prasad Dixit and many others, for their care, support and friendship.

Last, but far from the least, I would like to thank my husband Yuan Ji, for his love, understanding, support, and sacrifice during my graduate study; my parents, my sister and my brother, for their unconditional support and encouragement to pursue my interests in science through the years. This dissertation is dedicated to them.

To all of you, thank you.

Chapter 1

Introduction

1.1 Background and Motivation

Thermal sprayed ceramic coatings are employed in many industrial applications, including aerospace, transportation, petrochemical, electronics and medical applications. The coatings provide a variety of surface protections against high temperature, wear, corrosion, oxidation, and electrical conduction. They are fabricated with melted or semi-melted particles that solidify rapidly on substrates surfaces. The successive spray generates a unique lamellar microstructure with pores and cracks. The rapid solidification causes lamellar microstructure to form and many defects such as pores are generated. Cracks also form during initial cool down when thermal stresses are generated by thermal expansion mismatch with substrate. The microstructure of ceramic coating is characterized as the lamellae splats exist with interlamellar and globular pores, inter-splat and intra-splat microcracks. These geometrical attributes make the TS coating's stiffness to be much lower than that of bulk material. With the increasing engineering applications, coating reliability is critical to ensure their designed performances. The coating's properties, such as stress strain relation, thermal conductivity and residual stresses, are key factors in understanding coating's reliability (Kesler et al., 1998).

In-situ substrate-curvature measurement is an effective technique to determine coating's mechanical properties. This technique was introduced on the premises that both coating and substrate deform linearly, which enables the use of well-known bi-material

curvature-temperature formula to identify the elastic modulus as well as the residual stress of coating. Many thermally sprayed materials such as molybdenum indeed exhibit linear responses that justify the applicability of technique (Matejicek et al., 2003). However, recent studies revealed that curvature-temperature measurements of some ceramics do not exhibit linear behavior. These include yittria-stabilized zirconia (YSZ) and alumina (Al_2O_3) that are frequently chosen for thermal barrier applications. At first, the nonlinearity was thought to be the result of partial debonding between coating and substrate or measurement inconsistency during thermal cycle. However after careful inspections, it was confirmed that the coatings themselves indeed display nonlinear responses. In general, its modulus decreases with increasing stress. Note that the maximum temperatures in the tests were kept less than 250^{o}C, which is well below the temperatures when property changes are expected to occur in ceramics.

The source of nonlinearity appears to arise from unique microstructural attributes of thermally sprayed ceramic coatings. As many micro-cracks and weak interfaces are present in the coatings, their opening/closing and sliding during stress changes promote the nonlinear responses. Under sufficient compressive load, crack faces are closed and the coatings exhibit higher apparent stiffness while opened cracks under tensile state produce more compliant response (Kroupa et al., 1999, 2002). Since microcracks have various orientations/sizes and different local stresses, closings and openings do not occur simultaneously. This results in a smooth variation of effective modulus rather than a sudden change expected from a single crack model. At room temperature, high residual compressive stress keeps many cracks to be closed. The nonlinear behaviors of atmospheric plasma sprayed (APS) ZrSiO4 were also observed under four-point bend tests

(Harok et al., 2001). The mechanical behavior is elastic because ceramics generally do not exhibit plasticity at room temperature. Similar phenomenon is found by Eldridge (2002) that plasma sprayed YSZ coatings exhibit nonlinear elastic behavior and the modulus increases with applied stress because of coating compaction. Another bend test combined with strain analysis reported increasing in-plane stiffness of YSZ coatings with compressive stress while decreasing stiffness decrease under larger tensile stress (Wakui, et. al., 2004). Waki, et al. (2004) also reported the nonlinear stress-strain responses of plasma sprayed zirconia coating using the laser speckle strain-displacement gauge (SSDG). Wang et al. (2006) observed nonlinear stress-strain relation of thermally sprayed metallic Ni–45Cr coating under tensile loading along the through-thickness direction due to its lamellar features.

Although it is well understood that desired or application-specific microstructures can to a first approximation be obtained by varying feedstock powder and processing parameters, a quantitative description in terms of properties has yet to be satisfactorily achieved. Kroupa and co-workers Kroupa (1999, 2002) built physical models relating theoretical defect geometries to macroscopic non-linear mechanical response. Though a number of studies have elucidated nonlinear behavior of thermally sprayed ceramic coatings, relation of such reasoning to process variation, or put simply, a robust method of comparison of different TS coatings, needs to be developed.

Thermal spray is a well established processing technology for the fabrication of thick coatings of ceramics and metals onto a variety of substrates. These coatings are used extensively as protective layers against wear, high temperature and other harsh conditions. TS ceramic coatings are produced through successive impingement of molten

droplets on a prepared substrate resulting in a lamellar microstructure with pores and cracks. Accordingly, coating mechanical properties are highly dependent on the defect architecture of the coating and thus strongly related to the complex deposition processes and related processing conditions (Brinkiene et al., 2004; Deshpande et al., 2004; Friis et al., 2001; Kadolkar et al., 2002, 2003; Kweh et al., 2000; Li et al., 2003; Mawdsley et al., 2001; Montavon et al., 1997; Ning et al., 2006; Sampath et al., 2004; Teixeira et al., 1999; Thangamani et al., 2002; Zhao et al., 2004). For instance in the case of ceramics, the feedstock powder and the processing conditions of particles all affect the nature of the deposit formation dynamics and the ensuing properties of coatings. Although there are many studied of processing conditions effect on properties, most of them focus on the linear elastic properties. Therefore the investigation of the effects on processing parameters on coating nonlinear properties is very important for process control. And also it turns out that such studies are extremely useful for achieving the repeatability of coating fabrication and the reliability process system.

Current substrate-curvature tests show ceramic coatings exhibit a nonlinear mechanical behavior and the mechanical properties depend on the amplitude of applied stress or strain. Curvature measurements have also revealed that thermally sprayed ceramic coatings exhibit hysteresis during stress cycling. The stress strain relations tend to be different under cyclic loading but after unloading the strain can be fully reversed. It appears crack face frictions are responsible for this phenomenon. These nonlinear and hysteresis behavior of thermal spray coatings can be characterized as anelastic behavior

1.2 Organization of the Dissertation

In chapter 2, the detail process of substrate curvature measurements is given and

the experimental results are shown. The anelastic behavior including nonlinearity and hysteresis behavior can be clearly seen from the measurements.

In chapter 3, a novel procedure based on a nonlinear beam model and an inverse analysis is proposed to estimate the nonlinear stress-strain relations of thermal spray ceramics coatings. Essentially this method extracts the best estimates of unknown parameters from curvature-temperature measurements obtained during thermal cycles. It is based on inverse analysis and curvature measurement and is presented to estimate nonlinear mechanical property of thermal sprayed YSZ coating. This technique is attractive since it does not require complex set-up or lengthy data interpretation. More importantly, it is possible to make correct interpretations of measured curvature temperature records. Previously, the nonlinear record made even the extraction of linear elastic modulus uncertain.

In chapter 4, the proposed nonlinear properties characterization technique is used to extract nonlinear elastic coating properties by inverse analysis of substrate curvature measurements during thermal cycling. Then, the results of such analyses are presented results on a range of plasma sprayed YSZ coatings, obtained from a number of different processing conditions, and interpreted in the context of defect architecture. This work has important implications for both coating design as well as performance reliability.

Finally in chapter 5, the mechanism that governs anelastic behavior of YSZ ceramic coatings is elucidated with experimental data, analytical models and finite element analysis. The similar nonlinearity and hysteresis of curvature as measured in experiments are simulated by finite element modeling.

1.3 References

Brinkiene, K. and Kezelis, R. (2004), "Correlations between processing parameters and microstructure for YSZ films produced by plasma spray technique", *Journal of the European Ceramic Society*, 24 (6), 1095-1099.

Deshpande, S., Kulkarni, A., Sampath, S. and Herman, H., (2004). "Application of image analysis for characterization of porosity in thermal spray coatings and correlation with small angle neutron scattering", *Surface and Coatings Technology,* 187(1), 6-16.

Eldridge, J.I., Morscher, G.N.and Choi, S.R., (2002), "Quasistatic vs. dynamic modulus measurements of plasma- sprayed thermal barrier coatings", *Ceramic Engineering and Science Proceedings* 23, 371-378.

Friis, M., Persson, C. and Wigren, J. (2001), "Influence of particle in-flight characteristics on the microstructure of atmospheric plasma sprayed yttria stabilized ZrO_2", *Surface and Coatings Technology,* 141 (2-3), 115-127.

Kadolkar, P. and Dahotre, N. B. (2002), "Variation of structure with input energy during laser surface engineering of ceramic coatings on aluminum alloys", *Applied Surface Science,* 199 (1-4), 222-233.

Kadolkar, P. and Dahotre, N.B. (2003), "Effect of processing parameters on the cohesive strength of laser surface engineered ceramic coatings on aluminum alloys", *Materials Science and Engineering A,* 342 (1-2), 183-191.

Kroupa, F., Dubsky, J., (1999). "Pressure dependence of Young's moduli of thermal

sprayed materials". *Scripta Materialia* 40 (11), 1249-1254.

Kroupa, F., Plesek, J., (2002). "Nonlinear elastic behavior in compression of thermally sprayed materials". *Materials Science and Engineering A*, 328, 1-7.

Kweh, S. W. K., Khor, K. A. and Cheang, P. (2000), "Plasma-sprayed hydroxyapatite (HA) coatings with flame-spheroidized feedstock: microstructure and mechanical properties", *Biomaterials,* 21 (12), 1223-1234.

Li. M. and Christofides, P. D. (2003), "Modeling and analysis of HVOF thermal spray process accounting for powder size distribution". *Chemical Engineering Science,* 58 (3-6), 849-857.

Matejicek, J., Sampath, S., (2003). "In situ measurement of residual stresses and elastic moduli in thermal sprayed coatings: Part 1: apparatus and analysis". *Acta Materialia* 51, 863-872.

Matejicek, J., Sampath, S., Gilmore, D., Neiser, R., (2003). "In situ measurement of residual stresses and elastic moduli in thermal sprayed coatings: Part 2: processing effects on properties of Mo coatings". *Acta Materialia* 51, 873-885.

Mawdsley, J. R., Su, Y. J., Faber, K. T. and Bernecki, T. F. (2001), "Optimization of small-particle plasma-sprayed alumina coatings using designed experiments". *Materials Science and Engineering A*, 308 (1-2), 189-199.

Montavon, G., Sampath, S., Berndt, C.C., Herman, H. and Coddet, C. (1997), "Effects of the spray angle on splat morphology during thermal spraying". *Surface and Coatings*

Technology, 91 (1-2), 107-115.

Ning, X., Li, C., Li, C., and Yang, G., (2006), "Effect of powder structure on microstructure and electrical properties of plasma-sprayed 4.5 mol% YSZ coating", *Vacuum,* 80 (11-12), 1261-1265.

Sampath, S., Jiang, X. Matejicek, J., Prchlik, L., Kulkarni, A. and Vaidya, A. (2004) "Role of thermal spray processing method on the microstructure, residual stress and properties of coatings: an integrated study for Ni–5 wt.%Al bond coats", *Materials Science and Engineering A,* 364, 216-231.

Teixeira, V., Andritschky, M., Fischer, W., Buchkremer, H. P., Stover, D., (1999). "Effects of deposition temperature and thermal cycling on residual stress state in zirconia-based thermal barrier coatings". *Surface and Coatings Technology* 120-121, 103-111.

Thangamani, N., Chinnakali, K., and Gnanam, F. D. (2002), "The effect of powder processing on densification, microstructure and mechanical properties of hydroxyapatite". *Ceramics International* 28, 355-362.

Zhao, L. Maurer, M., Fischer, F., Dicks, R. and Lugscheider, E., (2004), "Influence of spray parameters on the particle in-flight properties and the properties of HVOF coating of WC-CoCr", *Wear,* 257(1-2), 41-46.

Wakui, T., Malzbender, J. and Steinbrech, R.W., (2004), Strain analysis of plasma sprayed thermal barrier coatings under mechanical stress, *Journal of Thermal Spray and Technology* 13(3), 390-395.

Wang, W., Li, C., Wang, Y., Yang, G., Sonoya, K., (2006), “Tensile deformation behavior of plasma-sprayed Ni-45Cr coatings”, *Surface and Coatings Technology* 201(3-4), 842-847.

Chapter 2

Substrate Curvature Measurements

2.1. Background

A thermal cycle test to measure curvature change is an effective method to estimate an unknown modulus of coating or thin film. The curvature measurement to determine properties of thin films on thick substrate was introduced by Stoney (1909). The substrate-curvature method based on Stoney formula has been was widely used in various applications (e.g., Carlotti et al., 1997; Lacquaniti et al., 1997; Krulevitch et al., 1996; Hunsche et al., 2001; Oka et al., 2003; Menzel et al., 2005). Kuroda et al. (1988, 1990) have also utilized the formula for TS coatings. The simple form of Stoney formula makes determinations of material properties, including nonlinear terms, straightforward. Obviously the limitation of this formula is that the thickness of film or coating must be relative small as compared to that of substrate. For films and coatings that are thick, curvature solutions must be obtained with an alternate method. However as the bimaterial solution for linear elastic materials, if the total thickness (film plus substrate) is still small compared to the specimen length, one can still invoke the beam/plate theory to establish nonlinear curvature formula. Such a formulation is described in Chapter 3.

Although there are other means to measure the modulus of coating attached to a substrate, the curvature measurement under temperature change offers several advantages. First, an inaccuracy associated with measurement error is less than that from tensile tests. For an example, if the modulus ratio of coating over substrate is ~0.40 (close to thermal spray YSZ-Al system) and the thickness of coating is 20% of that of substrate, 1% error in

the displacement measurement under uniaxial tensile test magnifies the error in modulus estimation by 14%. With the curvature test, it would be 6% error. Second, the thermal loading produces more uniform stress state within the coating than that under mechanical load. For an example, with three-point-bend test, local stress concentrations and associated measurement errors at the loading points are inevitable. Obviously near-uniform stress and deformation states are more ideal for property measurements.

Within thermally sprayed coatings, the state of stress evolves as follows (Matejicek et al., 2003; Tsui et at., 1997). During deposition to fabricate the coating, molten particles strike onto a substrate or previous splats (solidified particles) and immediately cool down. As their temperatures rapidly drop and solidify, high quenching stresses develop. These non-equilibrium thermal conditions produce an overall tensile state within the coating. At the end of deposition, the large tensile stresses in the coating cause sizable curvature in the coating-substrate specimen. However as both coating and substrate cool down to the room temperature, their mismatch in thermal expansion coefficients (CTE) generates additional thermal stresses. Since CTE of ceramic coating is generally less than that of metallic substrates, the cooling down tends the coatings to be more compressive. The net stress state at the room temperature depends on the actual CTE's of coating and substrate. For YSZ-Al systems, due to the large CTE difference, the overall or net stresses within the coating are usually compressive although locally tensile stress states may remain within solidified splats. The magnitude of residual stress also depends on the preheating temperature of substrate, substrate and coating thicknesses and other spray process parameters (e.g., powder, powder sizes, particle temperature and velocity).

Measurement of substrate curvature during thermal cycling is a well-established method to extract mechanical properties of thin films and thick and/or graded coatings. Briefly, the bilayer film-substrate system is subjected to a temperature excursion ΔT that imposes thermal mismatch strain in the film. The resulting film stress depends on the constitutive properties, and the unbalanced force (stress integrated through film thickness) causes substrate curvature $\Delta\kappa$. For sufficiently thin films and coatings, it may be shown that stress in the film is uniform through-thickness and the general expression for beam bending due to intrinsic film stress may be simplified to the Stoney formula (Stoney, 1909). For thicker specimens (as is the case here), the curvature solutions must be obtained with an alternate method. If both coating and substrate are linear elastic, the curvature change during spraying and cooling can be expressed as (Tsui and Clyne, 1997)

$$\Delta\kappa = \frac{6E_s E_c ht(h+t)\Delta\alpha\Delta T}{E_s{}^2h^4 + E_c{}^2t^4 + 2E_s E_c ht\left(2h^2 + 3ht + 2t^2\right)} \tag{2.1}$$

Here, t and h are the thickness of film/coating and substrate respectively, and E_s and E_c are the elastic modulus of the substrate and coating, respectively. Also $\Delta\alpha$ is the difference of thermal expansion coefficients of substrate α_s and film/coating α_c, and ΔT is the temperature change. The above equation with measured $\Delta\kappa$–ΔT record is used to determine the coating modulus E_c (via the quadratic formula). Further complications arise if the coating has nonlinear elastic properties, a different formulation is necessary to determine the unknown properties as described in chapter 3.

2.2. Experimental Procedure

Figure 2.1 shows a schematic of the substrate curvature test and salient points are described here (Matejicek et. al., 2003). The method uses non-contact laser based

displacement sensing on the backside of a substrate, with a resolution of a few microns; multiple laser displacement sensors allow for precise extraction of the radius of curvature. In addition, the temperature of the substrate is also monitored through multi-point temperature sensing using thermocouples attached to the substrate. Typical in-plane dimensions of specimens are 230mm × 25.4mm. The thickness of coating varies (via experimental design), t = 250~800μm while that of substrate is about h = ~3mm. The original device was used to examine curvature changes during spraying and post-spray cool down to extract residual stresses and elastic modulus of metallic and ceramic coatings. However, the YSZ coating post-deposition continues to exhibit transient microcracking phenomena and as such the cooling curve from deposition was unsuitable for nonlinear data extraction. To achieve this, the coating-substrate system is further heated by passing a hand torch (usually MAPP gas) multiple time over the coating and is left to cool under the forced air convection. Typically it takes 2 minutes to heat up and about 7 minutes to cool down. There are large fluctuations of curvature measurements while the specimen is heated, produced by the moving of hand-held flame torch. Subsequently, the far less noisy measurements during the cool down period are used in our analysis. Furthermore, at the initial phase of cool down, the temperature within the specimen is still not uniform as it takes about 2~3 seconds to reach the thermal equilibrium across the entire length of specimen. Thus the measurements obtained during the first few seconds of cooling (about 30^{o}C drop) are discounted.

In this investigation, YSZ coatings were plasma-sprayed under different conditions on Al 6061 substrates, and subjected to thermal cycling as described above. Figure 2.2 shows one typical curvature-temperature plot during cycling from room

temperature to 320°C. The thickness of this coating is 764μm while that of substrate is 3.4mm. At the onset of heating, the coating is in compression due to the mismatch in the coefficients of thermal expansion (CTE), and the initial curvature κ_R at the room temperature T_R is non-zero. As the specimen is heated during the thermal cycle, the coating stress tends to be tensile and the curvature shifts its sign as shown in the figure. Here, the zero-curvature is denoted as κ_o and the corresponding temperature is denoted as T_o. A notable characteristic of this data is the obvious nonlinear dependence of curvature with temperature. The fluctuation of curvature during heating is caused by the moving torch and the transient heat transfer effect. The curve is steeper at lower temperature, suggesting a higher stiffness in this region. Since the properties of YSZ are not thermally dependent in this temperature range, the nonlinearity is likely to be driven by geometrical/microstructural attributes, and affected by the stress state (i.e., tension vs. compression) of the coatings. Although curvature-temperature behavior is for the most part elastic, some specimens exhibit clearly different paths during heating and cooling phases shown in Figure 2.3. The thickness of this coating is 277μm while that of substrate is 3.19mm. The feedstock is Agglomerated and Sintered (AS) powder and it was sprayed at average velocity of 79m/s and particle temperature of 2,736°C. This cyclic hysteresis is likely to be caused by crack face sliding and associated frictions, and the properties of thermal spray ceramics are more accurately described as 'anelastic'.

2.3. References

Carlotti, G., Doucet, L., Dupeux, M., (1997), "Elastic properties of silicon dioxide films deposited by chemical vapour deposition from tetraethylorthosilicate". *Thin Solid Films* 296, 102-105.

Hunsche, B., Vergöhl, M., Neuhäuser, H., Klose, F., Szyszka, B., Matthée, T., (2001), "Effect of deposition parameters on optical and mechanical properties of MF- and DC-sputtered Nb_2O_5 films", *Thin Solid Films* 392(2), 184-190.

Krulevitch, P., Ramsey, P. B., Makowiecki, D. M., Lee, A. P., Northrup, M. A., Johnson, G. C., (1996), "Mixed-sputter deposition of Ni-Ti-Cu shape memory films". *Thin Solid Films* 274, 101-105.

Kuroda, S., Fukushima, T., Kitahara, S., (1988), "Simultaneous measurement of coating thickness and deposition stress during thermal spraying", *Thin Solid Films,* 164, 157-163.

Kuroda, S., Fukushima, T., Kitahara, S., (1990), "Generation mechanisms of residual stresses in plasma-sprayed coatings", *Vacuum* 41, 1297-1299.

Lacquaniti, V., Monticone, E., Picotto, G. B., (1997), "Structural and surface properties of sputtered Nb films for multilayer devices", *Surface Science,* 377-379, 1042-1045.

Matejicek, J., Sampath, S., (2003), "In situ measurement of residual stresses and elastic moduli in thermal sprayed coatings: Part 1: apparatus and analysis", *Acta Materialia* 51, 863-872.

Matejicek, J., Sampath, S., Gilmore, D., Neiser, R., (2003), "In situ measurement of residual stresses and elastic moduli in thermal sprayed coatings: Part 2: processing effects on properties of Mo coatings", *Acta Materialia* 51, 873-885.

Menzel, S., Strehle, S., Wendrock, H., Wetzig, K., (20050, "Effect of Ag-alloying addition on the stress–temperature behavior of electroplated copper thin films" *Applied Surface Science* 252, 211-214.

Oka, Y., Tao, M., Nishimura, Y., Azuma, K., Fujiwara, E., Yatsuzuka, M., (2003), "Properties of thick DLC films prepared by plasma-based ion implantation and deposition using combined RF and H.V. pulses", *Nuclear Instruments and Methods in Physics Research* B 206 700-703.

Stoney, G., (1909), "The tension of metallic films deposited by electrolysis", *Proc Roy Soc London* A82, 172-175.

Tsui, Y.C. and Clyne, T.W., (1997), "An analytical model for predicting residual stresses in progressively deposited coatings Part 1: Planar geometry", *Thin Solid Films* 306, 23-33.

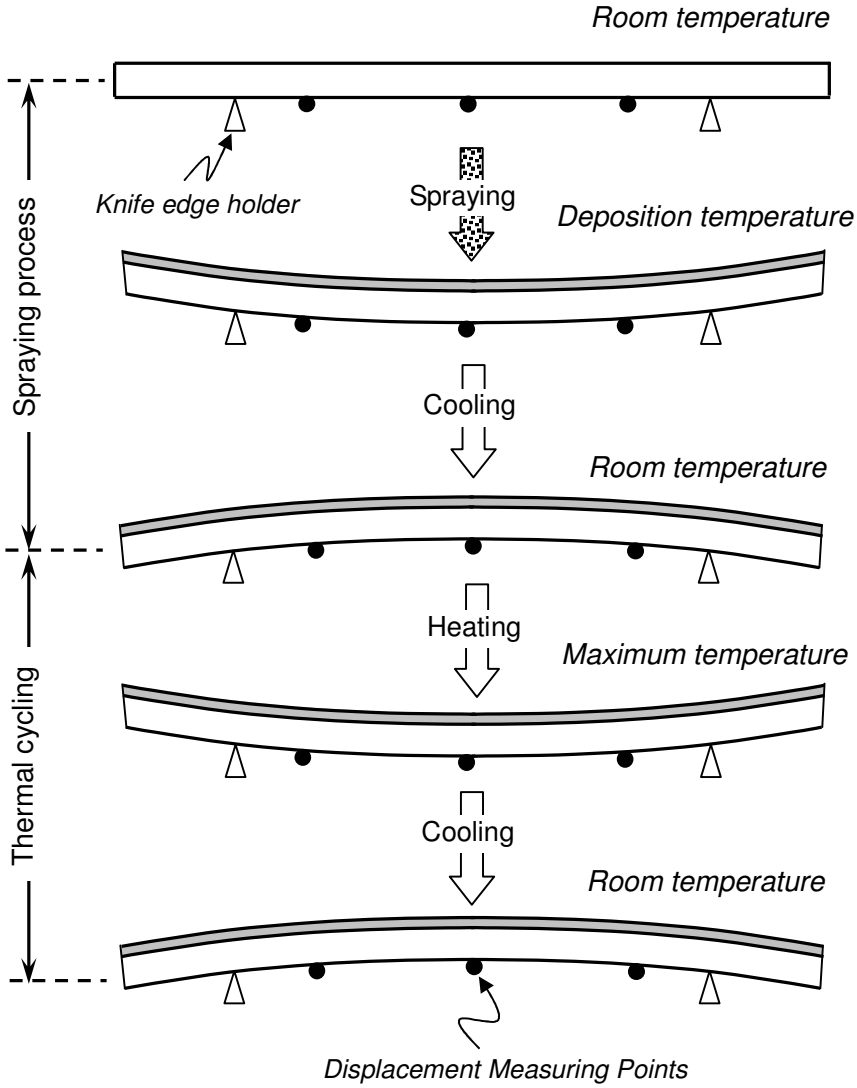

Figure 2.1 Schematic of curvature change as coating and substrate is thermally sprayed and thermal cycled.

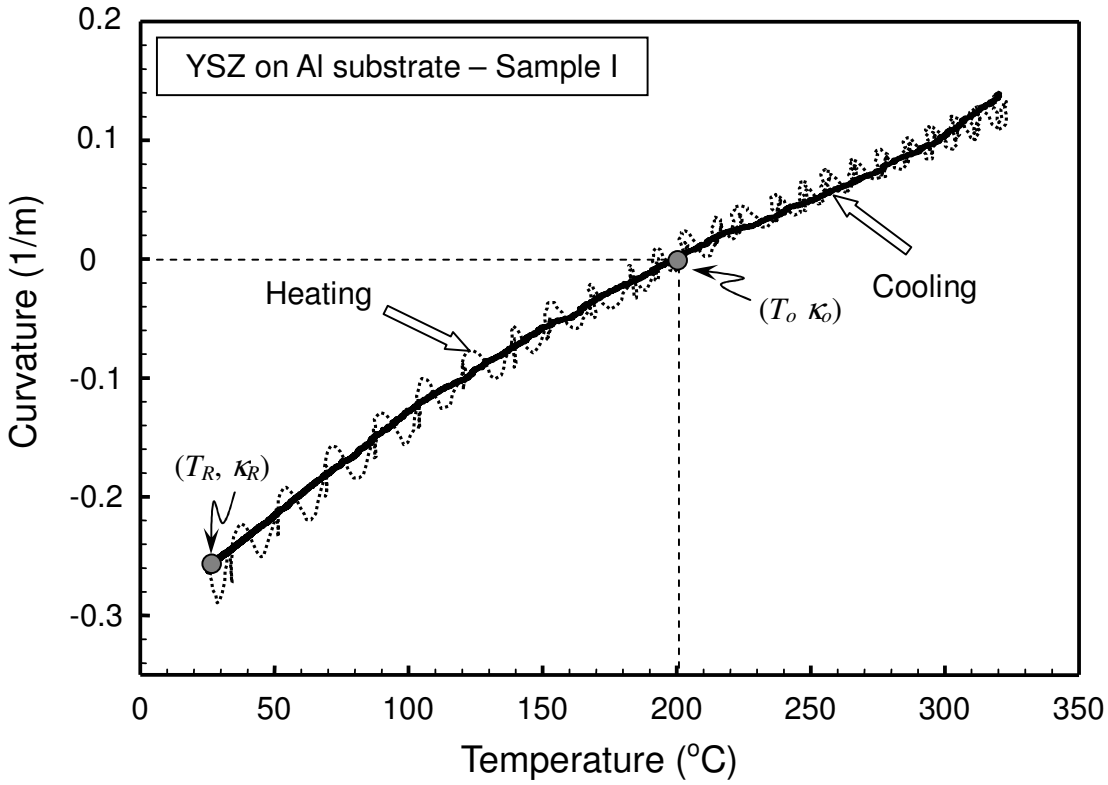

Figure 2.2 Measured curvature during thermal cycle of YSZ coating on Al substrate – Sample I. The heating curvature is shown in dash while the cooling curvature is shown in dark solid curve. Here to denote the temperature when the curvature is zero κ_o. Also κ_R is the room temperature curvature.

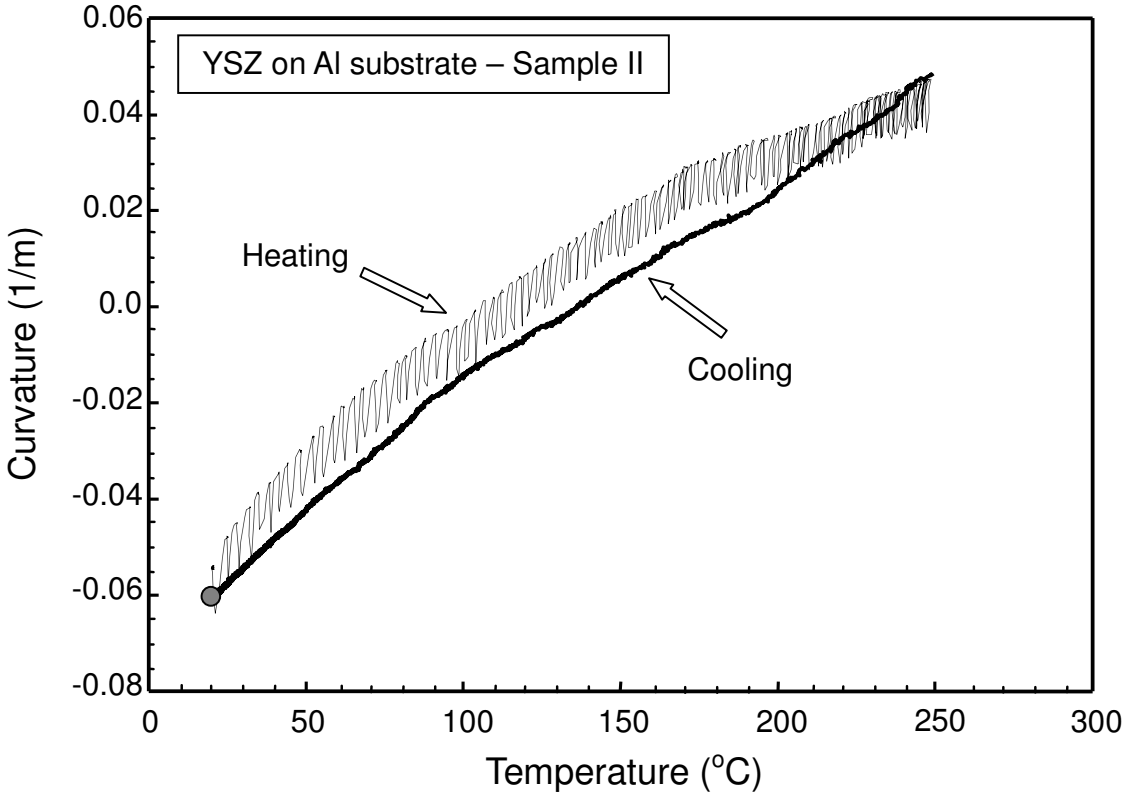

Figure 2.3 Measured curvature during thermal cycle of YSZ coating on Al substrate –Sample II. The heating curvature is shown in dash while the cooling curvature is shown in dark solid curve.

Chapter 3

Identification of Nonlinear Property

3.1. Constitutive Model

In order to describe the coating's nonlinear behavior, a phenomenological constitutive model is introduced. First, based on the experimental observations and likely physical causes of nonlinearity (cracks and defects), the stress-strain relation is expected to be asymmetric under tension and compression. Second, under very large compression, the response should be nearly linear since many cracks and thin defects are closed. Third, the transitions from linear to nonlinear generally do not occur at the zero stress ($\sigma = 0$). With these factors, the following uniaxial stress-strain model is proposed.

$$\varepsilon = \begin{cases} \dfrac{\sigma}{E} - \dfrac{\left|\sigma_T\right|^n}{E\sigma_N^{n-1}} & \text{for} \quad \sigma < \sigma_T \\ \dfrac{\sigma}{E} + \dfrac{(\sigma - \sigma_T)^n - \left|\sigma_T\right|^n}{E\sigma_N^{n-1}} & \text{for} \quad \sigma \geq \sigma_T \end{cases} \tag{3.1}$$

Here the transitional stress σ_T corresponds to the change from linear to nonlinear relations, generally negative (i.e., $\sigma_T < 0$). Note if $\sigma_T = 0$, the relation simplifies to $\varepsilon = (\sigma/E) + (\sigma^n/E\sigma_N{}^{n-1})$ under tension, which represents a combination of linear elastic and modified Ramberg-Osgood model. It is important to note that due to the nature of TS coating microstructures, it is expected that there is no clear "transition" from linear to nonlinear regimes since some cracks continue to close below σ_T. Also E is the Young's modulus, n is the power-law exponent and σ_N is a reference stress. A small value of σ_N signifies a higher degree of nonlinearity while $\sigma_N \to \infty$ for a linear elastic.

The schematic of stress-strain curve according to (3.1) is shown in Figure 3.1. Here the stress-strain axes ($\sigma^*-\varepsilon^*$) centered at $\sigma = \sigma_T$ separate the linear and nonlinear regimes. This relation turns out to be very versatile to describe the stress-strain behavior of thermal spray coatings with minimum number of parameters (E, σ_N, n and σ_T). Under multi-dimensional condition (e.g., plate bending), the Poisson's ratio ν is also required. Also note E is appropriately described as the *elastic tangent modulus* near room temperature since it is not the modulus at $\sigma = 0$. We have used a number of measured data to examine the suitability of the proposed material model. Other, perhaps more refined, forms of stress-strain relation describing the mechanical behavior of TS coatings are also possible but they would require more parameters to define the relation.

3.2. Nonlinear Bimaterial Beam Solution

To extract material parameters of many specimens, a robust procedure, without requiring large-scale computations such as a finite element analysis, is needed. Here the formulation for nonlinear bimaterial beam solution is described. This procedure is straightforward, yet the derivation is rather complex due to shifting of the neutral axis as stress changes (unlike linear elastic model). Furthermore, although there have been studies on large deformation effects on beams and plates (e.g., Finot and Suresh, 1996), we were not able to find solutions for the nonlinear elastic bimaterial beams.

Suppose a bimaterial specimen consists of a nonlinear elastic coating and linear elastic substrate as shown in Figure 3.2. The axial strain within the coating under temperature change ΔT is,

$$\varepsilon_c(y) = -\Delta\kappa(y - y_o) + \alpha_c \Delta T + \frac{F_{mis}}{bE_c^* t} \quad . \tag{3.2}$$

Here $\Delta\kappa$ is the curvature change under temperature variation ΔT, α_c is the coefficient of thermal expansion, y_o is the location of neutral axis, F_{mis} is the mismatch force needed to equilibrate thermal expansions of coating and substrate, t is the coating thickness and E_c^* is the secant modulus defined as $E_c^* = \sigma_c/\varepsilon_c^m$. Also σ_c is the axial stress and ε_c^m is the mechanical strain (i.e., $\varepsilon_c^m(y) = \varepsilon_c(y) - \varepsilon_c^{\text{therm}}$) in the coating. Unlike the linear elastic coatings, the neutral axis shifts with change in the secant modulus as,

$$y_o = \frac{E_s h^2/2 + \int_h^{h+t} E_c^*(y)\, y dy}{E_s h + \int_h^{h+t} E_c^*(y) dy} \quad . \tag{3.3}$$

Here E_s and h are the Young's modulus and thickness of substrate, respectively. The moment M_{mis} (per thickness) generated by the mismatch force F_{mis} can be shown as,

$$\frac{M_{mis}}{b} = \frac{F_{mis}}{b}\left(\frac{h+t}{2}\right) = \frac{E_s E_{ave}^* h\, t}{E_s h + E_{ave}^* t}\left(\frac{h+t}{2}\right)\Delta\alpha\Delta T \ . \tag{3.4}$$

In the above, $\Delta\alpha = \alpha_s - \alpha_c$ and E_{ave}^* is introduced as the average secant modulus through thickness of the coating. The curvature change relates to the moment as $\Delta\kappa = M_{mis}/(EI)_{\text{bimaterial}}$. Here $(EI)_{\text{bimaterial}}$ is the effective flexural composite stiffness which varies with the neutral axis and the secant modulus. With these relations, the curvature change may be expressed as,

$$\Delta\kappa = \frac{\dfrac{E_s E_{ave}^* h\, t}{E_s h + E_{ave}^* t}\left(\dfrac{h+t}{2}\right)\Delta\alpha\Delta T}{E_s h\left(\dfrac{h^2}{3} - h y_o + y_o^2\right) + \int_h^{h+t} E_c^*(y)(y - y_o)^2 dy} \quad . \tag{3.5}$$

Since y_o is not constant during thermal loading, the above formula requires several iterations for a given ΔT. The iteration loops can be reduced by assuming the following form,

$$\Delta\kappa \cong \frac{6E_s E^*_{ave} h\ t(h+t)\Delta\alpha\Delta T}{E_s{}^2 h^4 + E^*_{ave}{}^2 t^4 + 2E_s E^*_{ave} h\ t\left(2h^2 + 3ht + 2t^2\right)}. \tag{3.6}$$

In the above, the secant modulus $E_c{}^*(y)$ in the integral (3.5) is replaced with the average value E^*_{ave}. A similar assumption can be taken for the computation of y_o in (3.3). To further reduce the computational requirement, instead of computing the correct average value, E^*_{ave} can be estimated at the midpoint of coating ($y = h + t/2$) as,

$$E^*_{ave} \cong \frac{\sigma(\varepsilon_c{}^{mid})}{\varepsilon_c{}^{mid}} \quad \text{where} \quad \varepsilon_c{}^{mid} = -\Delta\kappa\left(h + \frac{t}{2} - y_o\right) + \frac{E_s h}{E_s h + E^*_{ave} t}\Delta\alpha\Delta T \tag{3.7}$$

Clearly, the computation of E^*_{ave} still requires multiple iterations. The curvature formula (3.6) for the nonlinear beam appears to be similar to the one given for the linear elastic case (2.1). However, the required computations are very different and the determination of unknown material properties for a given $\Delta\kappa$–ΔT record is not a simple process. First, the axial strain at mid-point is initialized as $\varepsilon = \Delta\alpha\Delta T$ (note $\varepsilon = \varepsilon_c{}^{mid}$). Then the stress is computed via the constitutive equation (3.1) with iterations. Once the average secant modulus and neutral axis are calculated, the curvature can be solved. With this curvature, the strain is updated and the convergence is checked. The iteration is repeated until the required tolerance, generally set as $\Delta\alpha\Delta T/100$, is met. The whole process is shown in Figure 3.3.

In terms of σ^* and ε^* in (3.1), the average modulus is expressed as,

$$E^*_{ave} = \frac{\sigma^*}{\varepsilon^*} = \begin{cases} E_c & \sigma^* < 0 \\ \dfrac{E_c \sigma_0^{n-1}}{\sigma_o^{n-1} + \left(\sigma^*\right)^{n-1}} & \sigma^* > 0 \end{cases} \tag{3.8}$$

Suppose ε^*, E_c, σ_0, and n are known, Newton's method can be used to determine σ^* for a given ε^* under $\sigma^* > 0$. First an implicit function is defined as,

$$f(\sigma^*) = \frac{\sigma^*}{E_c} + \frac{(\sigma^*)^n}{E_c \sigma_0^{n-1}} - \varepsilon^* = 0 \tag{3.9}$$

Then the following iteration is carried out to determine σ^*

$$\sigma_i^* = \sigma_{i-1}^* - \frac{f(\sigma_{i-1}^*)}{f'(\sigma_{i-1}^*)} \text{ where } \quad f'(\sigma_{i-1}^*) = \frac{1}{E_c}\left[1 + n\left(\frac{\sigma_{i-1}^*}{\sigma_0}\right)^{n-1}\right] \tag{3.10}$$

The convergence is satisfied when $\left|\sigma_i^* - \sigma_{i-1}^*\right| < 1\times10^{-3}\sigma_0 / E_c$. Then (3.8) is used to compute E^*_{ave}.

To compute the transition stress σ_T, first the average secant modulus E^T_{ave} between the zero-curvature and the transition point is computed in the following linear bimaterial equation.

$$\frac{6E_s E^T_{ave} h\ t(h+t)\Delta\alpha(T_o - T_T)}{E_s{}^2 h^4 + E^T_{ave}{}^2 t^4 + 2E_s E^T_{ave} h\ t(2h^2 + 3ht + 2t^2)} - (\kappa_o - \kappa_T) = 0 \tag{3.11}$$

Then the following equation is used to solve for the transition stress σ_T.

$$\sigma_T = \sigma_0\left(\frac{E_c}{E^T_{ave}} - 1\right)^{\frac{1}{n-1}} \tag{3.12}$$

To determine the residual stress at room temperature at the mid-point of coating σ_R, the following equation may be used.

$$\sigma_R = E_c(\kappa_R - \kappa_T)\left(h + \frac{t}{2} - y_o\right) + \frac{E_c E_s h}{E_s h + E_c t}\Delta\alpha(T_R - T_T) + \sigma_T \tag{3.13}$$

Here T_R and κ_R are the room temperature and the corresponding curvature.

3.3. Inverse Analysis to Estimate Unknown Parameters

The constitutive equation (3.1) has four parameters E_c, σ_N, n and σ_T to be defined. To estimate them, we use a multi-step procedure. First, the initial tangent modulus E_c

near the room temperature is determined. Here the slope of linear portion of curvature-temperature curve ($\Delta\kappa/\Delta T$), shown in Fig. 4, and the bimaterial formula for linear elastic materials (2.1) are used to determine E_c. Second the determination of the nonlinear parameters is carried out. Here the process can be simplified by shifting T and κ coordinates as $T^* = T - T_T$ and $\kappa^* = \kappa - \kappa_T$, respectively. The stress and strain are re-adjusted once the parameters are determined. Third, to obtain the best estimates of σ_N and n from the curvature-temperature ($T > T_T$), we utilize an inverse analysis as described next. Finally, the transitional stress σ_T and also the residual stress σ_{RT} at room temperature (20°C) can be obtained.

The present inverse analysis utilizes the Kalman filter technique (Kalman, 1960, Nakamura et. al., 2000, Gu et. al., 2003, Vaddadi et. al., 2003, Nakamura and Liu, 2007) to estimate the reference stress σ_N and the power-law exponent n. Essentially the algorithm updates the previous estimates based on indirect measurements of unknown state variables and covariance information and attempts to find the best estimate. In the formulation, two unknown parameters are expressed in a state vector form as $\boldsymbol{x}_t = [(\sigma_N)_t,\ n_t]^T$. Here t may represent the actual time as well as the temperature (e.g., from $T_{\min}$ to $T_{\max}$). The procedure is carried out with the following updating equation

$$\boldsymbol{x}_t = \boldsymbol{x}_{t-1} + \boldsymbol{K}_t [\kappa_t^{\text{meas}} - \kappa_t(\boldsymbol{x}_{t-1})] \ . \tag{3.14}$$

Here, $\boldsymbol{K}_t$ is the Kalman gain matrix and κ_t^{meas} is the measured curvature at t. Also $\kappa_t(\boldsymbol{x}_{t-1})$ is a curvature computed with estimated state parameters at the previous increment. In the above equation, the Kalman gain matrix multiplies the difference between the measured and computed curvature and it is given as,

$$\boldsymbol{K}_t = \boldsymbol{P}_t (\boldsymbol{\kappa}_t')^T \boldsymbol{R}_t^{-1} \text{ where } \boldsymbol{P}_t = \boldsymbol{P}_{t-1} - \boldsymbol{P}_{t-1} (\boldsymbol{\kappa}_t')^T (\boldsymbol{\kappa}_t' \boldsymbol{P}_{t-1} \boldsymbol{\kappa}_t'^T + \boldsymbol{R}_t)^{-1} \boldsymbol{\kappa}_t' \boldsymbol{P}_{t-1} \ . \tag{3.15}$$

With two state parameters and one measured parameter, the size of Kalman gain matrix is 2×1. Also $\boldsymbol{\kappa}_t'$ is a vector that contains the gradients of κ_t with respect to the each parameter. In addition, $\boldsymbol{P}_t$ is the measurement covariance matrix related to the range of unknown state parameters and $\boldsymbol{R}_t$ is the error covariance matrix related to the size of measurement error. Once the initial values are imposed, $\boldsymbol{P}_t$ is updated every step while $\boldsymbol{R}_t$ is prescribed at each step. In many cases, fixed values can be assigned to $\boldsymbol{R}_t$ as long as measurement error bounds do not vary substantially. Since the convergence rate is sensitive to the values of $\boldsymbol{P}_t$ and $\boldsymbol{R}_t$, proper assignments for these two matrices are essential. The initial measurement covariance matrix $\boldsymbol{P}_0$ is set according to the estimated ranges of state parameters (i.e., domain of unknowns) while the constant error covariance matrix $\boldsymbol{R}_t$ is chosen based on the estimated measurement error for the curvature measurements (~1% of total curvature change).The flowchart is shown in Figure 3.4. In many problems, forward solutions to relate state parameters to measurement parameters and their gradients require computations such as finite element analysis. However in this case, the established analytical curvature-temperature relation can be used to compute the required κ_t and $\boldsymbol{\kappa}_t'$. The accuracy of present procedure was tested with independent numerical simulations in (Nakamura and Liu, 2007).

Curvature κ changes as a function of σ_o and n for given T in κ^*- T^*, expressed as,

$$\kappa^* = \frac{6E_s E_{ave}^* ht(h+t)\Delta\alpha T^*}{E_s^2 h^4 + \left(E_{ave}^*\right)^2 t^4 + 2E_s E_{ave}^* ht(2h^2 + 3ht + 2t^2)} \tag{3.16}$$

Here, $T^* = T - T_T$ and $\kappa^* = \kappa - \kappa_T$. Then the derivatives of κ^* with respect to σ_o and n are

$$\frac{\partial \kappa^*}{\partial \sigma_0} = \frac{\partial \kappa^*}{\partial E^*_{ave}} \frac{\partial E^*_{ave}}{\partial \sigma_0} \quad \text{and} \quad \frac{\partial \kappa^*}{\partial n} = \frac{\partial \kappa^*}{\partial E^*_{ave}} \frac{\partial E^*_{ave}}{\partial n} \ . \tag{3.17}$$

From (3.8), each partial derivative is expressed as

$$\frac{\partial \kappa^*}{\partial E^*_{ave}} = \frac{6E_s ht(h+t)\left(E_s^2 h^4 - \left(E^*_{ave}\right)^2 t^4\right)\Delta\alpha T^*}{\left(E_s^2 h^4 + \left(E^*_{ave}\right)^2 t^4 + 2E_s\left(E^*_{ave}\right)ht\left(2h^2 + 3ht + 2t^2\right)\right)^2} \tag{3.18}$$

Also,

$$\begin{aligned} \frac{\partial E^*_{ave}}{\partial \sigma_o} &= \frac{E_c(n-1)\left(\sigma^*\right)^{n-1}\left(\sigma_0^{n-1} + \left(\sigma^*\right)^{n-1}\right)}{\left(\sigma_0^n + \sigma_0\left(\sigma^*\right)^{n-1}\right)\left(\sigma_0^{n-1} + n\left(\sigma^*\right)^{n-1}\right)} \\ \frac{\partial E^*_{ave}}{\partial n} &= \frac{-E_c \ln\left(\sigma^*/\sigma_0\right)\left(\sigma^*\right)^{n-2}\left(\sigma_0^n \sigma^* + \sigma_0\left(\sigma^*\right)^n\right)}{\left(\sigma_0^n + \sigma_0\left(\sigma^*\right)^{n-1}\right)\left(\sigma_0^{n-1} + n\left(\sigma^*\right)^{n-1}\right)} \end{aligned} \tag{3.19}$$

The above expressions are used in the Kalman filter algorithm.

3.4. Verification Study

Prior to implementing the proposed procedure to estimate unknown properties of TS ceramic coatings, the inverse analysis was carried out with simulated measurements generated from a finite element analysis. Since correct solutions are known in such a study, it can be used to evaluate the accuracy and robustness of the present procedure.

3.4.1. Geometrical Model

Several different types of models were constructed to evaluate the suitability and accuracy of the proposed procedure to extract the unknown material parameters. They are:

1. Nonlinear bimaterial model based on the beam theory [from (2.1)].
2. Finite element model with complete substrate and coating from beginning (no re-meshing).

3. Finite element model with element layer by layer build-up of coating (only vertically).
4. Finite element model with elements build-up along both horizontal and vertical directions.

In all models, curvature-temperature relations were generated with inputs of fictitious material parameter values. These relations were then used to estimate or back-track the material parameters. In Model 1, since the same equations are used to generate and extract the parameters, the inverse analysis was able to estimate essentially the same values as the input material parameters. In Model 2, a finite element model of Al substrate and YSZ coating was constructed and the temperature was raised to generate the curvature due to the CTE mismatch. As in Model 1 case, there was no residual stress at the room temperature which coincided with the zero-curvature temperature. For defining the stress-strain of coating, the constitutive relation (2) with arbitrary values was assigned for E_c, σ_0 and n. Again the proposed procedure was able to estimate the parameters accurately.

Unlike the first two models, more complex approaches were taken in Models 3 and 4. Here actual deposition processes of YSZ coating were closely replicated in the finite element models. Essentially the spraying process was simulated by adding new stress-free elements on previously added elements to characterize continuous depositions of YSZ layers. Similar works have been carried out by Bengtsson (1997) and Lugscheider (2003). The key difference in the two models is that a layer of elements which covers the entire specimen length is added each time in Model 3 while the process was much more refined in Model 4. The detail of Model 3 is not given here due to space limitation. The more refined procedure of Model 4 is described next.

In the actual TS process, a plasma gun is moved transversely to deposit molten particles. The number of spray passage depends on required thickness of coating. Based on a sample fabrication process, the passage is set as 15 with the final thickness of YSZ coating at t = 277μm. The substrate is assumed to be aluminum with thickness of h = 3.2mm. The re-meshing process during the element build-up is illustrated in Figure 3.5. At each pass, the coating deposition (18.5μm build-up) is simulated by adding five layers of elements. Note a special care was also taken to reproduce the actual deposition. Since the spray gun deposition rate varies with radial distance (more near the center), the element addition was carried out as a moving inclined slope. The sizes of elements were chosen carefully to optimize the accuracy and computation time. In total 4,500 elements were used for coating and 2,400 elements for the substrate. A significant amount of computational time was required to carry this simulation since the total number of re-meshing was 960. The total length is chosen to be 40mm, which is shorter than actual specimens but large enough compared to the thicknesses.

3.4.2. Thermal and Heat Flow Conditions

A special care was also taken for the thermal and heat flow conditions to replicate the actual process as close as possible. During the deposition and cooling down periods, the heat is continuously taken away by forced air convection while deposited molten particles add heat to the specimen. The heat flux out of surfaces was modeled with the following equation.

$$q_{out} = \tilde{h}(T - T_{\infty}) \tag{3.20}$$

Here $\tilde{h}$ is heat transfer coefficient, T_{∞} is ambient temperature and T is the surface temperature. After separate detailed simulations of heat transfer conditions with an inverse

analysis, the coefficient was chosen as $\tilde{h} = 45\text{W/m}^2\cdot\text{K}$. Since all tests are conducted at the same locations under similar conditions, this parameter was fixed for all deposition and cool down simulations. The heat input through the molten particles was chosen by comparing the simulated and measured temperature records. Unlike $\tilde{h}$ in (3.20), this parameter changes with the process parameters of TS. For the simulation results shown here (although not shown, several others were carried out), the heat flux was chosen to be $q_{in} = 210\text{W/m}^2$. In addition, the temperature of newly deposited particle is set as $T = 330^{\circ}\text{C}$ to match the measured curvatures. Although molten particles have much higher temperature, as soon as they strike the plate, the temperature drops immediately. After the deposition is completed, the specimen was cooled down through the top and bottom surfaces according to (3.20). The heat flow conditions are illustrated in Figure 3.5.

3.4.3. Materials

In the tests, Al6061 plates were used for the substrates. Since it is sensitive to temperature change, its properties were modeled as temperature dependent. The Young's modulus and the coefficient of thermal expansion follow (Material Properties Database, 1999),

$$\begin{aligned} E_s(T) &= -2.65\times10^{-7}T^3 + 2.4\times10^{-4}T^2 - 9.21\times10^{-2}T + 85.2 \text{ (GPa) for } 113\text{K} < T \le 573\text{K} \\ \alpha_s(T) &= -9.27\times10^{-12}T^2 + 2.59\times10^{-8}T + 1.54\times10^{-5} \quad \text{(1/K) for } 283\text{K} < T \le 575\text{K} \end{aligned} \tag{3.21}$$

Only the temperature ranges relevant to the present tests are noted above. Although in the experiments, the high temperature reaches only up to ~250°C (523K) during thermal cycles, the inclusion of temperature dependent properties for aluminum is very important in the estimations. In fact, without these considerations, the coating property would appear to be less nonlinear than actually is.

Since the stress in substrate does not reach very high level, plastic flow for the aluminum was not considered although limited yielding probably occurs when the substrate is struck with molten particles. The other parameters for the aluminum were chosen as $\nu = 0.33$, $\rho = 2{,}702\text{Kg/m}^3$, thermal conductivity $K_{\text{Al}} = 155\text{W/m·K}$ and specific heat capacity $c_{\text{Al}} = 963\text{J/kg·K}$. For the coating, the mechanical property was assumed to follow the nonlinear relation shown in (3). In the simulation shown here, they are chosen as $E_c = 22.8\text{GPa}$, $\nu = 0.32$, $\sigma_0 = 38\text{MPa}$, $n = 2.65$, $\sigma_T = -22.1\text{MPa}$ at $T_T = 30^{\text{o}}\text{C}$. Other parameters include the mass density $\rho = 5{,}436\ \text{Kg/m}^3$, the thermal conductivity $K_{\text{YSZ}} = 1.0$ W/m·K and the specific heat capacity $c_{\text{YSZ}} = 360\text{J/kg·K}$. These are representative values of YSZ coatings.

3.4.4. Simulated Curvature-Temperature Measurements

The finite element analysis was carried out under transient coupled heat-transfer and stress condition. The computed results for temperature and curvature are shown as function of time in Figure 3.6. Here the temperature is obtained at the mid-point on the bottom surface as in the actual tests where a thermo-couple attached to the substrate bottom is used. In both experiment and simulation, the substrate is pre-heated to 160^{o}C. For the curvature measurements, to be consistent with experimental procedure, it was computed from deflections at three points as shown in Figure 2.1.

In Figure 3.6, the oscillatory behavior during deposition in both temperature and curvature experimental measurements signifies the spray passages. This phenomenon was accurately captured in the computational simulations as shown. Although the amplitudes of noises are smaller than those from the experiment, the agreements are excellent. The higher frequency oscillations observed in the experiment are due to high velocity particles

striking onto to the substrate. Since such was not simulated, they were not observed in the finite element analysis. Note, although the temperature of deposited particles was adjusted to match the experiment, the temperature and curvature are the results of thermal-mechanical conditions described earlier and they were not directly imposed at the measured locations.

After 4~5 spray passes, the substrate temperature appears to reach the steady state. This suggests the heat input from particles and the heat removed from the specimen are approximately equilibrated. Since new elements added to the substrate have high temperature and they immediately cool down, the state of stress in the coating is tensile. These stresses cause the curvature to increase during the deposition as shown in Figure 3.6. After the deposition is completed at t = 190sec, both substrate and coating immediately cools down (from 246^{o}C to 20^{o}C). During the cool down phase, the same heat transfer coefficient $\tilde{h}$ = 45W/m^2·K in (3.20) was imposed across the substrate and coating surfaces. Since the CTE of substrate is higher than that of coating, the curvature reverses its sign and it eventually makes the overall stress in the coating to be compressive.

From the curvature and temperature results during the cool down period, the curvature temperature relation is obtained as shown in Figure 3.7. This relation is used to back-track the material parameters as described in the next section. In Figure 3.8, the through-thickness axial stresses are shown at four different temperatures. High stress gradients are observed in both Al substrate and YSZ coating in the boundary layer across the interface. These so-called quenching stresses were generated since the difference between particle and substrate temperatures during the first deposition pass is very high. Furthermore, unlike in the substrate, the stress does not change linearly outside this

boundary layer in the coating. It is nearly constant in the top half of the coating. The average stresses in the coating are 9.7MPa, −2.4MPa, −23.7MPa and −27.3MPa at the maximum, zero-curvature, transition and room temperatures, respectively. It is interesting to observe that at the zero curvature, the average stress is not zero due to the nonlinear through-thickness variation of stress. We also note that in real specimens, the stress states are more inhomogeneous due to locally high solidification stress in each particle. In fact, these high tensile stresses are the causes of many intra-splat cracks (Teixeira et al., 1999). The magnitude of residual stress at the room temperature is also relevant in terms of defining the stress-strain relation. It also keeps micro-cracks from extending. However, for thermal barrier coating applications, the overall coating stresses are likely to be tensile in the high temperature environments. It is emphasized that these stresses vary according to processing parameters, coating thickness, pre-heat temperature and other parameters. Alternatively, one may generate a desired stress state with suitable spray parameters.

3.4.5. Estimated Material Parameters

From the curvature-temperature relation shown in Figure 3.7, the proposed procedure was carried out to extract the unknown parameters. First, the transition curvature and temperature are identified as $\kappa_T = -5.2\times10^{-5}$/mm and $T_T = 30^{o}$C, respectively. Since the curvature change is gradual, precise determination of the transitional point is difficult. However, our analysis (to be shown later) demonstrates the precise determination of T_T is not critical to re-construct the stress-strain relation. Using the linear slope between T = 20^{o}C and 30^{o}C and the curvature formula (2.1), the Young's modulus of the coating is estimated as E_c = 23.2GPa, which is 1.8% off from the input modulus (22.8GPa).

Next, the two nonlinear parameters σ_0 and n are estimated with the Kalman filter procedure described above after adjusting the curvature-temperature relation to $T^*-\kappa^*$ coordinates as shown in Figure 3.7. Here we have selected 25 curvatures and temperatures at time increment of dt = 10sec for t > 200sec for the inputs in the Kalman filter. The initial estimates of σ_0 and n were chosen as follows. Within the ranges of 10MPa < σ_0 < 90MPa and 1 < n <4, σ_0 and n are incremented into forty separate values to generate 41×41 = 1,681 sets of initial estimates. Each set of initial estimates are processed through the Kalman filter and the final estimates are obtained after 25 steps. In general, different initial estimates do not merge at the same point but a robust inverse procedure should generate a small domain of convergence. The intensity of converge plot is created from the 1,681 sets of final estimates as shown in Figure 3.9. Here high intensity regions suggest greater convergence of initial estimates. The best estimates can then be made from either the location where the highest intensity occurs or the weighted average as marked in the figure. Our estimates are σ_0 = 35.6MPa and n = 2.53, respectively. They defer the exact or input values by 6.3% and 4.5%, respectively.

Finally the remaining material parameter, the transitional stress was computed as σ_T = −21.2MPa, which is about 4% lower than the input value. The residual stress at room temperature is also calculated as σ_R = −24.5MPa, which is ~10% different from the average residual stress through-thickness shown in Figure 3.8. Using these estimated parameters, the stress-strain relation is re-constructed according to (3.1) as shown in Figure 3.10. Here the prescribed or input/exact stress-strain relation is also shown with the circles. Although each estimated parameter is slightly off from the corresponding input value, the agreement

between two stress-strain curves is surprising. In fact, the two results essentially overlaps with each other.

As noted earlier, one possible difficulty in this procedure is identification of the transitional temperature. Suppose T_T = 50°C was chosen instead of T_T = 30°C as was chosen earlier. With this T_T, the inverse analysis was re-carried out and the unknown parameters were estimated according to the same inverse procedure. The resulting stress-strain curve is shown in Figure 3.10. There are clearly larger errors than that estimated with T_T = 30°C. However, the stress-strain curve of T_T = 50°C is still very close to the input/exact curve. These results of verification study support the effectiveness of present procedure.

3.5. Sample Implementation

As described earlier, the substrate curvature technique was utilized for the entire investigation and Al6061 substrate was chosen as the substrate material. There were several reasons for this. Primarily, aluminum provided significant deflection, due to relatively low stiffness, and high thermal mismatch with YSZ, for high fidelity curvature measurements which would allow careful extraction of nonlinear parameters in thick top coats. Also YSZ tended to bond well to the aluminum substrate and the high thermal conductivity of aluminum also reduced propensity for thermal gradients in the substrate. Similar studies were also conducted with steel based substrates, but the YSZ bonded poorly to the steel and resulted in delamination. Experiments with superalloy substrates and bond coats (e.g., NiCrAlY) are also under consideration for three layer model.

Here the above proposed procedure is applied to estimate unknown properties of an actual TS ceramic coating. The cooling phase of the curvature-temperature curve is

used to estimate E_c, σ_N, n and σ_T. For this and all other specimens, the properties of Al6061 substrate are assumed as temperature dependent as (3.21). Note that the inclusion of above temperature dependent properties for aluminum is critical in terms of estimating accurate properties for TS coatings.

From the results shown in Figure 3.11, the transitional temperature is identified as $T_T = 50^oC$. The corresponding transitional curvature is $\kappa_T = -0.22$/m. Since the curvature change is gradual, precise determination of the transitional point is often difficult. In order to quantify the effects of variation of T_T, we also estimated the properties for $T_T = 30^oC$ and 60^oC. The differences in the modulus were within ±1.7% and the variations of stress-strain relations were well within the error bounds. Thus a slight variation in T_T appears to have limited influences on the resulting estimated stress-strain curves.

Next, two nonlinear parameters σ_N and n are estimated with the Kalman filter procedure. Here in order to facilitate the interpretation, initially a simpler form of constitutive equation, with $\sigma_T = 0$ in (3.1). Once the nonlinear parameters were estimated then σ_T is computed from the difference between zero and transitional curvature values. As described earlier, due to the non-equilibrium thermal state, the data from initial cool down phase was not used during the estimation of the properties. Here 30 data points within $50^oC < T < 274^oC$ are selected for the inputs in the Kalman filter. The initial estimates of σ_N and n are chosen as follows: Within the domain of 10MPa $< \sigma_N <$ 90MPa and $1 < n < 4$, σ_N and n are incremented into 40 intervals to generate 41×41 = 1,681 sets of initial estimates. Each set of initial estimates is processed through the Kalman filter and the final estimates are obtained after 30 steps. In general, different initial estimates do not merge at the same point but a robust procedure should generate a small domain of

convergence. The intensity of converge plot is created from the 1,681 sets of final estimates as shown in Figure 3.12. Here high intensity regions imply greater convergence of initial estimates. The best estimates can then be made from the weighted average of converged values. Our estimates are σ_N = 37MPa and n = 3.2, respectively. Afterward the transitional stress and the residual stress are computed as σ_T = −32MPa and σ_{RT} = −38MPa, respectively. The error bounds are estimated as ΔE_C = ±2GPa, $\Delta\sigma_N$ = ±3MPa and Δn = ±0.2 based on the repeatability of measurements and the sensitivity of solutions. It is also noted that since different combinations of σ_N and n yield the same strain according to the uniaxial model (3.1), very precise determinations of σ_N and n are difficult, especially from the single measurement of curvature. However, the estimated stress-strain curves from different combinations of σ_N and n would still look very similar, as well as results of any post analyses using such curves.

Using these parameters, the stress-strain relation is reconstructed as shown in Figure 3.13. The two circles represent the bounds at the room temperature (20^{o}C) and the maximum temperature (274^{o}C). Essentially, the slopes outside these bounds are extrapolated results since only the records between these temperatures are actually used to estimate the property. Note the coating may behave in a different way outside the range, especially under large tensile load (e.g., further cracking).

In most inverse analyses, there is no independent way to prove that best estimates are indeed correct or near-correct solutions. However, there are two ways to judge the accuracy. One is based on the convergence behavior of various initial estimates. A small domain of convergence implies the robustness of inverse method as many initial estimates converged near the same location (i.e., similar estimates). The present analysis

generated small domains of convergence, and thus supports the accuracy of the estimates. An additional confirmation can be made from re-creation of the curvature-temperature plot. Using the best estimates as inputs, the curvature-temperature relation was re-computed using the nonlinear bimaterial formula as shown in Figure 3.14. Its agreement with the measured curvature is excellent as the measured data (shown with circles) essentially lies on top of the reconstructed curve with the estimated parameters. Thus for the present material model, the estimated parameters represent accurate measures of the coating properties.

3.6 References

Bengtsson, P., Persson, C., (1997), "Modelled and measured residual stresses in plasma sprayed thermal barrier coatings". *Surface and Coatings Technology* 92, 78-86.

Finot, M. and Suresh, S., (1996), "Small and large deformation of thick and thin film multi-layers: effects of layer geometry, plasticity and compositional gradients", *Journal of Mechanics and Physics of Solids* 44, 683-721.

Gu, Y., Nakamura, T., Prchlik, L., Sampath, S., Wallace, J., 2003. Micro-indentation and inverse analysis to characterize elastic-plastic graded materials. *Materials Science and Engineering* A345, 223-233.

Kalman, R.E., (1960), "A new approach to linear filtering and prediction problems", *ASME Journal of Basic Engineering*, 82D, 35-45.

Lugscheider, E. and Nickel, R., (2003), **"**Finite element simulation of a coating formation on a turbine blade during plasma spraying", *Surface and Coatings Technology* 174-175, 475-481.

Material Properties Database, (1999), *JAHM Software, Inc.*

Nakamura, T., Wang, T. and Sampath, S., (2000), Determination of properties of graded materials by inverse analysis and instrumented indentation, *Acta Materialia* 48(17), 4293-4306.

Nakamura, T. and Liu, Y., (2007), "Determination of nonlinear properties of thermal sprayed ceramic coatings via inverse analysis", *International Journal of Solids and Structures,* 44, (6), 1990-2009.

Vaddadi, P., Nakamura, T., Singh, R., (2003), "Inverse analysis for transient moisture diffusion through fiber-reinforced composites". *Acta materialia* 51, 177-193.

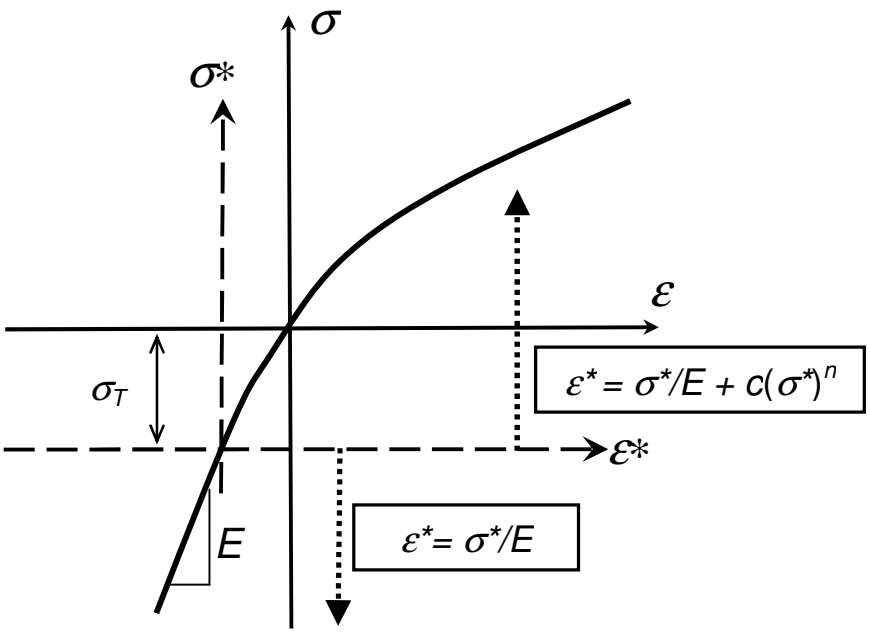

Figure 3.1 Nonlinear stress-strain relation model for thermal spray ceramic coatings. Change in linear and nonlinear stress-strain relation occurs at transitional stress σ_T. Corresponding equations are noted below and above the ε^* axis, respectively.

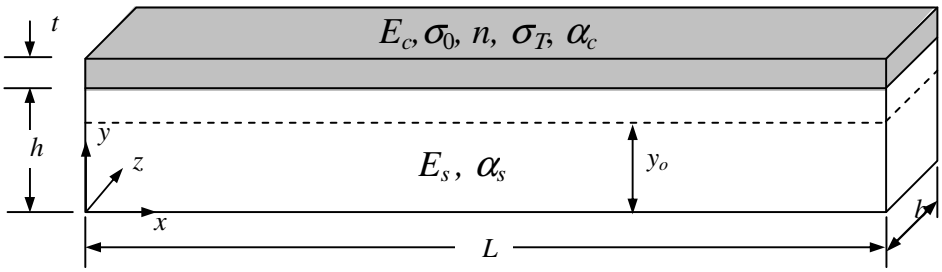

Figure 3.2 Schematic of thermal spray coating on substrate with relevant dimensions. Corresponding material parameters are noted and the location of neutral axis y_o is shown.

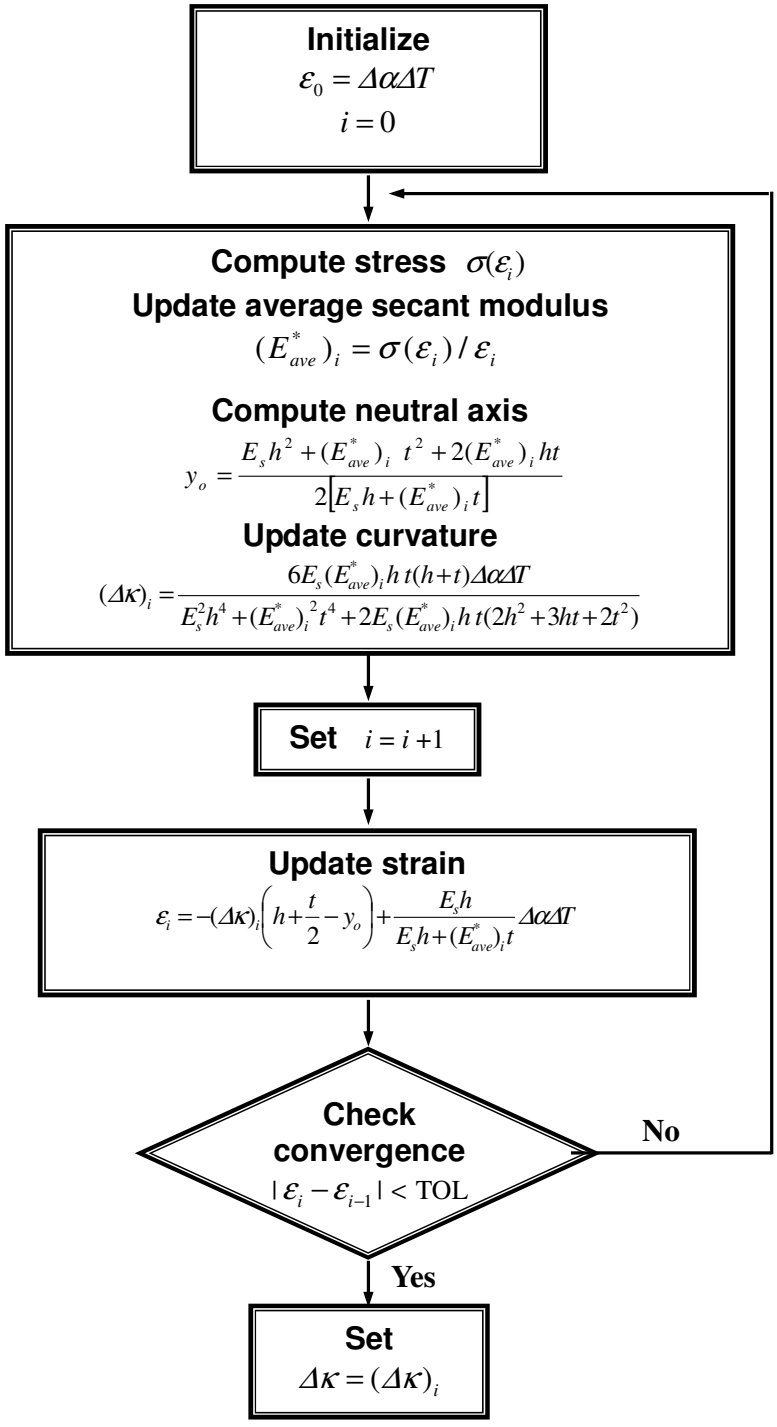

Figure 3.3. Flowchart of curvature calculation for a given temperature change ΔT.

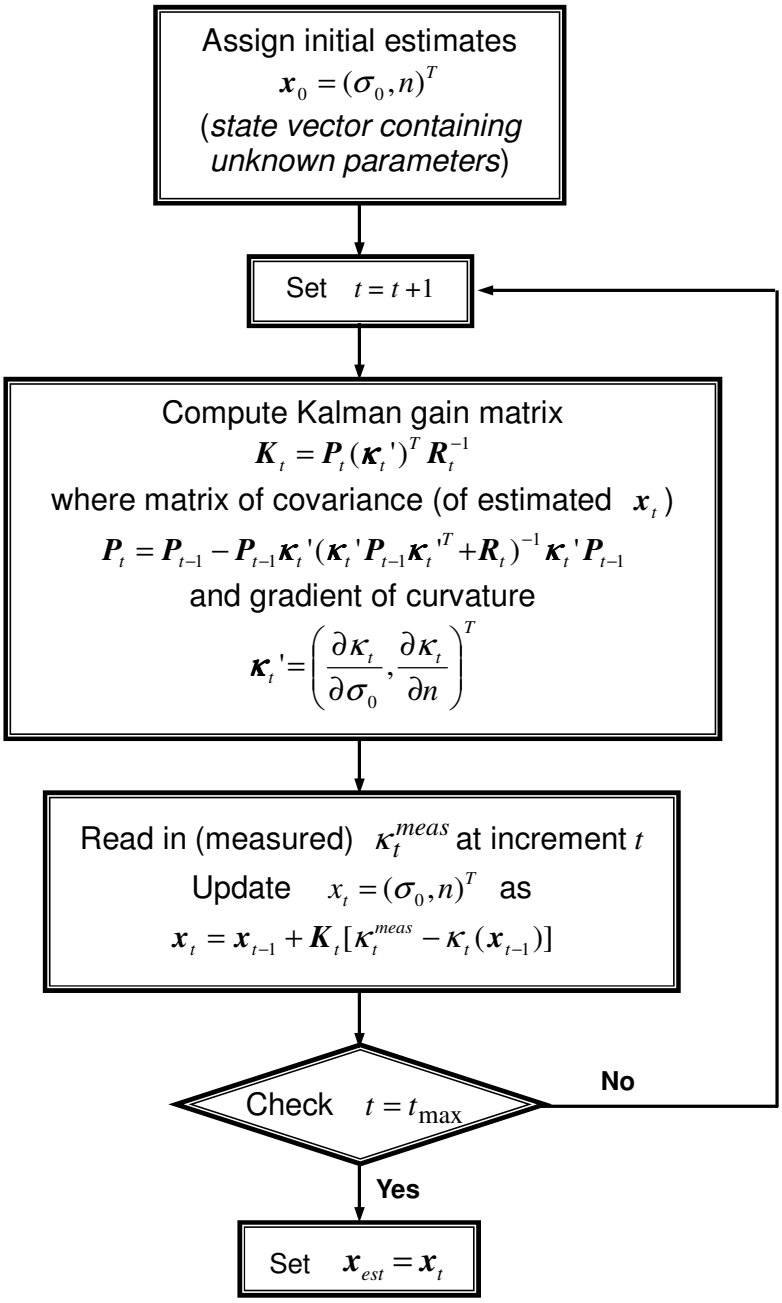

Figure 3.4. Flowchart of Kalman filter procedure to estimate the unknown parameters.

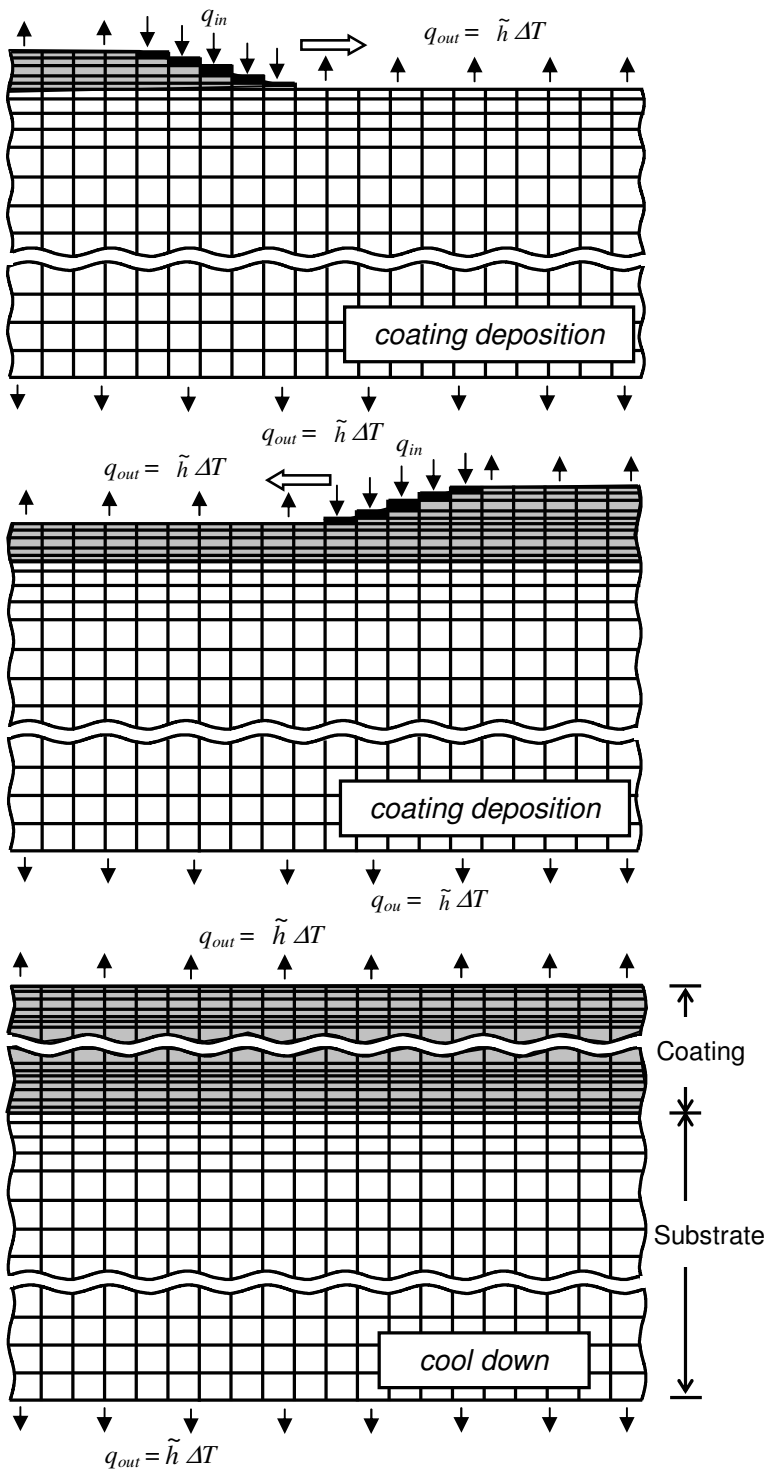

Figure 3.5. Accurate simulation of thermal spray deposition process through adding elements along transverse direction under proper heat transfer. The bottom figure shows cool down of completed deposition.

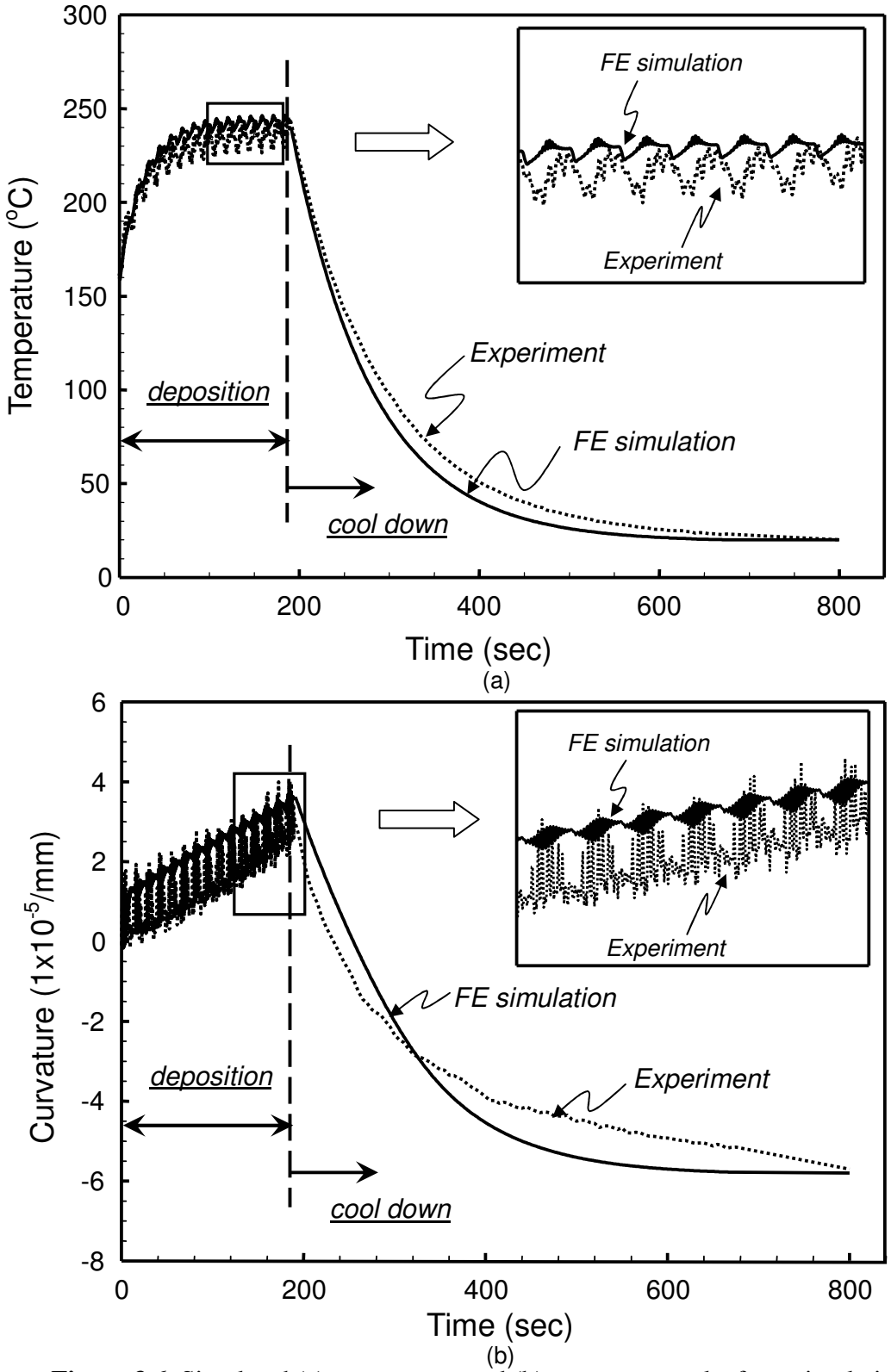

Figure 3.6. Simulated (a) temperature and (b) curvature results from simulation. For comparison experimental results are also shown.
Magnified curves in insets have different coordinate scales.

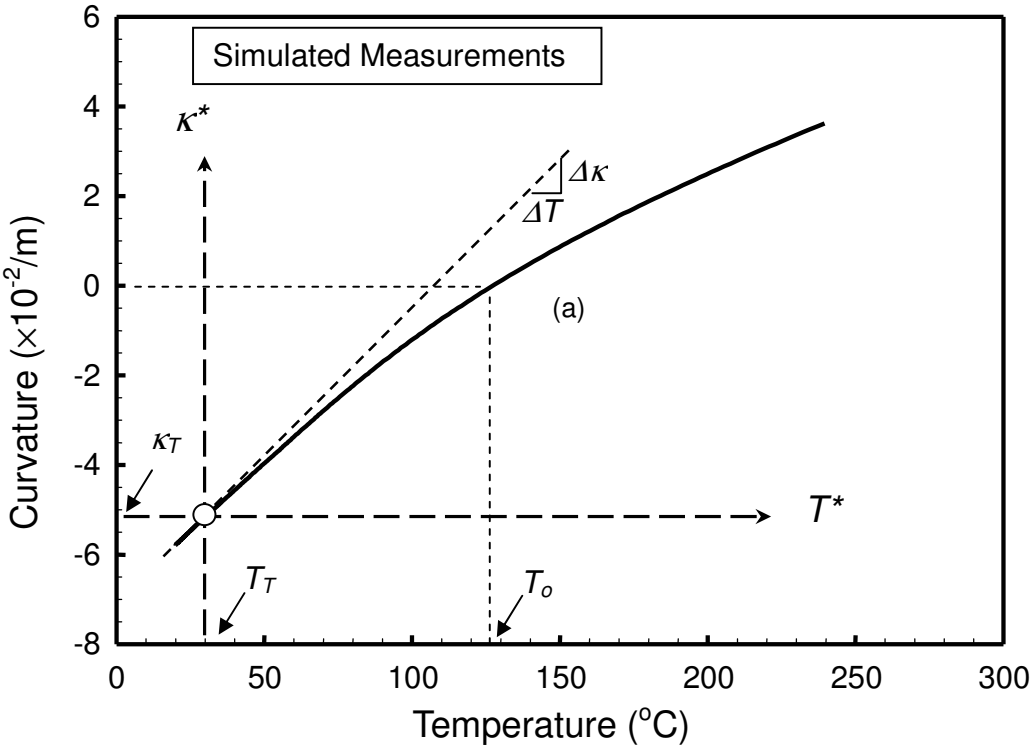

Figure 3.7. Simulated curvature-temperature record during cool-down. Key curvature and temperatures are noted.

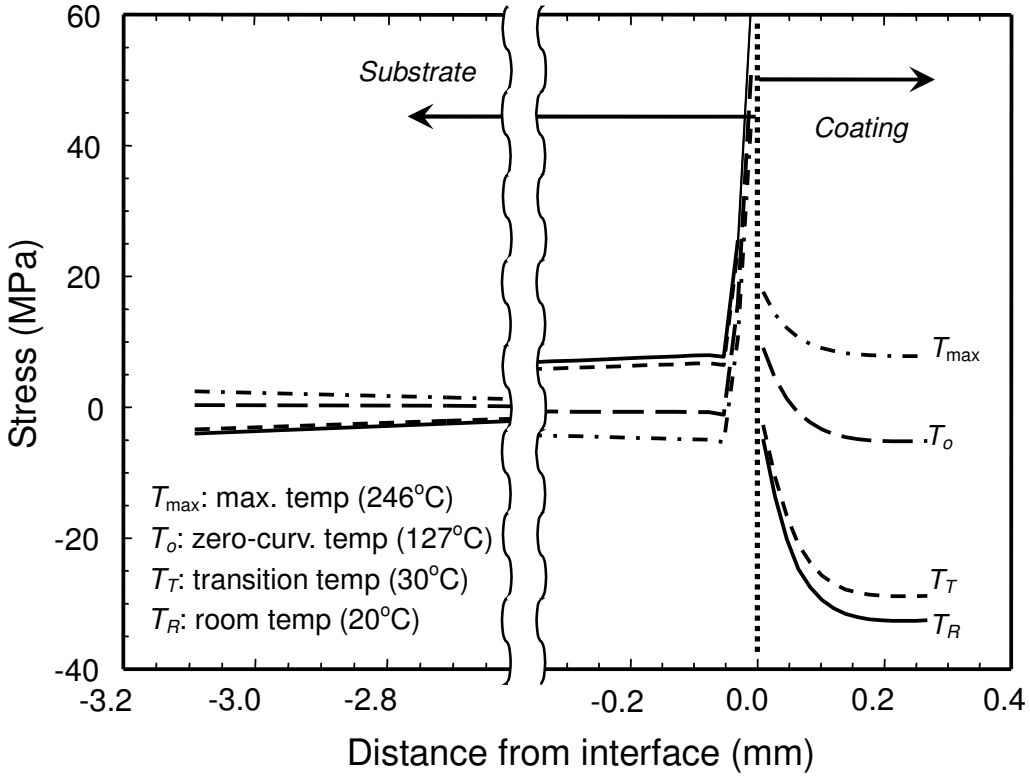

Figure 3.8. Axial stress through thickness at different temperatures.

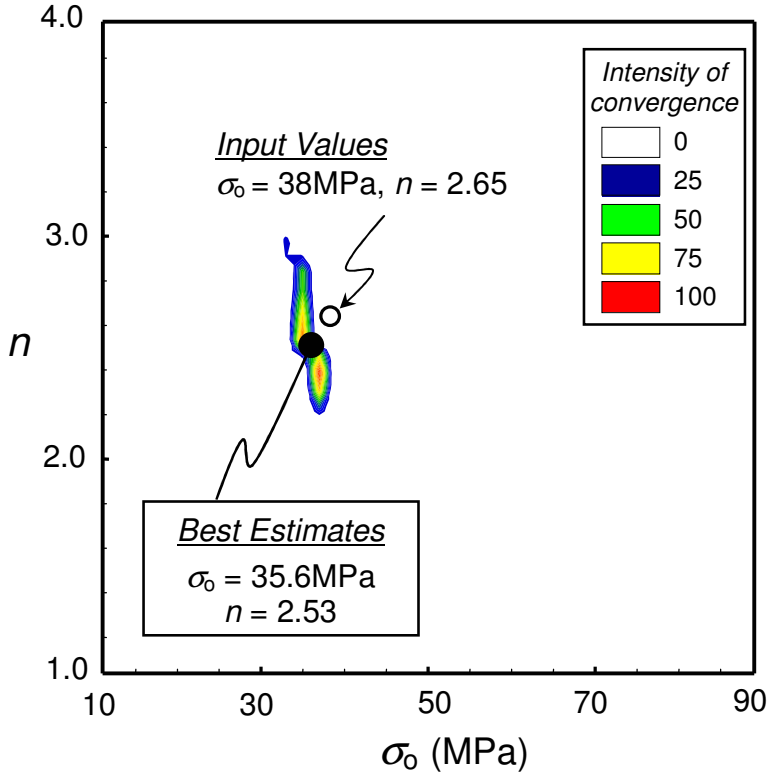

Figure 3.9. Intensity of convergence plot generated from the inverse analysis from simulated TS deposition and cool down. A high intensity represents convergence of many initial estimates and likely location of best estimates. The scale of intensity (i.e., 0 to 100) is relative. The location of input values is also noted.

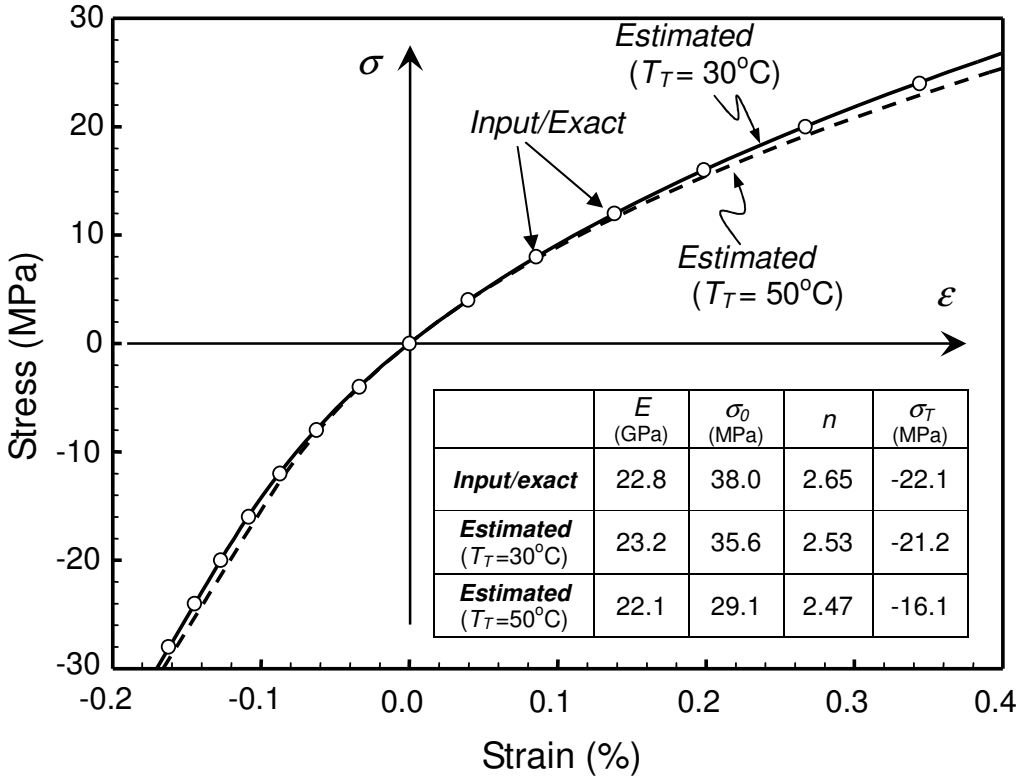

	E (GPa)	σ_0 (MPa)	n	σ_T (MPa)
Input/exact	22.8	38.0	2.65	-22.1
Estimated (T_T=30°C)	23.2	35.6	2.53	-21.2
Estimated (T_T=50°C)	22.1	29.1	2.47	-16.1

Figure 3.10. Reconstructed stress-strain relations based on estimated (solid line) and input/exact (circles) parameters. Note estimated result (T_T = 30°C) nearly overlaps with the input/exact relation. Estimated result with a different transitional temperature (T_T = 50°C) is also shown for comparison.

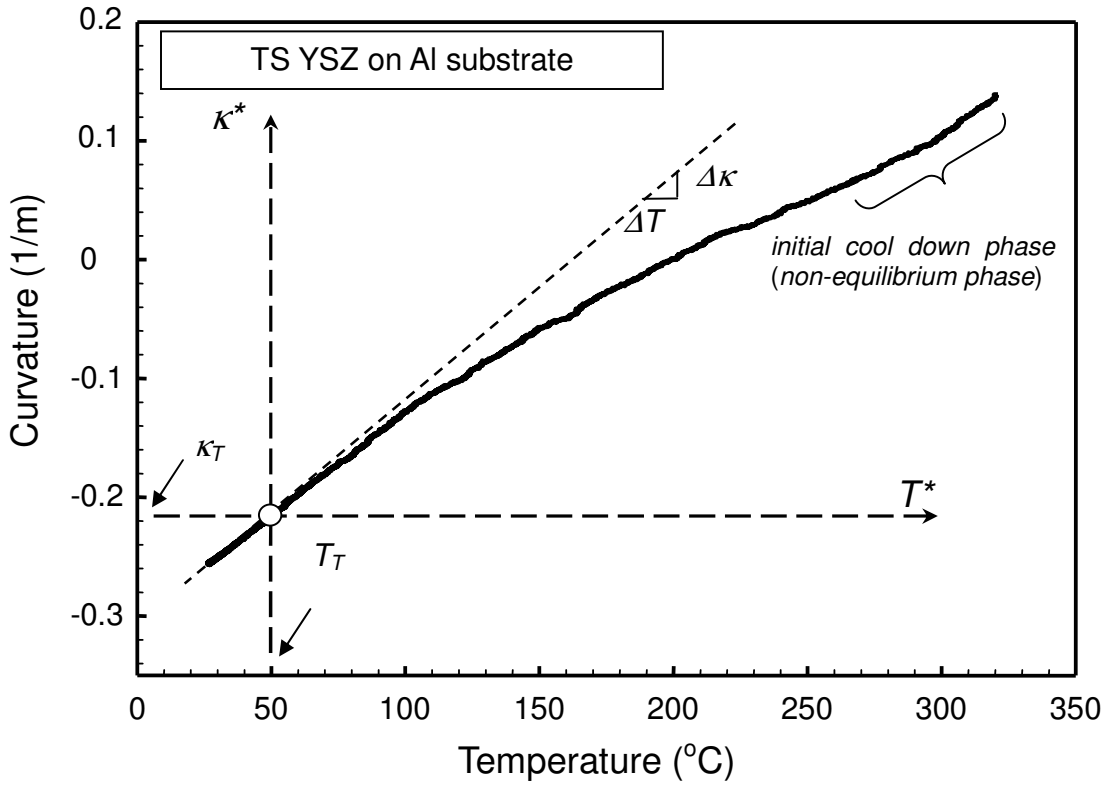

Figure 3.11. Identification of transitional point (linear to nonlinear) to extract initial tangent modulus E_c from ΔT and $\Delta\kappa$. Shifted coordinates centered at T_T and κ_T are also shown.

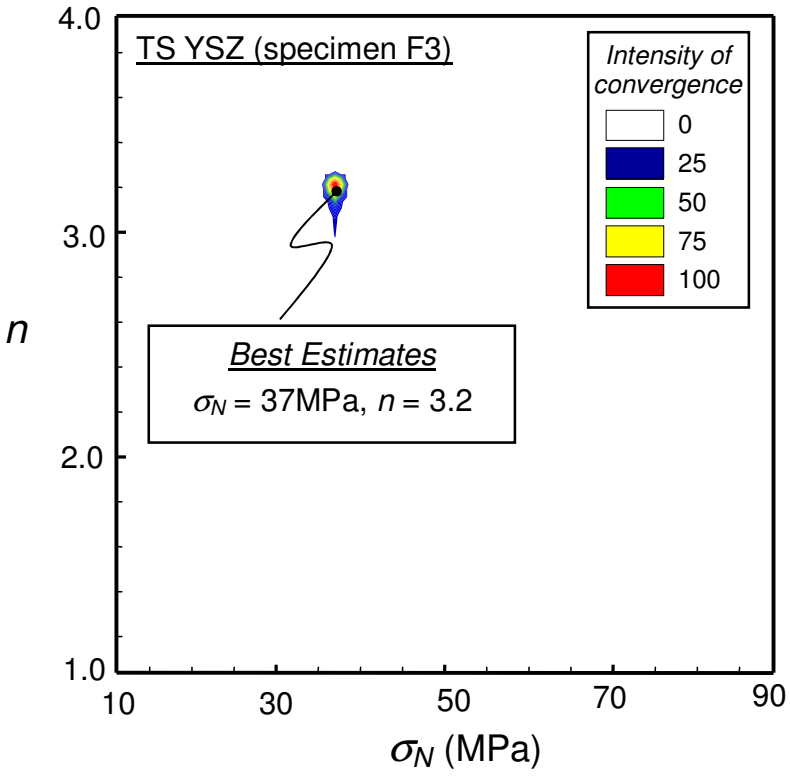

Figure 3.12. Intensity of convergence plot generated from the inverse analysis with measured curvature change with temperature during thermal cycle.

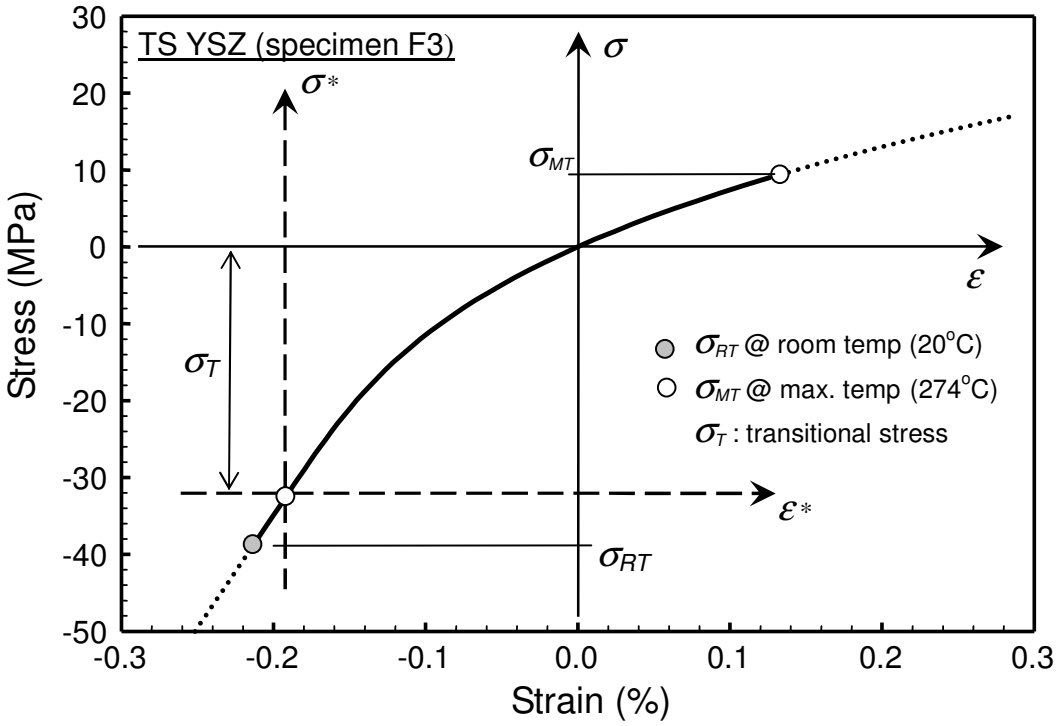

Figure 3.13. Corresponding nonlinear stress strain relation with the best estimates. The coordinates centered at the transition point are also shown.

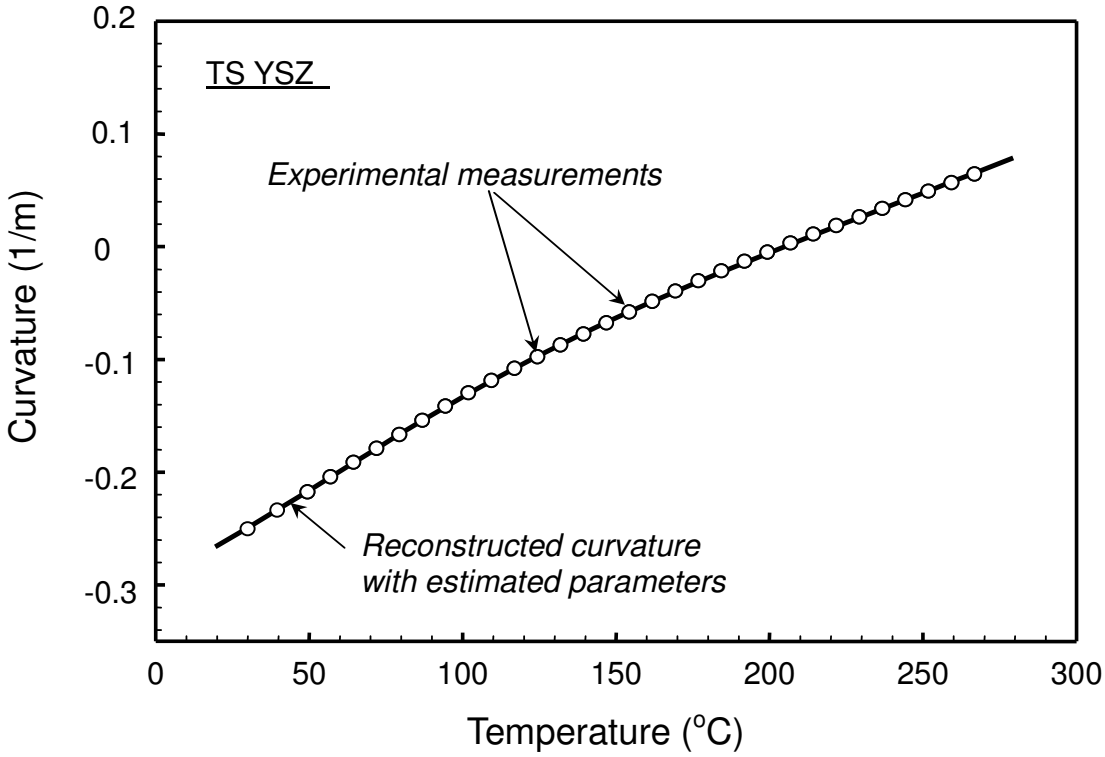

Figure 3.14. Comparison between measured (circles) and simulated (solid line) curvatures. The latter is calculated by assigning the best estimates as properties in the nonlinear bimaterial formula.

Chapter 4

Effects of processing parameters on coating properties

The above non-linear analysis method was used to investigate effects of various process conditions on the nonlinear mechanical properties of TS YSZ coatings. Here, effects of the following processing conditions are discussed.

- Variations in feedstock size distributions, which affect not only the particle state but the splat morphology and deposit characteristics as well.
- Different feedstock morphologies with known implications in thermo-mechanical performance of TBCs (Kulkarni et al., 2003).
- Variations in in-flight particle temperature and velocity as affected by torch conditions.
- Other deposition conditions of critical importance for actual components including spray distance and angle.

Over 50 experiments were conducted through the course of this investigation, but for the sake of brevity only selected results from the above are presented here. The tabulated processing conditions for different specimens are listed in Table 4.1.

4.1. Effect of Feedstock Particle Size Distribution

Feedstock particle size is one of the key parameters that affect the deposit microstructure. Particle size affects the molten fraction of particles during plasma spraying. In particular for YSZ, smaller particles are desired given the high melting temperature and low thermal conductivity of the particles. However, other important attributes influence the deposit formation. For instance, smaller particle size yields

thinner splats (due to better melting) and more compaction (due to higher velocities) resulting in greater deposit density and a smoother surface. However, smaller particle size will also result in a larger fraction of splat interfaces per unit thickness of the coating. Several previous studies have investigated the effects of starting particle size on the melting, deposit formation dynamics, microstructure and properties of the coatings (Kulkarni et. al., 2003, Kweh et. al., 2000, Despande et. al., 2004). Significantly higher modulus (obtained via indentation) and hardness have been observed for the coating produced using fine powder with smoother surface and less unmelted particles.

For this investigation a single powder morphology, Fused and Crushed (FC), was chosen with three different size distribution referred to as fine, coarse and ensemble with 10-45μm, 45-75μm and 10-75μm powder sizes. They were sprayed by air plasma on an aluminum (Al6061) substrate under the similar controlled processing parameters including spray distance, final coating thickness, and spray angle as listed in Table 1.

Curvature-temperature records Figure 4.1 were used to characterize coating properties through the procedure described in Section 3. Continuous stress-strain relations of coating in the experimental temperature range from the room to the maximum temperatures were identified as shown in Figure 4.2. The estimated parameters are listed in Table 4.2. The results confirm that the in-plane modulus at room temperature increases as powder size decreases resulting from improved coating density (this was confirmed from other density and porosity measurements as well). All three coatings show nonlinear stress strain behavior, while not surprisingly a stiffer mechanical response is observed for coating produced by fine powder. Since the coatings have many microcracks and pores, the opening cracks give rise to the more compliant response of coating with increasing tension.

Once the cracks close or partly close, coatings show stiffer response. It is interesting to observe that the ensemble curve, powder with large variation of particle sizes (i.e., equal mixture of fine and coarse grains) falls between the other two.

Bounds of stress change during thermal cycle are indicated in as circles in Figure 4.2. Although it is likely that stress-strain relation would follow the extrapolated paths at least for some extent, specimens were not subjected outside these bounds. Note for these specimen, the stresses at corresponding maximum temperatures (T_{max} = 200-230^{o}C) reach very low tensile state. On the other hand, the amplitudes of residual stresses at the room temperature are significant, reaching −37MPa for fine powder, and −33MPa for both coarse and ensemble powder.

4.2. Effect of Powder Morphology of Feedstock

In the case of YSZ, starting feedstock morphology can strongly affect the microstructure of the coating (Kulkarni et. al., 2003). This is due to the nature of flame-particle interactions with respect to behavior of the particles in-flight has significant contribution to microstructural variations. Here we briefly describe three morphologies commonly used for YSZ coatings: fused and crushed (FC), agglomerated and sintered (AS), and plasma densified hollow sphere (HOSP). FC powders are very dense with the angular/polyhedral morphology, AS powders are globular, and HOSP powders are hollow spheroids (Kulkarni et al., 2003, Kulkarni et al., 2003, Wang et al., 2003). In this study, Comparable size distributions of all three morphologies of feedstock mentioned above were used.

In an effort to normalize potential variance in particle state, the process parameters were optimized such that the averages and distributions in particle temperatures and

velocities (averaged over 10,000 particles) for each of the morphologies were kept nominally constant. In fact even the distributions of temperature and velocity were kept relatively similar by relatively close choice of process parameters. The procedure used to accomplish such optimization through process control is a significant study in itself and is partially described in Streibl et al. (2006).

From the curvature measurements shown in Figure 4.3 and the present identification procedure, mechanical properties were determined as listed in Table 1. Coating sprayed by FC powders shows higher modulus compared with the HOSP and AS powders. The stress-strain relations in Figure 4.4 show their nonlinear behavior. The HOSP material displays a larger compliance in tension and higher degree of nonlinearity compared to the other morphologies. In fact it has been anecdotally reported in industrial work that the HOSP material has had beneficial thermo-mechanical response in service. The origin of such a response is related to larger fraction of interfaces created during consolidation of the hollow powder (lower density). Although establishment of detailed microstructure-nonlinearity relation requires further investigations, some connections are described in Discussions.

4.3. Effect of Particle Temperature and Velocity

Particle temperature and velocity are known to have a strong influence on the melting and flattening of particles, affecting the droplet solidification and adhesion among the splats. Temperature and velocity are two of the most important parameters influencing the coating microstructure. Friis et al. (2001) showed that an increase in temperature and velocity of particles results in a decrease in total porosity and denser coatings. Particles of

high temperature and velocity possess high kinetic energy and low viscosity, which lead to the particles better filling the irregularities in the deposited splats.

To investigate the dependence of the nonlinear response of the YSZ coating with the particle state, an operational parameters space was explored. First a design of experiments approach was used to investigate the particle temperature velocity space for the particular powder and spray condition. Subsequently three conditions with differences in particle temperatures and velocities were identified and coatings were fabricated. The three resultant coatings were made from particle streams with average temperatures and velocities (in increasing order) of 2504^{o}C, 80m/s, 2631^{o}C, 103m/s and 2677^{o}C, 150m/s respectively. Figure 4.5 presents the curvature temperature relationships for the three above coatings and the corresponding nonlinear stress strain relations are shown in Figure 4.6. One can clearly see that the coatings produced at low particle temperature and velocities have a greater compliance compared to the higher temperature, velocity sample. These results quantitatively and robustly confirm conventional 'rule of thumb' from point of view of process-microstructure correlation. Note although the thicknesses of three specimens are not similar here, the effects of particle temperature and velocity appears much greater than the thickness effect described below.

4.4. Effects of Other Parameters

Figures 4.7-4.10 show additional examples of parametric effects including spray distance, angle, speed and coating thickness. All these other parameters are important to industry since the turbine is a complex 3D object and there are spatial microstructural distinctions within the coating depending on geometry and associated changes in spray distance, torch speed and deposition angle.

The results indicate that the coating was somewhat more nonlinear when it was sprayed from greater distance (from 130mm). The spraying at an angle (at 60^o) produces much more nonlinear specimen. Although it is not apparent from Fig. 10(b), while σ_N values are similar for both cases, n values are 1.9 for 90^o specimen and 3.9 for 60^o specimen. The spray speed affects the number of particles per unit area per unit time and can modify the evolution of the microstructure. Our results indicate that the compliance is affected by this parameter. Coating fabricated with spray speed of 150 mm/s is more densified and stiffer than that with 450 mm/s.

The influencing parameters are not limited to powder and spray conditions. The deposited coatings posses different mechanical characteristics if they have different final thickness. Two specimens with different thicknesses, shown in Figure 4.10, exhibit very different stress-strain relations. In fact, the thinner coating (t = 424μm) is more compliant and nonlinear than the thicker one (t = 960μm). (In exploring the various process variations, the thicknesses of the various coatings were kept relatively similar to avoid this effect). It is possible that different heat transfer conditions after deposition produce dissimilar microstructures during cool down period. These examples further demonstrate the utility of the proposed approach in quantifying the mechanical attributes of these nonlinear ceramic coatings.

It can be argued that a coating is likely to exhibit higher nonlinearity when it possesses a high density of embedded micro-cracks since opening and closure of these cracks cause such a behavior. Our initial results suggest that the nonlinearity increases in thinner coatings, coatings sprayed at a tilted angle and those obtained conditions such as high particle temperature. Rigorous confirmations of these predicted relations between

the process conditions and microstructures require further studies.

Characteristics of each coating's mechanical behavior can be summarized graphically, as shown in Figure 4.11. Here 'nonlinear degree' (*ND*) is introduced to denote the extent of nonlinearity as,

$$ND = E / E^*_{0.001} \quad . \tag{4.1}$$

Here E is the room temperature elastic modulus defined in (3.1) and $E^*_{0.001}$ is the *secant* modulus between the transitional point (σ_T, ε_T) and the stress and strain at $\varepsilon = 0.001$. Note that this form has no physical significance (i.e., operationally defined), and other formulations are also possible to quantify the nonlinearity. However this form has shown to be least sensitive to measurement and interpretation errors. If a coating is linear, *ND* = 1 while a large *ND* value denote greater nonlinearity. In Figure 4.11, this parameter is plotted as a function of the room temperature modulus *E* for each specimen. In the figure, approximated quadrangles are drawn to classify stress-strain relations of various coatings. Essentially, if a coating falls within the quadrangle *I*, it is expected to remain stiff throughout the loading. On the other hand, if a coating falls in the quadrangle *II*, then it tends to more compliant under large tension. Similarly, if a coating stays in the quadrangle *III*, it is compliant and also expected to be more so under larger tensile load. Lastly if a coating in the quadrangle *IV*, then its stiffness remains at similar low level regardless of the loading magnitude.

Some observations can be made from this figure. It suggests the coating sprayed under high temperature at mid-velocity (V2) to be initially stiff but becomes more compliant at higher stress. For HOSP powder coating (F3), it is initially compliant and more so under large stresses. Such a phenomenon is consistent with the high density of

interfacial cracks observed in HOSP coating. On the other extreme, a coating fabricated with high temperature and high velocity particles (V3) remains stiff regardless of the level of loading (or thermal strain) considered in this study. The figure also suggests the angle sprayed coatings (A2) to be very compliant and stays linear even at higher stresses. These integrated connections between process science and mechanics will enable opportunities for microstructural control for optimal design and performance of thermo-mechanical coatings. Estimated stress-strain relations presented here are qualitatively consistent with those measured under mechanical load (Harok and Neufuss, 2001, Eldridge et al., 2002, Wakui et al., 2004). Coatings exhibit stiffness response under compression and more compliant response under tension. Although it requires knowledge of CTE, an advantage of curvature measurement under temperature change is that it produces more uniform stress state within a coating than that under mechanical load since it does not generate stress concentration near load-points.

In this study, the procedure was used to quantity the effects of both starting YSZ powder particle characteristics and processing parameters on the effective properties. Compared to linear elastic properties assumed in traditional models, the nonlinear stress-strain relations offer a more accurate description of coating behavior. In earlier studies, relationships between the microstructural changes with different spray conditions to curvature/stress-stain were investigated for linear properties (Deshpande et al., 2004, Friis et al., 2001, Kulkarni et al., 2003, Kulkarni et al., 2003, Wang et al., 2003). These studies were expansive and comprehensive and examined the microstructure-thermal conductivity and elastic properties for various feedstock and process conditions. The nonlinear response closely follows the links between microstructure and properties as

described in the earlier papers. For instance, SEM images in Figure 4.12 show distinctly different morphology of TS coatings with two types of feedstock. The FC coating contains shorter embedded cracks and smaller density of cracks (i.e., total crack lengths per area). On the other hand, the HOSP coating contains many long interlamellar cracks and higher crack density. The larger nonlinearity observed for HOSP coating is likely to be the result of these cracks as more of them open and close under tension and compression. Though not obvious here, a higher magnification images reveal HOSP to also possess many (partially) closed intra-splat cracks. These observations are consistent with measurements by small-angle neutron scattering (SANS) technique (Kulkarni et. al., 2003). They revealed the crack density of HOSP to be about 50% higher than that of FC and a higher interlamellar porosity with HOSP as well.

4.7 Repeatability and Process Reliability Study

The present tool is particularly interesting in that not only does it quantitatively confirm arguments about coating behavior based on microstructural observations, but it also provides a robust 'check' for new process and/or material feedstock strategies. The relative simplicity of the technique allows its ready use in many spray facilities, elevating the precision with which coating manufacturers may describe and compare their products.

Three sets of samples are tested for evaluating the repeatability and process reliability. One is from Stony Brook Thermal Spray Center and the other two are from industry. The processing parameters remain almost the same, including particle temperature and velocity, spray distance, angle and speed and others. Three samples are fabricated in Stony Brook with the same coating thickness. The corresponding moduli at

room temperature and the degrees of nonlinearity are shown in Table 4.3. Their stress strain relations are shown in Figure 4.15 and very close stress strain behaviors are achieved, which presents the good reliability of process control. Samples from two different industries are also analyzed with the same way. Curvatures during thermal cycles are measured and nonlinear properties are estimated in Table 4.3. Five samples are taken from industry I, and their modulus differ quite a lot with 16GPa, 36GPa, 25GPa, 20GPa and 34GPa and the degrees of nonlinearity are 1.8, 2.2, 1.8, 1.6, 2.0 respectively. Figure 4.16 shows the stress strain curves and the residual stress for these five samples are not similar. Another set from industry II with four samples shows much different nonlinear degree of 8.4, 2.0, 1.4, and 4.1. And from Figure 4.17, their stress strain behaviors are different. Meantime, their residual stresses are far away from each other. Therefore the ability of repeatability at Stony Brook is much better since many process parameters are monitored and controlled.

4.8 References

Deshpande, S., Kulkarni, A., Sampath, S. and Herman, H., (2004). "Application of image analysis for characterization of porosity in thermal spray coatings and correlation with small angle neutron scattering", *Surface and Coatings Technology,* 187(1), 6-16.

Eldridge, J.I., Morscher, G.N.and Choi, S.R., (2002), "Quasistatic vs. dynamic modulus measurements of plasma- sprayed thermal barrier coatings", *Ceramic Engineering Science Proceeding* 23, 371-378.

Friis, M., Persson, C. and Wigren, J. (2001), "Influence of particle in-flight characteristics on the microstructure of atmospheric plasma sprayed yttria stabilized ZrO_2", *Surface and*

Coatings Technology, 141 (2-3), 115-127.

Harok, V., Neufuss, K., (2001), "Elastic and inelastic effects in compression in plasma-sprayed ceramic coatings", *Journal of Thermal Spray Technology* 10 (1), 126-132.

Kulkarni, A., Vaidya., A., Goland, A., Sampath, S. and Herman, H., (2003), **"**Processing effects on porosity-property correlations in plasma sprayed yttria-stabilized zirconia coatings", *Materials Science and Engineering A,* 359(1-2), 100-111.

Kulkarni, A., Wang, Z., Nakamura, T., Sampath, S., Goland, A., Herman, H., Allen, J., Ilavsky, J., Long, G., Frahm, J., and Steinbrech, R.W. (2003), "Comprehensive microstructural characterization and predictive property modeling of plasma-sprayed zirconia coatings", *Acta Materialia,* 51 (9), 2457-2475.

Kweh, S. W. K., Khor, K. A. and Cheang, P. (2000), "Plasma-sprayed hydroxyapatite (HA) coatings with flame-spheroidized feedstock: microstructure and mechanical properties", *Biomaterials,* 21 (12), 1223-1234.

T. Streibl, A. Vaidya, M. Friis, V. Srinivasan and S. Sampath, (2006), "A critical assessment of particle temperature distributions during plasma spraying: Experimental results for YSZ", *Plasma Chemistry and Plasma Processing* 26(1), 73-102.

Wakui, T., Malzbender, J. and Steinbrech, R.W., (2004), "Strain analysis of plasma sprayed thermal barrier coatings under mechanical stress", *Journal of Thermal Spray and Technology* 13(3), 390-395.

Wang, Z., Kulkarni, A., Deshpande, S., Nakamura, T. and Herman, H., "Effects of pores

and interfaces on effective properties of plasma sprayed zirconia coatings", *Acta Materialia,* 51(18), 5319-5334.

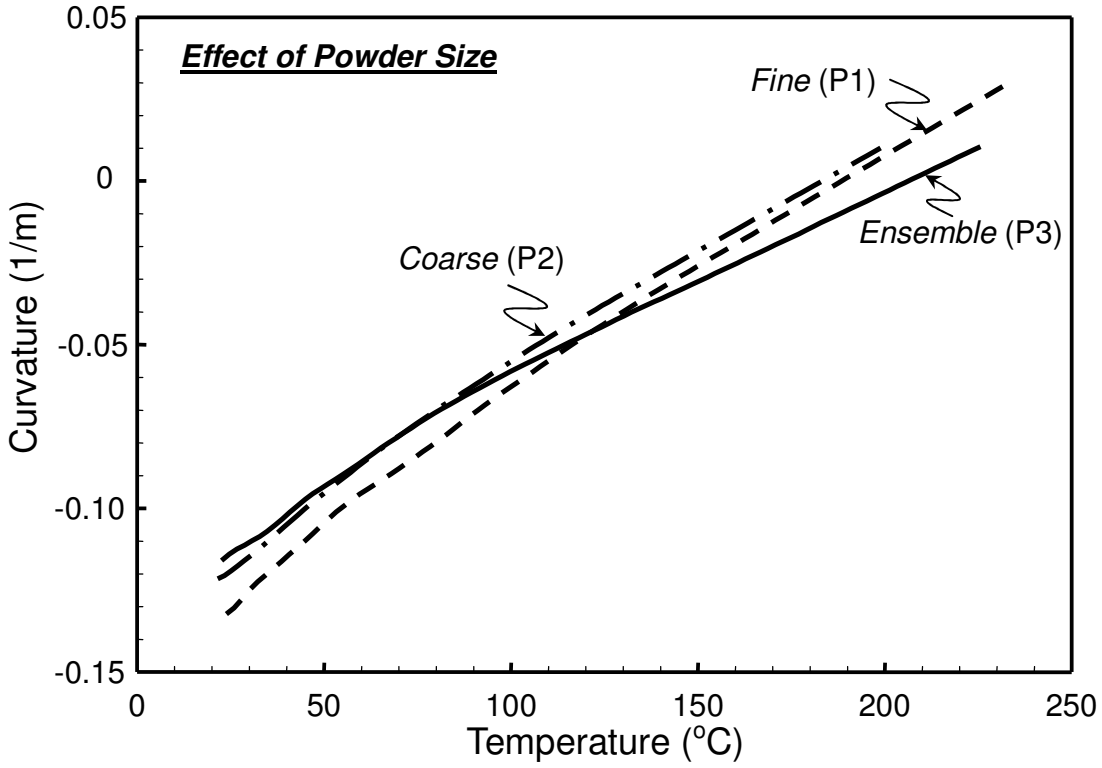

Figure 4.1. Measured substrate curvatures of different fused & crushed feedstock size processed under similar conditions, fine (10~45μm), coarse (45~75μm) and ensemble (10~75μm).

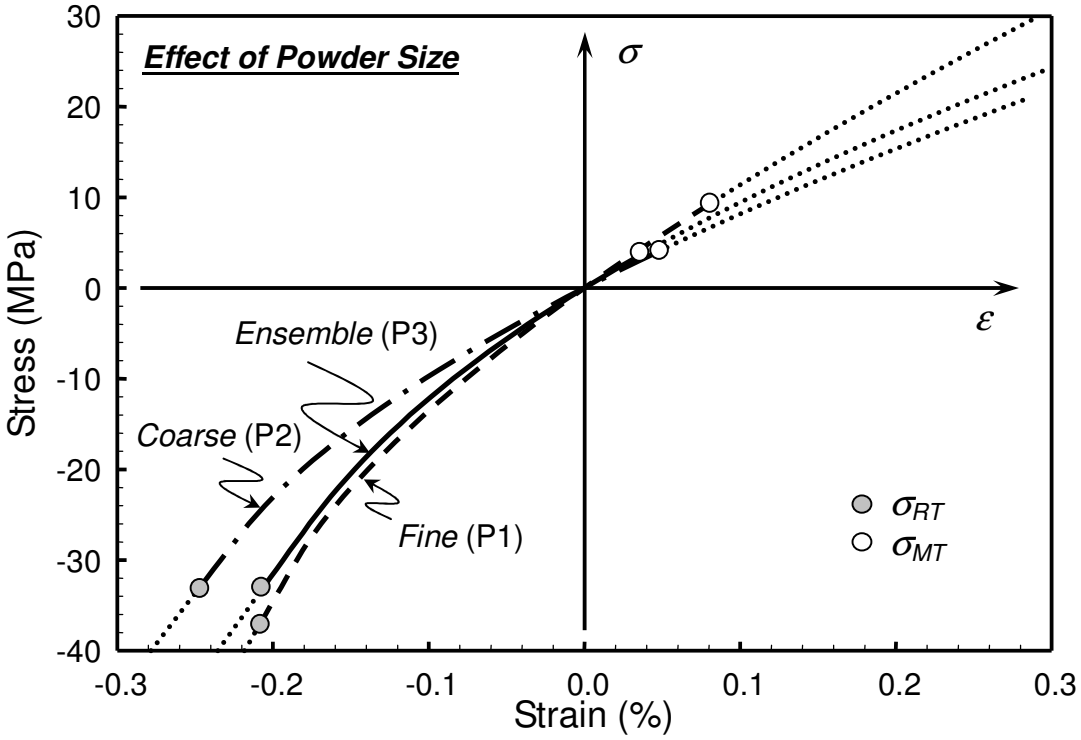

Figure 4.2. Estimated stress-strain relations of different fused & crushed feedstock size processed under similar conditions, fine (10~45μm), coarse (45~75μm) and ensemble (10~75μm).

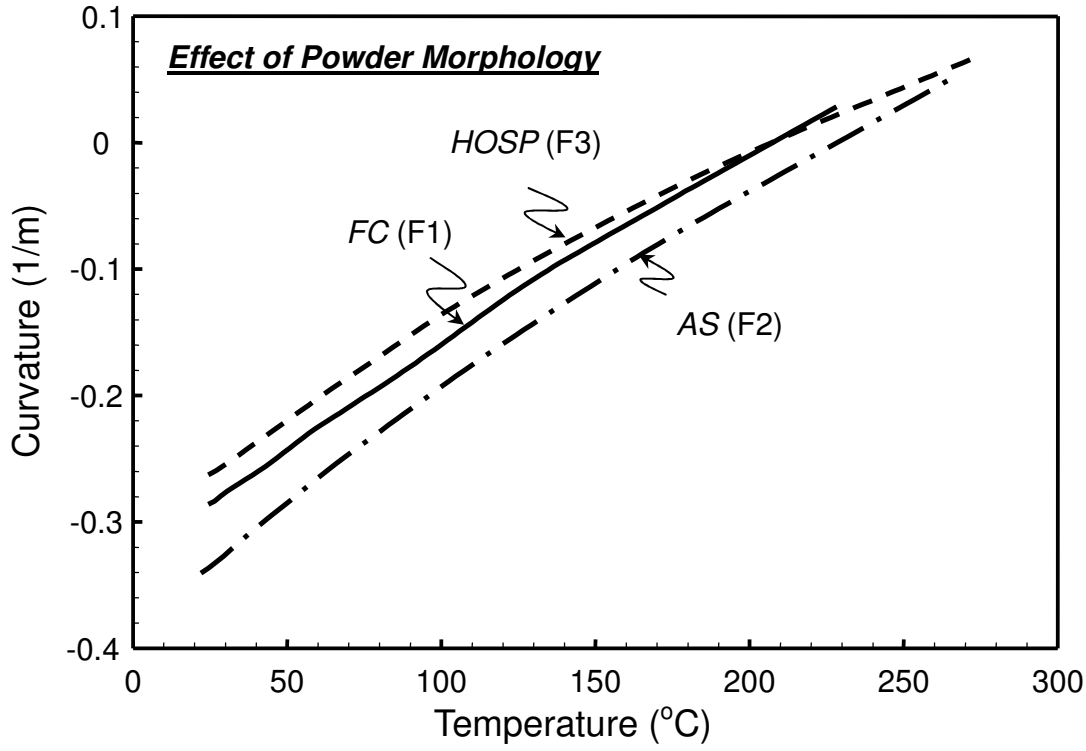

Figure 4.3. Measured substrate curvatures of different feedstock morphology processed under similar conditions for fused and crushed (FC), agglomerated and sintered (AS) and plasma densified hollow sphere (HOSP).

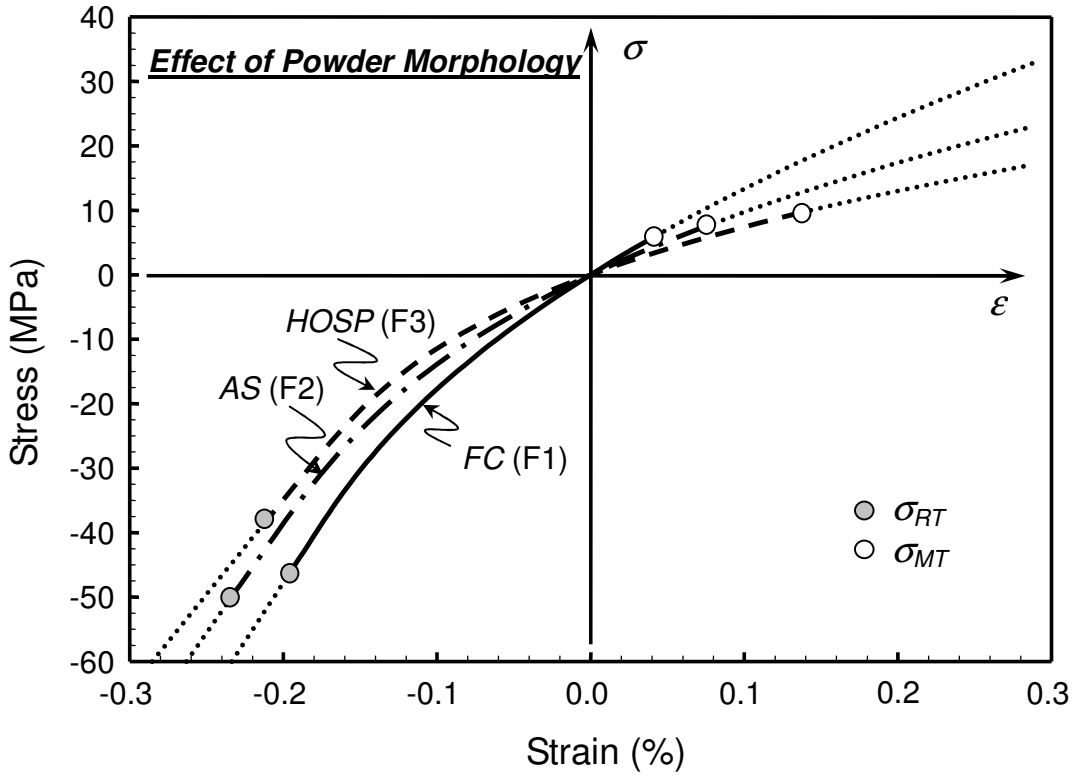

Figure 4.4. Estimated stress-strain relations of different feedstock morphology processed under similar conditions for fused and crushed (FC), agglomerated and sintered (AS) and plasma densified hollow sphere (HOSP).

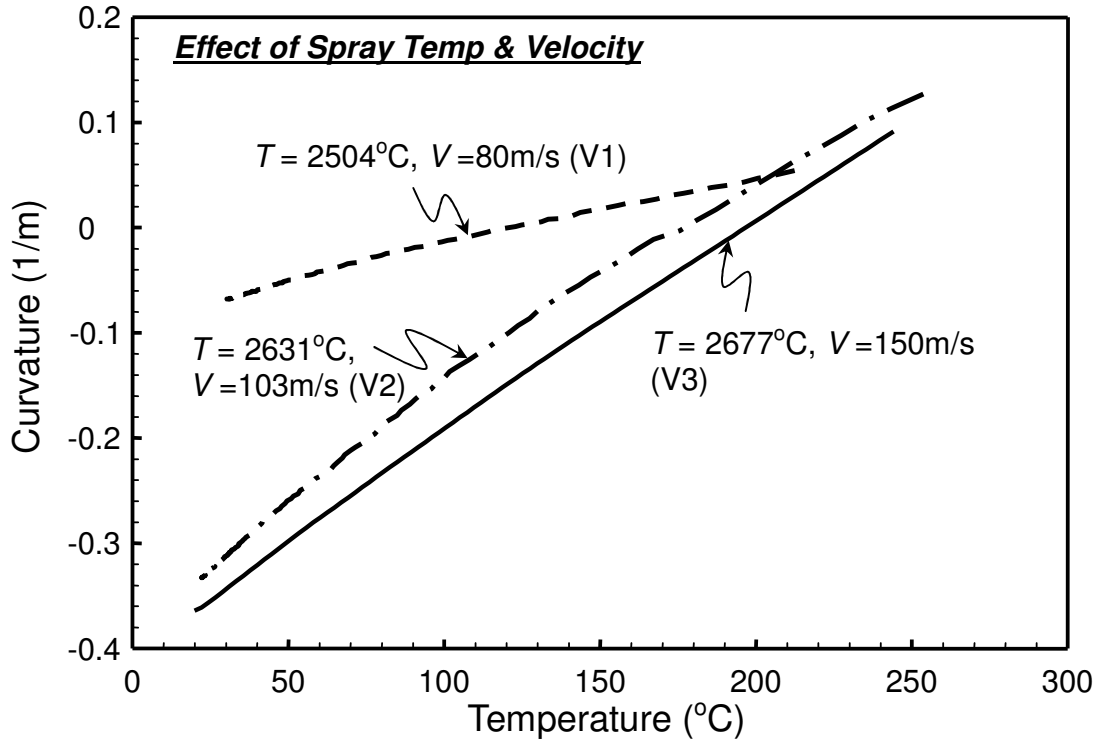

Figure 4.5. Measured substrate curvatures of different particle temperatures and particle velocities.

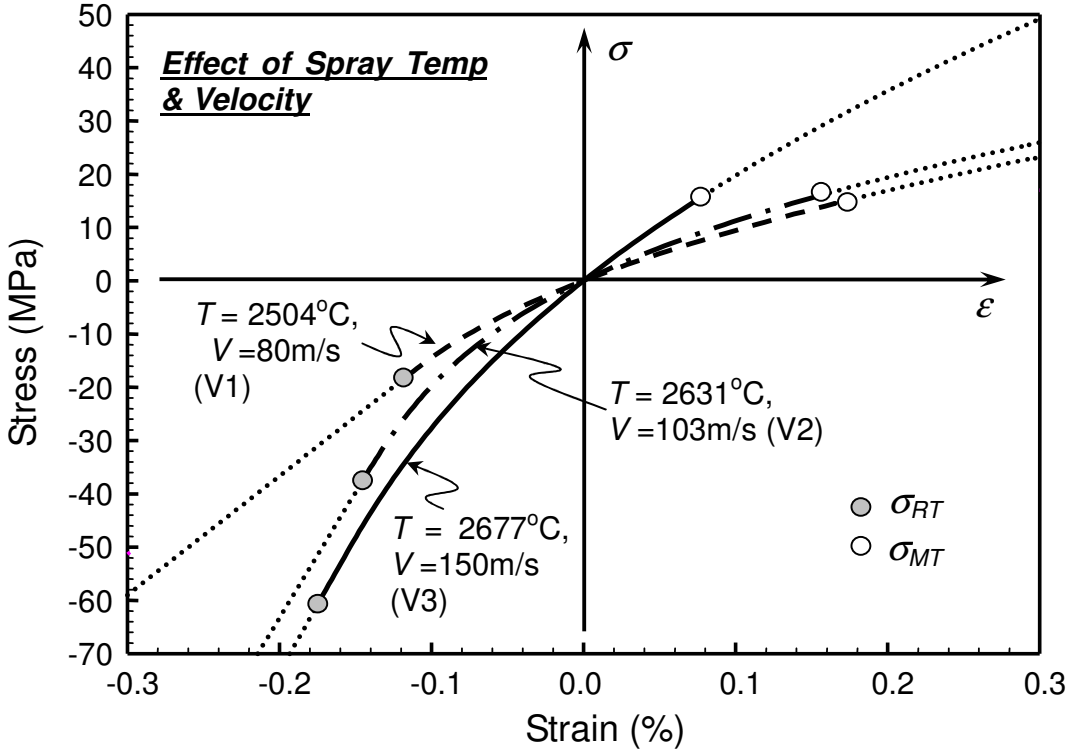

Figure 4.6. Estimated nonlinear stress-strain relations of different particle temperatures and particle velocities.

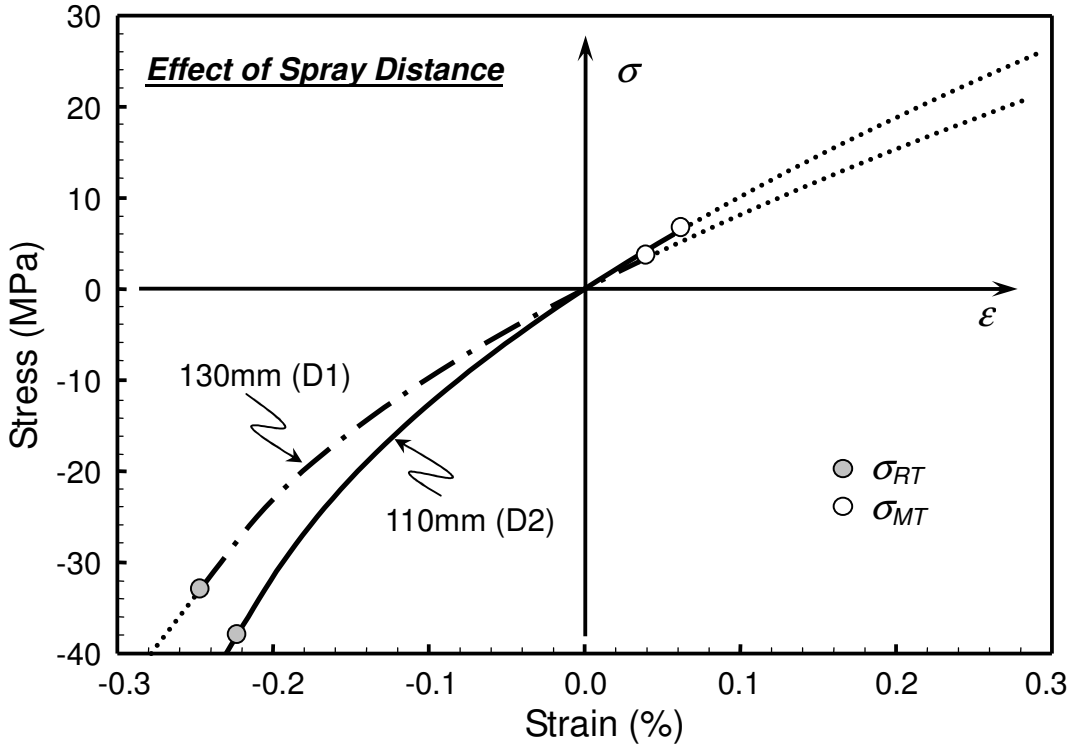

Figure 4.7. Estimated nonlinear stress-strain relations with different spray distance conditions.

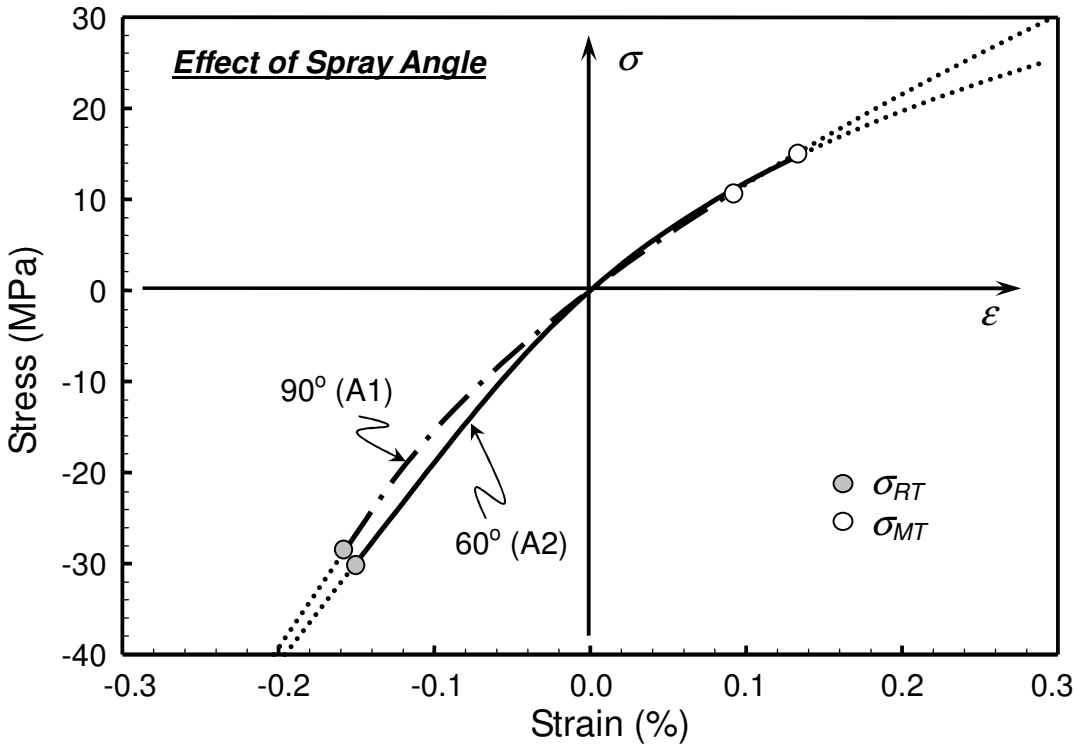

Figure 4.8. Estimated nonlinear stress-strain relations with different spray angle conditions.

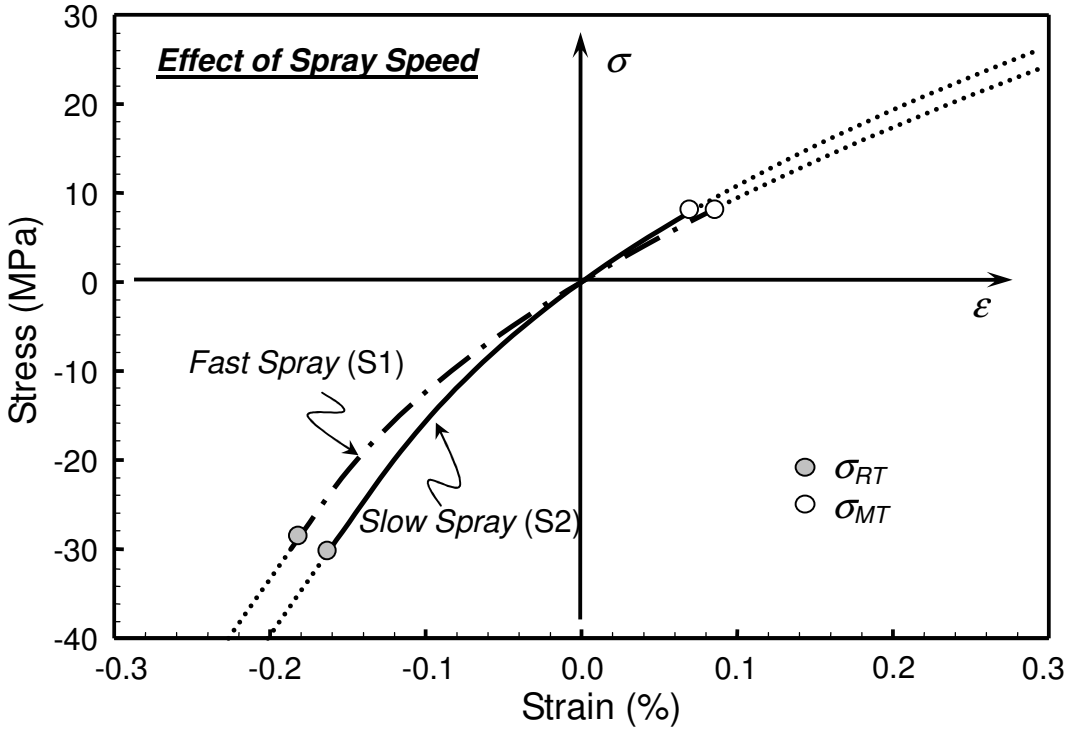

Figure 4.9. Estimated nonlinear stress-strain relations with different spray speed conditions.

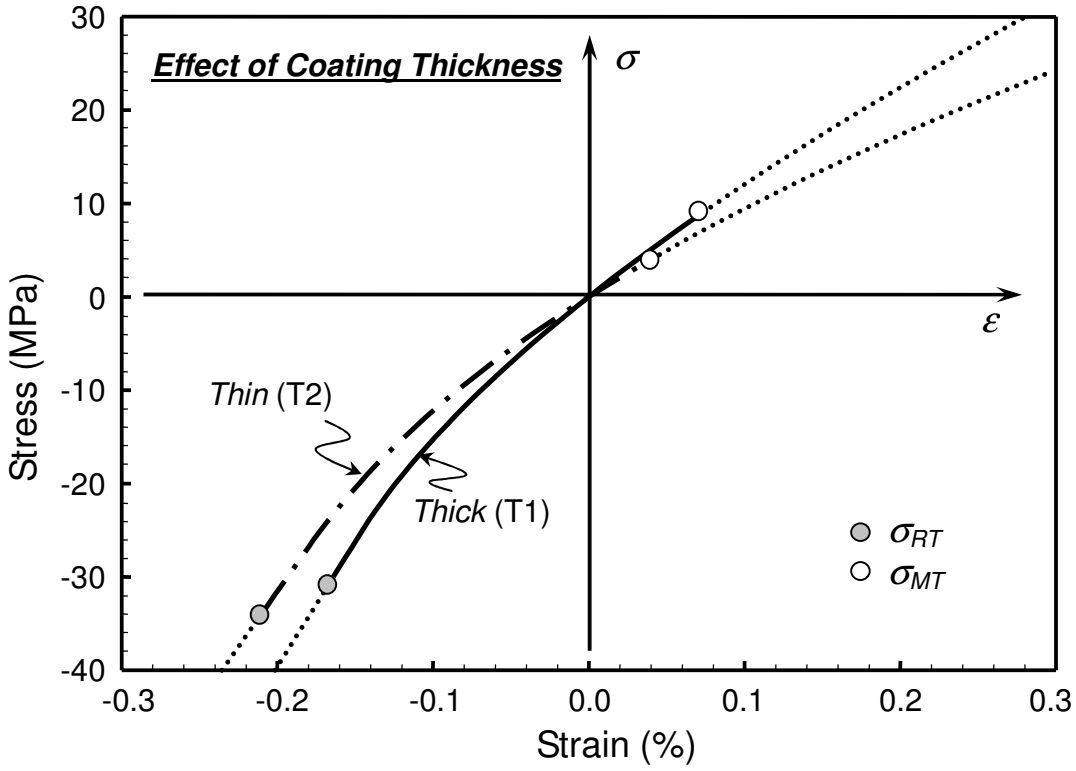

Figure 4.10. Estimated nonlinear stress-strain relations with different coating thickness conditions.

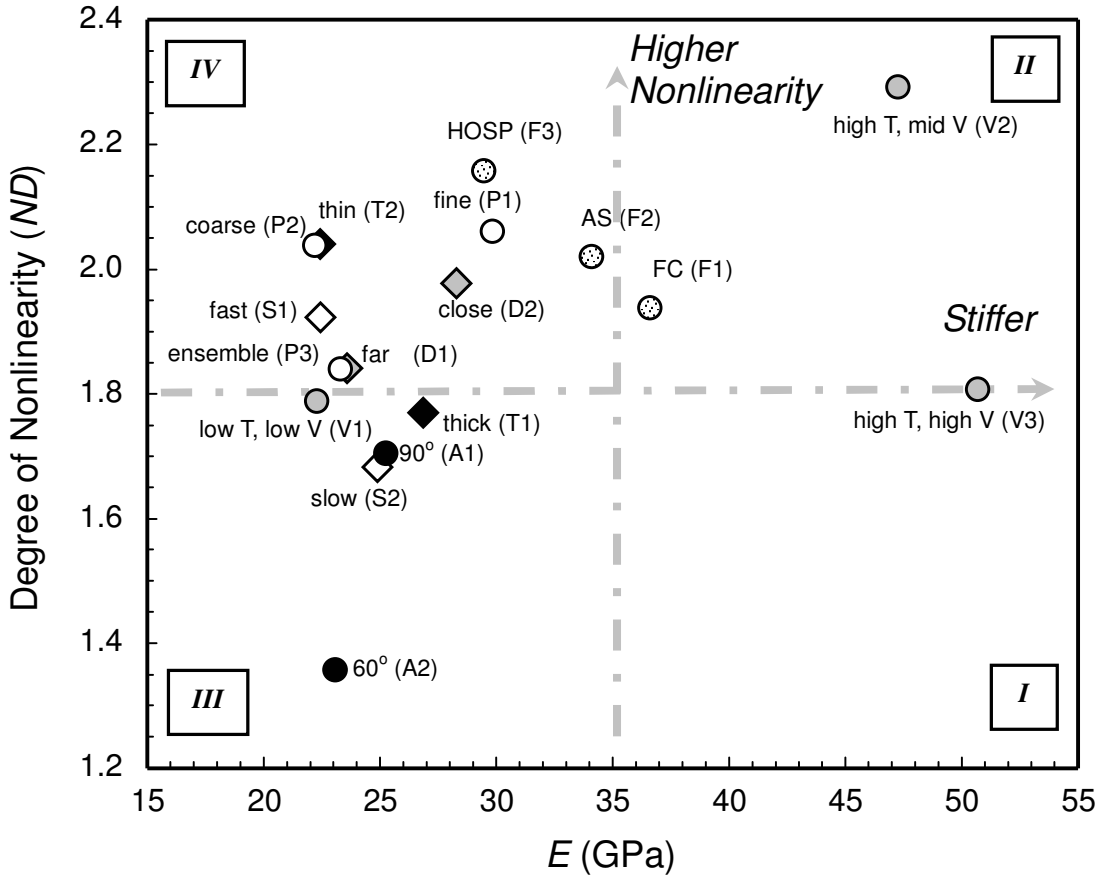

Figure 4.11. Graphical representations of nonlinear properties of TS YSZ coatings. Quadrangles symbolize, I: stiff throughout loading, II: stiff under compression but compliant under large tension, III: compliant under compression with increasing compliant under tension, and IV: compliant throughout loading.

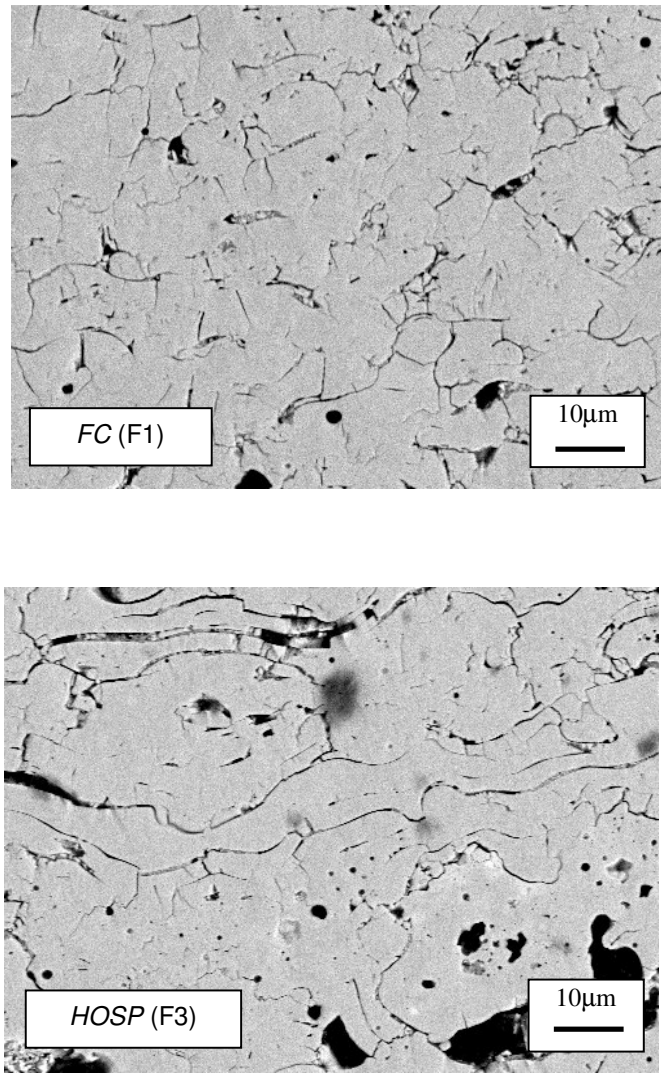

Figure 4.12. SEM images of two specimens, fused and crushed (FC) and plasma densified hollow sphere (HOSP), used to study effect of feedstock morphology.

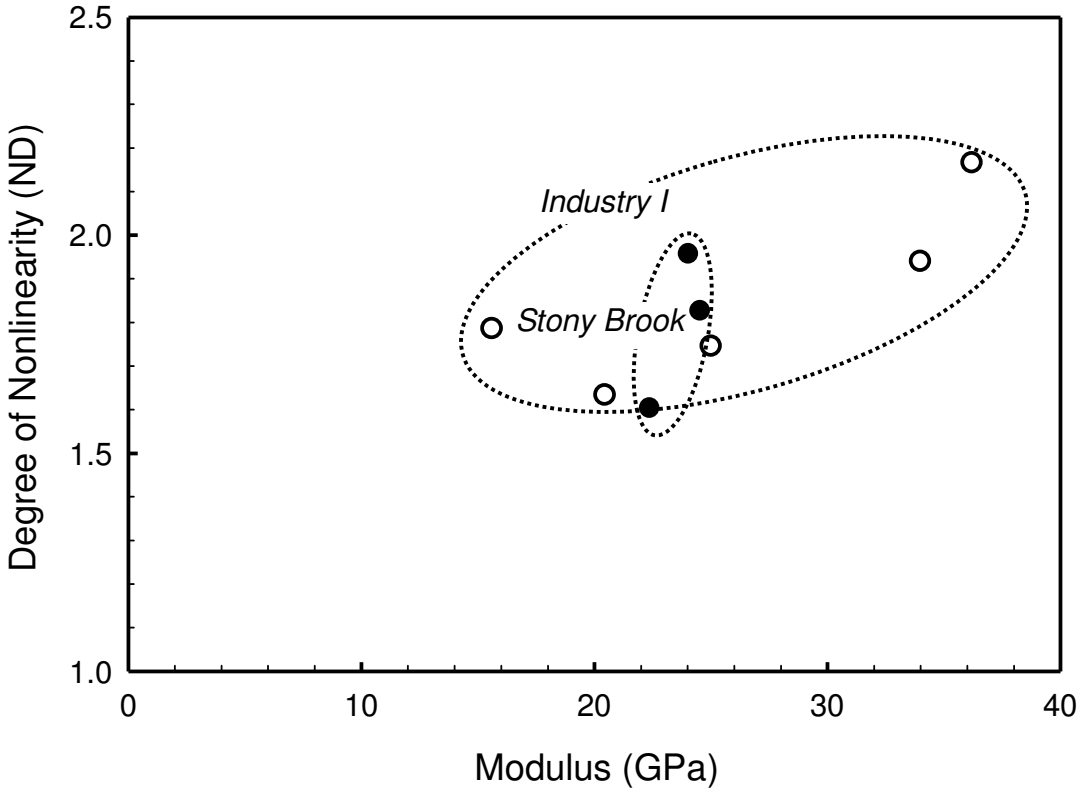

Figure 4.13. Graphical representations of nonlinear properties of TS YSZ coatings. Samples of different process reliability control from Stony Brook thermal spray center and industry I.

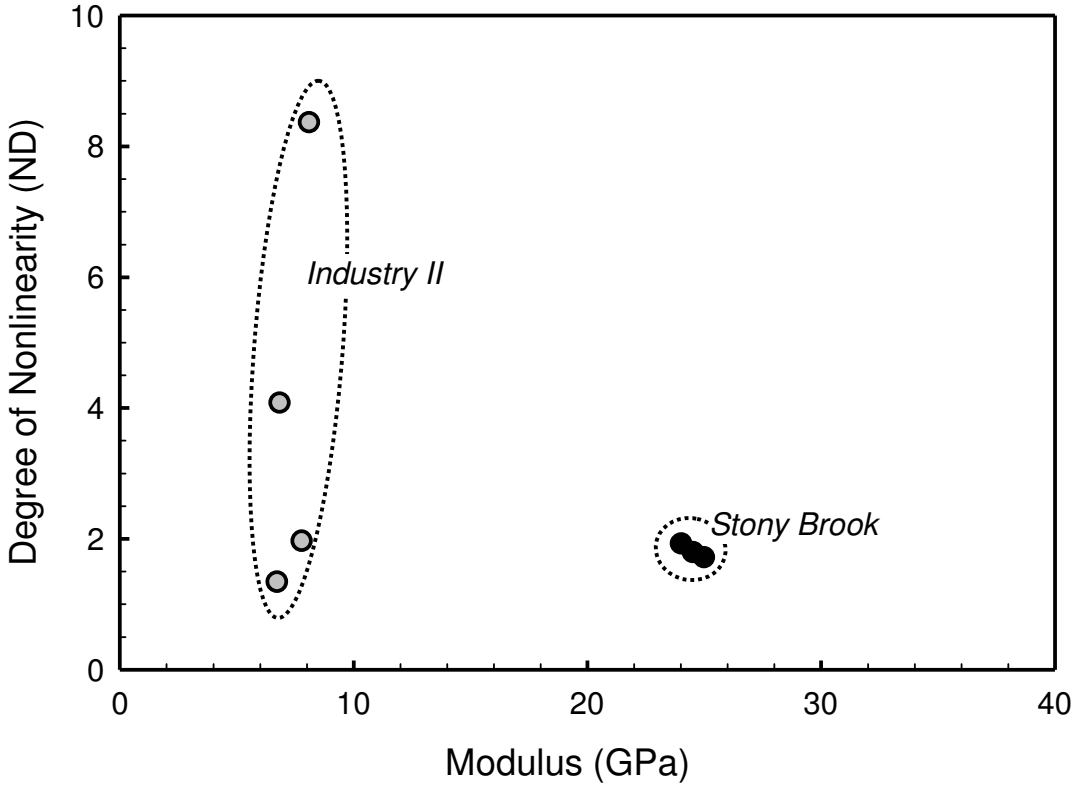

Figure 4.14. Graphical representations of nonlinear properties of TS YSZ coatings. Samples of different process reliability control from Stony Brook thermal spray center and industry II.

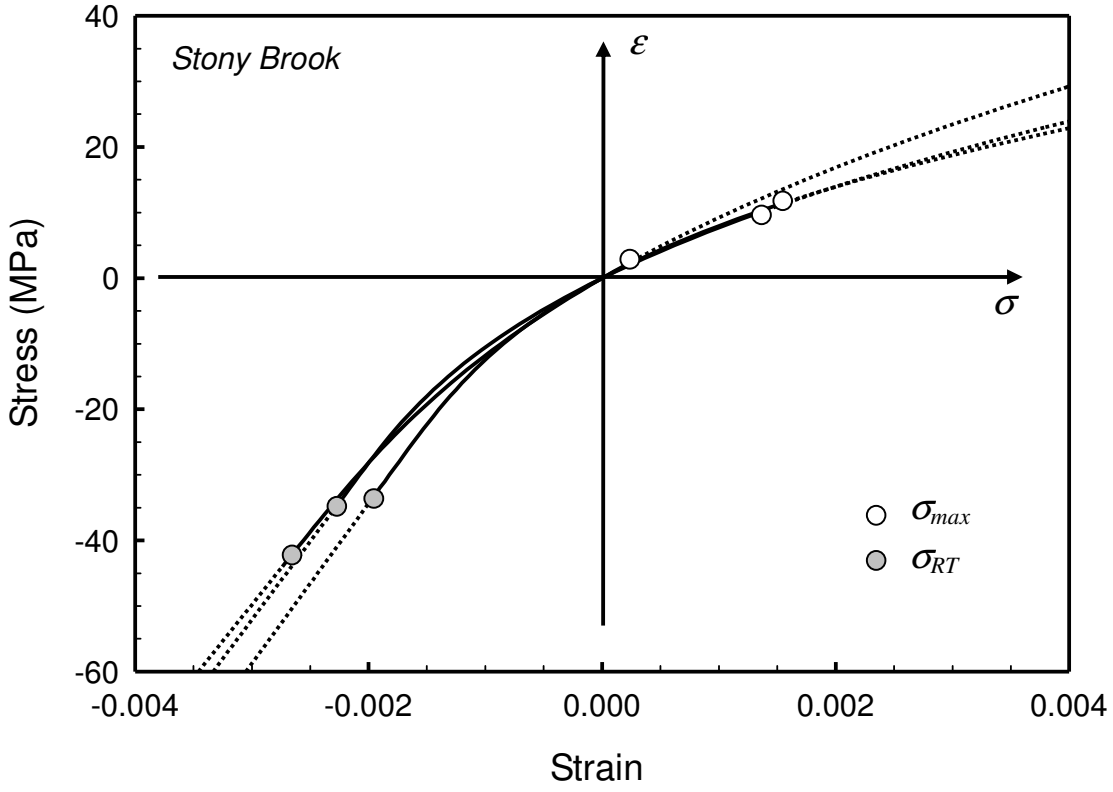

Figure 4.15. Nonlinear stress strain relation of samples from Stony Brook thermal spray center.

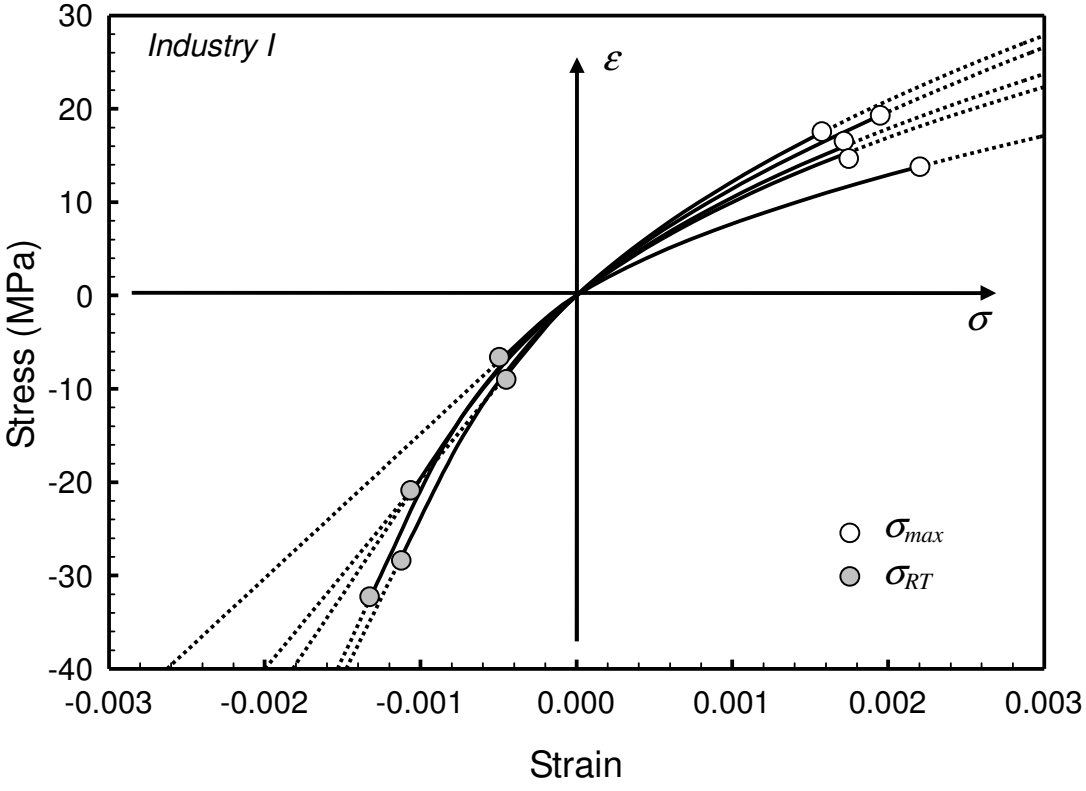

Figure 4.16. Nonlinear stress strain relation of samples from industry I.

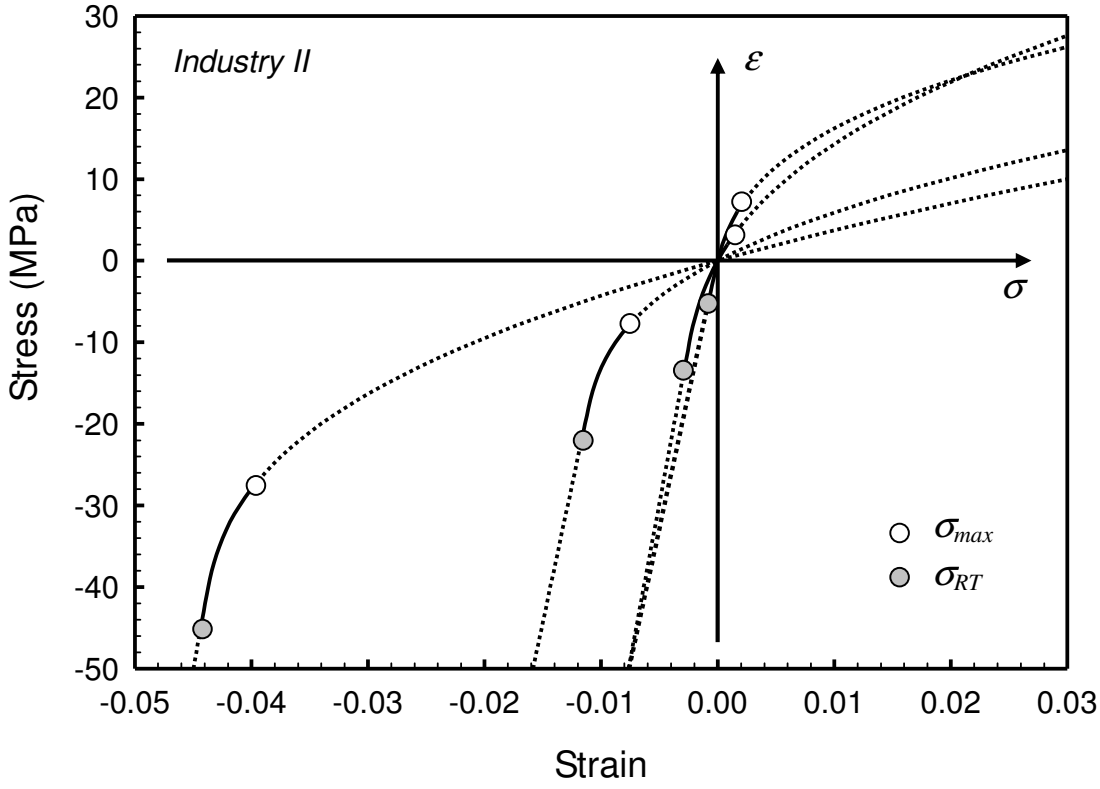

Figure 4.17. Nonlinear stress strain relation of samples from industry II.

Table 4.1. Processing conditions of various TS YSZ coatings.

	Processing Conditions					
	Size	*Powder*	*Particle T* (°C)	*Particle V* (m/s)	*Other Conditions*	*Thickness* (μm)
Effects of powder size						
P1	**Fine**	FC	2617	113	NA	433
P2	**Coarse**	FC	2587	101	NA	424
P3	**Ensemble**	FC	2547	95	NA	414
Effects of powder morphology/feedstock						
F1	Ensemble	**FC**	2659	128	NA	696
F2	Ensemble	**AS**	2661	127	NA	746
F3	Ensemble	**HOSP**	2650	127	NA	764
Effects of particle temperature and velocity						
V1	Ensemble	FC	**2504**	**80**	NA	434
V2	Ensemble	FC	**2631**	**103**	NA	815
V3	Ensemble	FC	**2677**	**150**	NA	615
Effect of spray distance					*distance*	
P3(D1)	Ensemble	FC	2547	95	**130mm**	414
D2	Ensemble	FC	2642	107	**110mm**	403
Effect of spray angle					*angle*	
A1	Ensemble	FC	2547	95	**90°**	776
A2	Ensemble	FC	2515	86	**60°**	660
Effect of spray speed					*speed*	
S1	Ensemble	FC	2568	100	**450mm/s**	348
S2	Ensemble	FC	2564	99	**150mm/s**	373
Effect of coating thickness						
T1	Coarse	FC	2576	102	NA	**960**
P2(T2)	Coarse	FC	2587	101	NA	**424**
P3 and D1, P2 and T2 are identical. Unless noted: feed rate = 30g/min, spray distance =130mm, angle = 90°, speed = 300mm/s						

Table 4.2. Estimated properties of various TS YSZ coatings.

	Estimated Properties					
	E_c (GPa) (±2GPa)	σ_N (MPa) (±3MPa)	n (±0.2)	σ_T (MPa) (±3MPa)	σ_{RT} (MPa) (±3MPa)	*ND*
Effects of powder size						
P1	30	37	1.7	-29	-37	2.1
P2	22	34	1.9	-27	-33	2.0
P3	23	43	2.2	-27	-33	1.8
Effects of powder morphology/feedstock						
F1	37	54	2.2	-38	-46	1.9
F2	34	52	2.9	-43	-51	2.0
F3	29	37	3.2	-32	-38	2.2
Effects of particle temperature and velocity						
V1	22	32	2.2	-17	-18	1.8
V2	47	45	3.1	-39	-40	2.3
V3	51	85	2.4	-53	-60	1.8
Effect of spray distance						
P3(D1)	23	43	2.2	-27	-33	1.8
D2	28	45	2.1	-34	-39	2.0
Effect of spray angle						
A1	25	50	1.9	-23	-28	1.7
A2	23	55	3.9	-26	-29	1.4
Effect of spray speed						
S1	23	36	2.0	-24	-30	1.9
S2	25	47	2.4	-25	-30	1.7
Effect of coating thickness						
T1	27	50	1.8	-25	-30	1.8
P2(T2)	22	34	1.9	-27	-33	2.0

Table 4.3. Estimated properties of YSZ coatings for repeatability.

Estimated Properties					
E_c (GPa) (±2GPa)	σ_N (MPa) (±3MPa)	n (±0.2)	σ_T (MPa) (±3MPa)	σ_{RT} (MPa) (±3MPa)	*ND*
Stony Brook Thermal Spray Center					
22	65	2.8	-40	-44	1.6
24	40	3.1	-29	-34	1.8
24	38	2.6	-30	-35	1.9
Industry I					
16	14	2.0	-3	-6	1.8
36	33	3.0	-26	-32	2.2
25	31	2.6	-16	-21	1.8
20	25	1.9	-3	-7	1.6
34	35	2.5	-21	-28	2.0
Industry II					
8	12	2.6	-42	-45	8.4
8	14	2.6	-12	-14	2.0
7	12	3.0	-3	-5	1.4
7	11	2.8	-19	-21	4.1

Chapter 5

Anelastic Stress Strain Behavior of Thermal Sprayed Coatings

5.1. Introduction

Thermally sprayed ceramic coatings are fabricated with melted or semi-melted particles that solidify on substrates. The successive spray generates a unique lamellar microstructure with pores and cracks. The microstructure of ceramic coating is characterized as the lamellae splats exist with interlamellar and globular pores, inter-splat and intra-splat microcracks. Current substrate-curvature tests show ceramic coatings exhibit a nonlinear mechanical behavior and the mechanical properties depend on the amplitude of applied stress or strain. The unique structures of ceramic coatings especially microcracks are also responsible for nonlinear mechanical response with compression loads. The extension of microcracks may also lead to lowering of coating modulus. Substrate curvature measurements show coating nonlinear deformation during thermal cycle. Curvature measurements have also revealed that thermally sprayed ceramic coatings exhibit hysteresis during stress cycling. The stress strain relations tend to be different under cyclic loading but after unloading the strain can be fully reversed. It appears crack face frictions are responsible for this phenomenon.

The mechanism is similar to the internal frictional resistances generated by closed cracks described by Lawn and Marshall (1998). The energy due to friction can be dissipated internally. Pan and Horibe (1997) found that zirconia ceramics exhibit strong anelastic behavior. These nonlinear and hysteresis behavior can be characterized as anelastic behavior and such behavior is expected to improve material strength and

toughness since it can possess more anelastic strain at high stress level (Pan et al., 1997). The anelastic stress strain relations of ceramic coatings is attributable to sliding friction at microcracks existed inside of coatings (Horri and Nemat-Nasser, 1986, Nemat-Nasser and Obata, 1988, Lawn and Marshall, 1998). The microcracks lead to modulus reduces and the frictional sliding results in the hysteresis upon unloading. The nonlinear stress strain behavior of solids that microcracks may propagate under a large tensile stress can be found in the works of Horri and Nemat-Nasser (1986) and Nemat-Nasser and Obata (1988).

Many materials show anelastic behavior with the modulus. For some metals, energy is stored in the material but it is dissipated therefore the element is not returned to its original position. For example, bcc metals such as niobium and niobium alloys, interstitial solute atoms cause local strain distortion of tetragonal symmetry. When an external stress is applied, these interstitial atoms are redistributed among the different sites, causing energy loss (Niemeyer et al., 2005). Crystalline materials exhibit anelastic behavior, which is time-dependent and hence not purely elastic but completely recoverable (Yagmur et al, 2007). Emel'lyanov et al. (2000) observed the anelastic behavior of martensitic Cu-Al-Ni crystals due to interface interactions under high energy impact by plane shock wave. Such behavior results from internal friction and there is a difference of modulus between loading an unloading.

In this study, we will elucidate the mechanisms that govern anelastic behavior of YSZ ceramic coatings with experimental data, analytical models and finite element simulations.

5.2. Experimental Procedure

In the present experiments, the curvature-temperature records from post-deposition thermal cycle are also utilized to study anelastic property. Typical in-plane dimensions of specimens are 230mm × 25.4mm. In this study, the thickness of coating is 730 μm while that of substrate is 3.35 mm. The feedstock is Fused and Crushed (FC) powder with 8% Yattria and was sprayed at average velocity of 115 m/s and particle temperature of 2650 ^{o}C. Feed rate was set as 30 g/min. The current and voltage are 550A and 75V, respectively. Initially, coating and substrate are thermal cycled by a gas torch gun moving across YSZ coating surface until the temperature reaches about 250^{o}C-300 ^{o}C, which is measured by three thermo-couple attached to the substrate bottom. At the bottom of substrate, three Aromat LM-10 (Panasonic Electric Works) sensors are also attached to measure the deflections with 1 μm resolution. After heating, the specimen is cooled down to the room temperature under forced air convection. Typically it takes 2 min to heat up and more than 7 min to cool down. The detail description was provided in Matejicek and Sampath (2003). However, there are large fluctuations of curvature measurements while specimen is heated. They are produced by the moving hand torch and the kinetic energy of flowing gas.

In order to obtain smooth curvature record in more stable heating environment during thermal cycle, a measurement was carried out with a surface profilometer Tencor FLX-2900 (KLA Tencor) laser scanning system in a furnace. Here both heating and cooling rates were set very low so that the thermal equilibrium was maintained throughout the test. Since the difference of thermal expansion coefficient (CTE) between YSZ coating and Al6061 substrate, curvature evolves as temperature changes as shown in

Figure 5.1. At room temperature, CTEs of substrate and coating are $23\times10^{-6}/^{o}C$ and $10\times10^{-6}/^{o}C$, respectively. It can be observed that the curve is steeper at lower temperature, which suggests higher stiffness of coating near the room temperature. Since the properties of YSZ are not thermally dependent in this temperature range, the nonlinearity is likely to be driven by ceramic microstructural attributes. In addition to the nonlinear elastic behavior described for TS YSZ coatings, the curvature measurements suggest hysteresis behavior during thermal cycle and clearly exhibit different paths under heating and cooling.

5.3. Anelastic Stress Strain

5.3.1 Stress Strain Relation from Curvature Measurements

The source of nonlinearity appears to arise from unique microstructural attributes of thermally sprayed ceramic coatings. As many micro-cracks and weak interfaces are present in the coatings, their opening and closing during stress changes promote the nonlinear responses. Under sufficient compressive load, crack faces are closed and the coatings exhibit higher apparent stiffness while opened cracks under tensile state produce more compliant response (Kroupa and Dubsky, 1999, Kroupa and Plesek, 2002). Since microcracks have various orientations, sizes and different local stresses, closings and openings do not occur simultaneously. This feature results in a smooth variation of effective modulus rather than a sudden change expected from a single crack model. At room temperature, high residual compressive stress keeps many cracks to be closed. The nonlinear behaviors of atmospheric plasma sprayed (APS) ZrSiO4 were also observed under four-point bend tests (Harok and Neufuss, 2001). Waki et al. (2004) also reported the nonlinear stress-strain responses of plasma sprayed zirconia coating using the laser

speckle strain-displacement gauge (SSDG). Wang et al. (2006) observed nonlinear stress-strain relation of thermally sprayed metallic Ni–45Cr coating under tensile loading along the through-thickness direction due to its lamellar features.

In order to describe the coating's nonlinear behavior, a phenomenological constitutive model is introduced. Based on the experimental observations and likely physical causes of nonlinearity (cracks and defects), the stress-strain relation is first expected to be asymmetric under tension and compression. Second, under very large compression, the response should be nearly linear since many cracks and thin defects are closed. Third, the transitions from linear to nonlinear generally do not occur at the zero stress ($\sigma = 0$). With these factors, the uniaxial stress-strain model is proposed in chapter 3. Essentially, it is a combination of linear elastic and modified Ramberg-Osgood models. Here E is the Young's modulus, n is the power-law exponent and σ_N is the reference stress (not yield stress). The transitional stress σ_T represents where the change from linear to nonlinear relations occurs. In most tests conducted for YSZ, the transitional stresses are in compression (i.e., $\sigma_T < 0$). The relation turns out to be very versatile to describe the stress-strain behavior of coatings with minimum number of parameters (E, σ_N, n and σ_T). The characterization of such nonlinear properties was published and robust procedure was proposed based on biomaterial beam theory and inverse analysis.

Using the curvature measurements from both heating and cooling, separate stress-strain relations are estimated. In the estimation, the initial and maximum temperatures are taken to be T_{init} = 30°C and T_{max} = 285°C, respectively. Also both the estimated curves from heating and cooling are shifted so that they merge at the maximum

temperature. Then they are adjusted so that zero strain ($\varepsilon = 0$) falls in the middle of two curves at $\sigma = 0$. Such a shift makes the estimated stress-strain relation to be inconsistent with the assumed model (3.1). Thus a rigorous estimation would require some modifications in the stress-strain model as well as the estimation process. However since the shifting or offset of each curve is limited, additional modifications were not taken here. In Figure 5.2, it is worth noting that two curves also merge at the initial temperatures although they were estimated independently.

5.3.2 Analytical Solutions of Stress Strain Relation

5.3.2.1. Contact Stress

Now consider a solid containing one single elliptical crack shown in Figure 5.3 with crack length $2a$ and oriented with angle θ relative to the x direction With opening 2δ, the crack tends to close under external compressive stress σ. From the exact solution for an elliptical crack in two-dimensional elasticity (Muskhelishvili, 1953, Walsh, 1965, Kroupa and Dubsky, 1999), the contact pressure σ_c is related to the applied compression and for θ =90^o

$$\sigma_c = \begin{cases} \dfrac{E\delta}{2a} & plane\ \ stress \\ \dfrac{E\delta}{2(1-\nu^2)a} & plane\ \ strain \end{cases} \tag{5.1}$$

Here, ν is Poisson ratio. However, microcracks inside of coating are not perfectly perpendicular to applied compressive stress but oriented with some angle. Thus considering the crack orientation, according to the normal stress along crack surface, the normal stress is

$$\sigma_c = \frac{E\delta}{2a\sin^2\theta} \tag{5.2}$$

And considering the Poisson ratio effect, contact stress can be adjusted as,

$$\sigma_c = \frac{E\delta}{2a(\sin^2\theta + \nu\cos^2\theta)} \tag{5.3}$$

5.3.2.2. Stress Strain Relation before Crack Closing

In present study, pores are not considered because those defects can not be closed under current thermal cycle process. According to stress strain relation of section 2, the transitional stress is σ_T = -49 MPa and δ/a can be determined as ~≤ 1/400 (= $E_c / 2\sigma_c$). The cracks with δ/a > 1/400 is ignored since they cannot be kept closed under transitional stress.

The effective modulus of a solid with cracks depends on its porosity, but the porosity of microcracks is very small if pores are not included. Except for the porosity, the shape factor of cracks play a leading role in effective modulus. Kachanov et al. (1994) derived the detail effective modulus introducing the second parameter *eccentricity*. And non-interacting microcracks are assumed in their studies. For crack perpendicular to the horizontal axis (θ=90^o), effective modulus in *x* direction can be expressed as

$$E_{eff} = \frac{d\sigma}{d\varepsilon} = \frac{E}{1 + \dfrac{3p + 2q}{1 - p}} \tag{5.4}$$

Here, E, E_{eff} are the bulk and effective modulus of solid. p is the porosity and q is the shape factor – *eccentricity*. They can be computed as

$$p = \frac{\pi a\delta}{A} \quad \text{and} \quad q = \frac{\pi(a-\delta)^2}{A} \tag{5.5}$$

A is the total area of solid $A = 4L^2$. If the defects are circular pores, the shape factor q reaches zero ($a = \delta$). Then the effective modulus of solid only depends on porosity. If the crack is randomly orientated with an angle θ, the effective modulus is

$$E_{eff} = \frac{d\sigma}{d\varepsilon} = \frac{E}{1 + \dfrac{3p + 2\pi(a-\delta)^2 \sin^2\theta / A}{1-p}} \tag{5.6}$$

5.3.2.3 Stress Strain Relation of Closed Crack

In our present study, the maximum tensile stress applied to coating during thermal cycles is small so that the propagation of microcracks is not considered. Lawn and Marshall (1998) derived the solutions for an isotropic body containing non-interacting cracks without crack extension based on the analysis of complementary energy density, which include crack energy density and complementary energy density for uncracked solid.

From Lawn and Marshall (1998), crack energy in two dimensions can be expressed as

$$\omega(\sigma,\theta) = \begin{cases} \pi\eta a^2 \sin\theta\cos\theta(\sin\theta\cos\theta - \mu\sin^2\theta)\sigma^2 / E & 0 \le \sigma \le \sigma^{\max} \\ \pi\eta a^2 \sin\theta\cos\theta(\sin\theta\cos\theta + \mu\sin^2\theta)\left(\sigma - \sigma^{slid}\right)^2 / E & 0 \le \sigma \le \sigma^{slid} \end{cases} \tag{5.7}$$

Here, σ is applied stress, η is dimensionless crack geometry constant for plane stress η=4/3. a, θ and μ are crack length, orientation and coefficient of friction. E is Young's modulus of uncracked solid. For sliding a crack, the condition of $\theta < \arctan(1/\mu)$ must be satisfied. σ^{max} is the maximum stress during loading and σ^{slid} represents the transition point which crack status changes from stick to sliding. σ^{slid} is defined as $\sigma^{slid} = \sigma^{\max}(\sin\theta\cos\theta - \mu\sin^2\theta)/(\sin\theta\cos\theta + \mu\sin^2\theta)$. On unloading, the

friction reverse and crack faces remain stationary. Thus the effective modulus is the same as bulk material. The stress strain relations can be derived (Lawn and Marshall, 1998).

$$\frac{d\sigma}{d\varepsilon}=\begin{cases}\dfrac{E}{1+2\pi\eta a^2\sin\theta\cos\theta(\sin\theta\cos\theta-\mu\sin^2\theta)/A} & 0\le\sigma\le\sigma^{\max}(loading)\\ E & \sigma^{\max}\le\sigma\le\sigma^{slid}(unloading)\\ \dfrac{E}{1+2\pi\eta a^2\sin\theta\cos\theta(\sin\theta\cos\theta+\mu\sin^2\theta)/A} & 0\le\sigma\le\sigma^{slid}(unloading)\end{cases} \quad (5.8)$$

There, A is the area of solid.

5.3.2.4 Full Stress Strain Relation during Loading and Unloading

Combining the stress strain relations of before and after crack closure, the full normalized stress strain relation for a single crack with initial opening can be written as

$$\sigma/\sigma^{\max}=\begin{cases}\dfrac{\varepsilon/(\sigma^{\max}/E)}{1+\dfrac{3\pi a\delta/A+2\pi(a-\delta)^2\sin^2\theta/A}{1-\pi a\delta/A}} & 0\le\sigma\le\sigma_c(loading)\\ \dfrac{\varepsilon/(\sigma^{\max}/E)}{1+2\pi\eta a^2\left(\sin^2\theta\cos^2\theta-\mu\sin^3\theta\cos\theta\right)/A} & \sigma_c\le\sigma\le\sigma^{\max}(loading)\\ \varepsilon/(\sigma^{\max}/E) & \sigma^{\max}\le\sigma\le\sigma^{slid}(unloading)\\ \dfrac{\varepsilon(\sigma^{\max}/E)}{1+2\pi\eta a^2\left(\sin^2\theta\cos^2\theta+\mu\sin^3\theta\cos\theta\right)/A} & \sigma_c\le\sigma\le\sigma^{slid}(unloading)\end{cases} \quad (5.9)$$

Figure 5.4 shows normalized stress strain curves according to (5.9) for one example with a=0.632L, which gives crack density ($\rho=a^2/A$) ρ=10%, θ = 45^o (θ=arctan (1.0)) and μ = 0.5. The aspect ratio of δ/a with 1/200 is chosen arbitrarily in order to see different stress strain slope during loading and unloading. Material modulus and Poisson ratio are set arbitrarily as E =100GPa and ν =0.3. The hysteresis loop of stress strain is clearly shown. With initial crack opening, crack faces will contact under a certain compressive stress which depends on the crack aspect ratio δ/a and orientation θ.

From (4), the contact stress is -0.385GPa. And the effective modulus can be calculated as 0.759*E*. Then the crack begins to slide until the maximum compression with the slope of 0.905*E*. As soon as unloading begins, the direction of friction changes to the opposite direction. Then the crack faces remain stationary and the effective modulus is the same as the Young's modulus of material *E*. When the compression reduces to σ^{slid} = -1.30GPa, crack faces start to slide again with reduced modulus 0.761*E*. When the stress reaches contact pressure, crack faces open and stress strain follow the same path as loading process. Figure 5.5 shows tangent modulus at different stages during loading and unloading. At stage I, crack surfaces remain open and the modulus reduce results from the defect including porosity and eccentricity effect. Stage II represents the sliding process during loading after closing crack. At this step, effective modulus is larger than stage I because of zero porosity but still smaller than bulk material modulus *E*, which is due to the crack sliding with friction. There is no modulus reducing at stage III after unloading and crack remain stationary without any sliding. When crack starts sliding again with opposite direction to loading backward, material shows more compliant than sliding during loading, shown in Stage IV. Stage V is the same as stage I after crack open.

5.3.2.5. Effect of Crack Aspect Ratio and Friction Coefficient

The effect of friction of coefficient on the stress strain behavior is shown in Figure 5.6 for μ = 0, 0.25, 0.5, 0.75, 1.0 with fixed a=0.632 L, δa = 1/200 and θ = 45°. Before contact stress, all curves have the stress strain relation with the slope of 0.759*E*. Once crack close, different friction coefficients lead to different stress strain behaviors. At μ = 0, the loading and unloading follow the same curve due to no frictional sliding with slope of 0.827*E* because of the crack closing. At μ = 1.0, because the crack cannot slide

and remain stationary during loading and unloading. The effective modulus for μ = 1.0 is the bulk material modulus E. For μ = 0.0 and 1.0, the tangent modulus during loading is the same as unloading after crack surfaces contact. Different tangent modulus exist during loading/unloading for μ = 0.25, 0.5 and 0.75. With the increasing of μ, the slopes of loading increase and the sliding stress σ^{slid} decrease. The tangent modulus decreases as μ increases after back-sliding during unloading, shown in Figure 5.7.

Figure 5.8 shows the effect of crack aspect ratio δ/a effect on the stress strain behavior with δ/a = 0, 1/500 and 1/200 with a=0.632 L, θ = 45^{o} and μ = 0.5. Different aspect ratios lead to crack will close at different applied stress and for δ/a = 0, crack can slide at the beginning loading. Crack with δ/a = 1/500 will contact at σ_c = -0.154GPa, less than the one with δ/a = 1/200 (σ_c = -0.385GPa). Before closure, the tangent modulus for δ/a = 1/500 is 0.7605E, which is a little bit larger than the one with 1/200 (0.759E), shown in Figure 5.9. Once the cracks remain contact, they will slide with exactly same tangent modulus of 0.905E. During unloading, initially bulk material modulus E is shown due to the sticking cracks and then they slide backward until contact stress also with same tangent modulus. Finally all cracks go back to the original point. With the increasing of crack aspect ratio, hysteresis loop deceases but material shows stiffer stress strain behavior.

5.3.2.6. Stress Strain Relation of Solid with Multiple Cracks

When a solid contains many crack with different crack aspect ratio δ/a, random orientation θ and different coefficient of friction, then the contact stress from (4) for each crack will be different and that means every crack will close at different applied stresses.

The anelastic stress strain behavior can be smooth and continuous. But it is more complicated to calculate the corresponding stress strain relation because it is possible that when some crack still keep open, some of them already contact and start sliding. Therefore the compliant response should include the open cracks and the sliding cracks. Another issue for computing stress strain relationship is the sliding stress where each crack can slide backward is also different. Thus it is necessary to find out, at the certain applied stress, every crack status including stationary or sliding. Note some cracks may remain always open during loading and unloading.

From Kachanov et al (1994) and Lawn and Marshall (1998), the tangent modulus can be computed for many cracks. Assumed all crack can close under loading stress and slide during loading and unloading, before all the cracks close, the effective modulus is

$$\frac{d\sigma}{d\varepsilon} = \frac{E}{1 + \dfrac{3\pi\sum_i a_i \delta_i / A + 2\pi\sum_i (a_i - \delta_i)^2 \sin^2\theta_i / A}{1 - \pi\sum_i a_i \delta_i / A}} \tag{5.10}$$

And if all the cracks start to slide after their closure, the tangent modulus is

$$\frac{d\sigma}{d\varepsilon} = \frac{E}{1 + 2\pi\eta\sum_i a_i{}^2 \left(\sin^2\theta_i \cos^2\theta_i - \mu \sin^3\theta_i \cos\theta_i\right)/ A} \tag{5.11}$$

Bulk material modulus E can be achieved while all cracks remain stationary after unloading and once they slide backward, the more compliant modulus than loading can be calculated as

$$\frac{d\sigma}{d\varepsilon} = \frac{E}{1 + 2\pi\eta\sum_i a_i{}^2 \left(\sin^2\theta_i \cos^2\theta_i + \mu \sin^3\theta_i \cos\theta_i\right)/ A} \tag{5.12}$$

However, the solutions for tangent modulus during loading and unloading are only valid

for non-interacting cracks, and the coupling effects of neighboring cracks are not considered. Before cracks contact, Horii and Netmat-Nasser (1985) investigated the interaction between defects using so called 'method of pseudotractions'. Similar work was done by Tsukrov and Kachanov (1996) with Neumann-Schwarz alternating method. However, the interacting effects of neighboring cracks after the cracks contact and slide with friction are not available.

To derive the whole stress strain relation for a solid containing multiple cracks is beyond this paper, which will be investigated in future publication. Detail finite element model are carried out in the following to show the stress strain relation for solid containing many cracks with different crack density.

5.3.3 Finite Element Simulation of Stress Strain Relation

5.3.3.1 Single Crack

Detail finite element analysis is carried out to study the anelastic behavior of cracked materials. The crack in section 5.3.2.4 with δ/a = 1/200, a/L =0.632, θ=45^{o} and μ = 0.5 are chosen in simulation. The edge effect will occur if the crack length is too large compared to finite element model geometry which is 1×1m^2, and the Young's modulus and Poisson ratio are set as E=100GPa and ν=0.3. Uniaxial compression with maximum stress σ^{max} = -1.753GPa, which is the reaction stress from finite element model when the deformation is ε =2%, is loaded at x direction. The crack center is located at x=0.5 and y=0.5 in Cartesian coordinate system.

Figure 5.10 shows the stress strain behavior of the single crack from finite element modeling. Crack faces start to partially close at σ_c = -0.348GPa, which is a little smaller

than analytical solution (σ_c = -0.385GPa). After that, crack keep closing until fully contact at σ = -0.438GPa. The effective modulus at stage I is 0.722*E*. Then the crack begins to slide until the maximum compression with the slope of 0.925*E*. As soon as unloading begins, the direction of friction changes to the opposite direction. Then the crack faces remain stationary and the effective modulus is the same as the Young's modulus of material *E*. When the compression reduces to σ^{slid} = -0.869GPa, crack faces start to slide again with reduced modulus 0.803*E*. When the stress reaches contact pressure, crack faces open and stress strain follow the same path as loading process. The good agreement of finite element and analytical solutions is shown in Figure 5.10. Smooth curve is shown in finite element result compared with analytical one. Figure 5.11 shows tangent modulus at different stages during loading and unloading.

5.3.3.2 Multiple Cracks

Finite element method is used to study the interacting effects of microcracks during the whole loading and unloading process for different crack density. Figure 5.12 shows solids with many cracks. Crack density with 20% and 80% are chosen and crack length is set as *a/L* =0.2, crack aspect ratio is δ/a = 1/200, randomly orientated with θ varying from 0^o to 180^o, and friction coefficient is μ = 0.5. The position of every crack is arbitrarily located and none of cracks overlap each other. The stress strain relations are shown in Figure 5.13, and nonlinearity and hysteresis increase as the increasing of crack density but the solid becomes more compliant. Tangent modulus from finite element simulations and analytical solutions are shown in Figure 5.14 and Figure 5.15. It is clearly shown that the modulus from analytical solutions is different ones from finite element modeling since the analytical solutions do not cover the interacting effect of cracks. Figure 5.16 and

Figure 5.17 show the stress strain relation obtained from finite element modeling and analytical approximations. The sliding of some cracks before all crack close is not considered in analytical results.

5.4. Finite Element Model for Curvature Hysteresis

In order to study the anelastic behavior of YSZ coatings, suitable models under thermal cycles are carried out with finite element method. Scanning electron microscope (SEM) image is taken and it clearly shows lamella structure and the existence of pores and microcraks in Figure 5.18. In the simulation, cracks are embedded inside of coating according to the real microstructure, shown in Figure 5.19 with coating thickness is 730μm and substrate thickness is 3.3mm. We treated the interface of splats as microcracks. To simply the simulation, the pores and microcracks which have large crack aspect ratio (δ/a) are not considered because those defect cannot contact and slide during thermal cycle between room temperature and maximum temperature around 300^{o}C. Due to the difficulty of creating model with microstructure exactly same as real materials, more realistic structure with several layers of splats and microcracks nearly perpendicular to splat surfaces are embedded. Their positions are chosen arbitrarily and the angles between mircocracks along splats surface and spray directions remain from 60^{o} to 90^{o} according to the SEM measurements.

Based on the stress strain relation in section 5.3.1, we could estimate the aspect ratio with (5.32). E_c=39GPa and σ_1=-49MPa give the maximum aspect ratio is 1/400 or so. Then the modulus at room temperature E_c=39GPa is used in the following finite element models and the effect of pores and microcracks which have aspect ratio greater than 1/400 are covered with the reduced modulus E_c compared with bulk YSZ material.

The minimum crack length in this finite element model is 40 μm and the maximum crack opening is 0.1μm. In modeling, material properties are assigned with modulus E_c=39GPa and Poisson ratio ν =0.3 for coatings and E_c=70GPa, ν =0.3 for substrates. Figure 5.20 represents the symmetric boundary condition with length 1.0mm, which is applied to model an infinite (horizontally) plate.

Initially, the crack opening is set as 0.01μm and coefficient of friction for every crack is used with μ=0.5. The simulated curvature is shown in Figure 5.21. This plot shows clearly the hysteresis of coatings with many cracks and small nonlinearity because of the crack opening is not much. Figure 5.22 represents the effect of friction coefficient on anelastic behavior. Here the same value of friction coefficient for each crack is assumed. And it seems increasing the coefficient of friction hystereis decrease. It might be due to more crack remaining stationary status since frictional stress increases. From Figure 5.23, the Crack initial openings with 0.1μm can give hysteresis a little bit but shows large nonlinearity clearly. When crack openings decrease to 0.05μm after a certain applied compression, cracks starts sliding with internal friction which lead to anelastic mechanical response. With the decrease of crack openings until to 0.01μm, hysteresis becomes larger with less nonlinearity because microcracks will contact with smaller applied stress.

Until now, coating stress strain relation can be determined with three ways, one is estimated from curvature measurement, another one is determined from uniaxial loading and unloading directly shown in Figure 5.24 and the third one is from analytical solution. Based on the simulated curvature from finite element modeling during thermal cycle, coating stress strain relation can be estimated with the proposed material model and

procedure in chapter 3. One case for crack opening with 0.01μm and coefficient of friction with 0.5 was analyzed and simulated curvature is shown in Figure 5.21. Coating property during heating are E_c=35GPa, σ_N =133.7MPa, n=2.45 and σ_T =-77MPa. And during cooling since crack opening is very small, so the cooling curvature is almost straight and all cracks close at very small stress, so nonlinearity is shown only at small region during cooling. The coating properties is simply calculated with linear elastic modulus E_c=27GPa. The anelastic stress strain behavior during heating and cooling is plotted in Figure 5.25. Compressive loading is applied in the uniaxial model and the effective property and stress strain behavior can be determined. Figure 5.25 shows the coating stress strain relation from simulated curvature measurement, uniaxial model and also analytical solution. Since the interacting effect is not included in the analytical solution, the stress strain curve shows a little different with the other two. Such effect will be studied in future work.

5.5. Conclusions

Anelastic stress strain behaviors thermally sprayed YSZ coatings are studied by substrate curvature measurements, numerical analysis and finite element simulations. The present study confirmed the anelastic behavior come from microcracks open/closing and their surfaces sliding with internal friction. With different crack density, anelastictity including nonlinearity and hysteresis would be various. Therefore, coatings with different microstructures lead to different anelastic stress strain response. As we know, the defect architectures of coatings are strongly related to the complex deposition processes and related processing conditions. Feedstock powder and processing conditions of particles all affect the nature of the deposit formation dynamics and the ensuing properties of

coatings. Thus, different anelastic behavior with the various coating microstructure can be controlled with feedstock properties and processing conditions.

5.6. References

Basista, M.and Gross, D., (1998), "The sliding crack model of brittle deformation: An internal variable approach", *International Journal of Solids and Structures,* 35 (5-6) 487-509.

Emel'lyanov, Y., Golyandin, S., Kobelev, N. P., Kustov, S., Nikanorov, S., Pugachev, G.., Sapozhnikov, K., Sinani, A., Soifer, Y. M., Humbeeck, J.V., Batist, R.D. (2000), "Influence of high-energy impact actions on the elastic and anelastic properties of martensitic Cu–Al–Ni crystals", *Journal of Alloys and Compounds*, 310 (1-2) 324-329.

Harok, V. and Neufuss, K., (2001), "Elastic and inelastic effects in compression in plasma-sprayed ceramic coatings", *Journal of Thermal Spray Technology* 10 (1), 126-132.

Horri, H. and Nemat-Nasser, S. (1985). "Elastic fields of interacting inhomogeneities", *International Journal of Solids and Structures,* 21 (7), 731-745.

Kachanov, M., Tsukrov I. and Shafiro, B., (1994), "Effective moduli of solids with cavities of various shapes", *Applied Mechanics reviews* 47 (1), 151-174.

Kroupa, F. and Dubsky, J., (1999), "Pressure dependence of Young's Moduli of thermal sprayed materials", *Scripta Materialia,* 40 (11), 1249-1254.

Kroupa F. and Plesek, J., (2002), "Nonlinear elastic behavior in compression of thermally sprayed materials", *Materials Science and Engineering* A, 328 (1-2) 1-7.

Lauterbach B., and Gross, D., (1998), “Crack growth in brittle solids under compression”, *Mechanics of Materials* 29 (2), 81-92.

Lawn, B. R. and Marshall, D. R., (1998), “Nonlinear stress-strain curves for solids containing closed cracks with friction”, *Journal of the Mechanics and Physics of Solids* 46 (1), 85-113.

Li, J. F., Liao, H., Wang, X. Y., Normand, B., Ji, V., Ding C. X. and Coddet, C., (2004), “Improvement in wear resistance of plasma sprayed yttria stabilized zirconia coating using nanostructured powder”, *Tribology International.,* 37 (1) 77-84.

Matejicek J. and Sampath, S., (2003), “In situ measurement of residual stresses and elastic moduli in thermal sprayed coatings: Part 1: apparatus and analysis”, *Acta Materialia,* 51 (3) 863-872.

Muskhelishvili, N.I., (1953), “Some basic problems of the mathematical theory of elasticity”. *Noordhoff, Groningen.*

Nemat-Nasser, S.and Obata, M., (1988), “A microcrack model of dilatancy in brittle materials”, *Journal of Applied Mechanics* 55 (1) 24-35.

Niemeyer, T. C., Grandini, C. R., and Florêncio, O., (2005), “Stress-induced ordering due heavy interstitial atoms in Nb–0.3 wt.% Ti alloys”, *Materials Science and Engineering A*, 396 (1-2) 285-289.

Ouyang, J. H. and Sasaki, S., (2001), “Unlubricated friction and wear behavior of low-pressure plasma-sprayed ZrO_2 coating at elevated temperatures”, *Ceramics*

International, 27(3), 251-260.

Pan, L.S., Imai, N. and Horibe, S., (1997), "Temperature dependence of anelastic behavior in 3Y-TZP ceramics", *Materials Science and Engineering A*, 230 (1-2) 155-160.

Pan, L.S. and Horibe, S., (1997), "Anelastic behaviour of zirconia ceramics under monotonic and cyclic loadings", *Acta Materialia*, 45 (2) 463-469.

Tsukrov, I and Kachanov, M., (1997), "Stress concentrations and microfracturing patterns in a brittle-elastic solid with interacting pores of diverse shapes", *International Journal of Solids and Structures*, 34(22), 2887-2904.

Waki, H., Ogura, K., Nishikawa I. and Ohmori, A., (2004), "Monotonic and cyclic deformation behavior of plasma-sprayed coatings under uni-axial compressive loading", *Materials Science and Engineering* A, 374 (1-2), 129-136.

Walsh, J. B., (1965), "The effect of cracks on the compressibility of rocks", *Journal of Geophysical Research,* 70(2), 381-389.

Walsh, J. B., (1965), "The effect of cracks on uniaxial compression of rocks", *Journal of Geophysical Research,* 70(2), 399-411.

Wang, W., Li, C., Wang, Y., Yang, G., Sonoya, K., (2006), "Tensile deformation behavior of plasma-sprayed Ni-45Cr coatings", *Surface and Coatings Technology* 201(3-4), 842-847.

Yagmur, L., Fank S. and Aydemir, B., (2007) "Effect of microstructure on modulus loss at flexural mode and stress in sensor materials", *Sensors and Actuators A: Physical*, 136(1), 261-266.

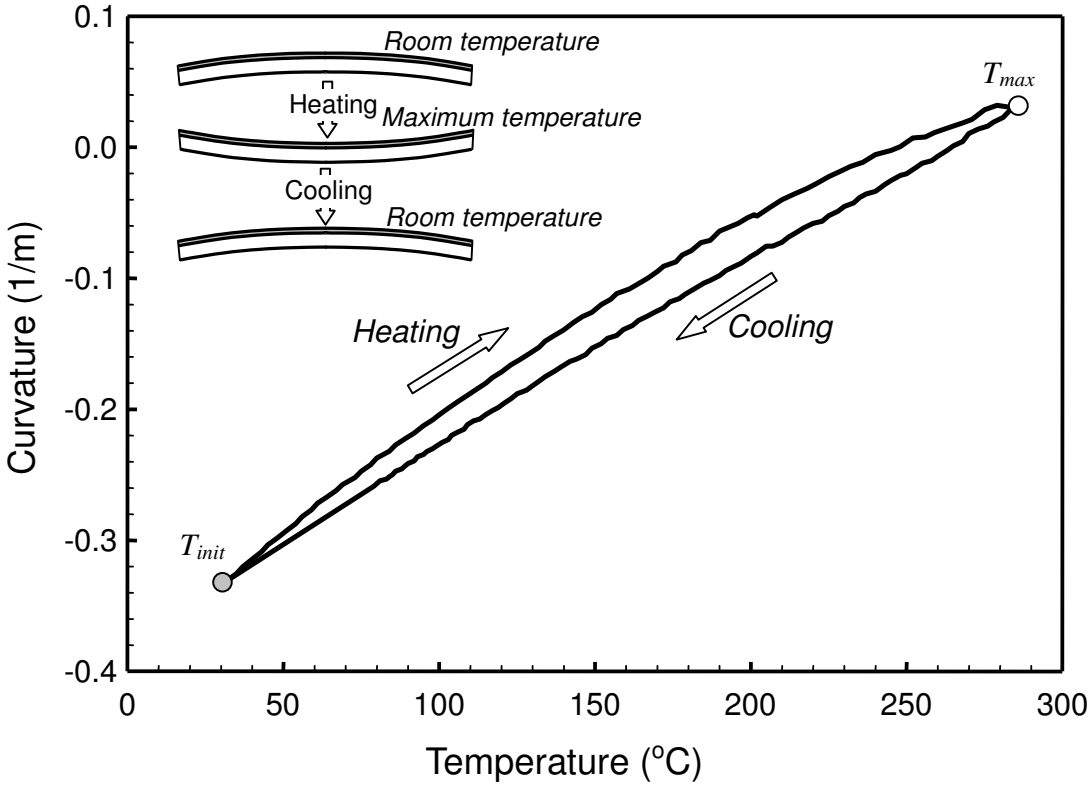

Figure 5.1. Cyclic curvature measurement by surface profilometer during thermal cycle. Here T_{init} and T_{max} represent initial and maximum temperature.

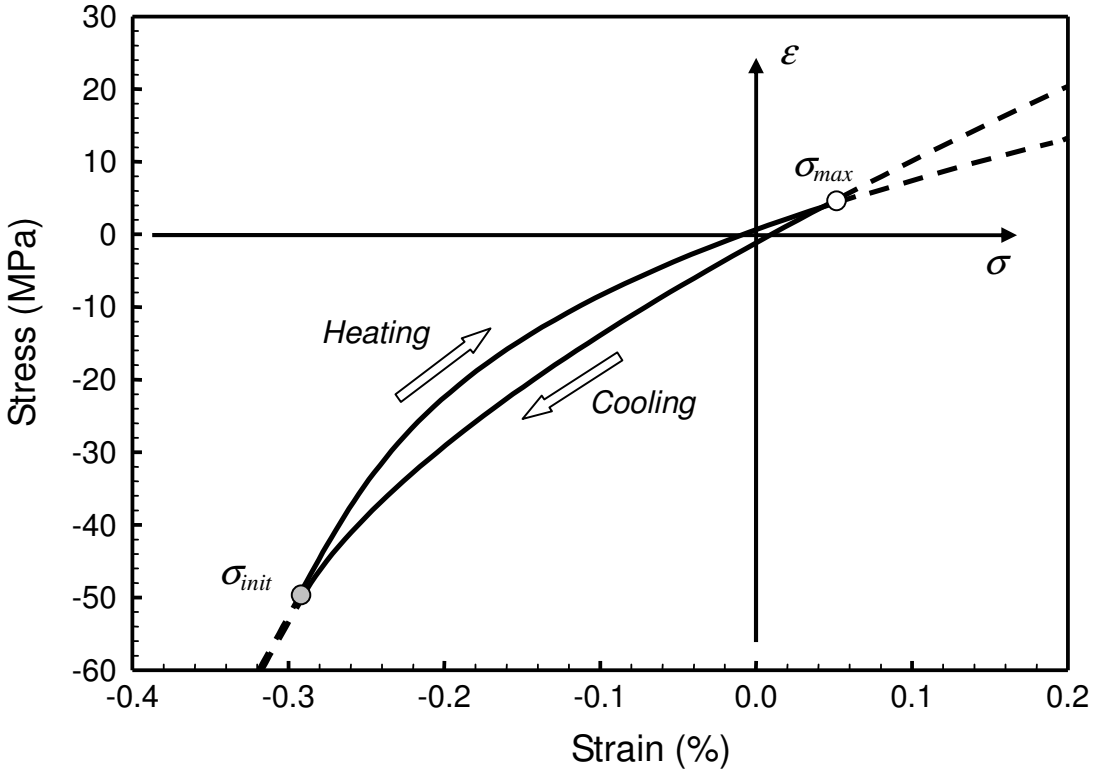

Figure 5.2. Stress strain relation showing nonlinearity and hysteresis. Here σ_{init} and σ_{max} represent stresses at T_{init} and T_{max}.

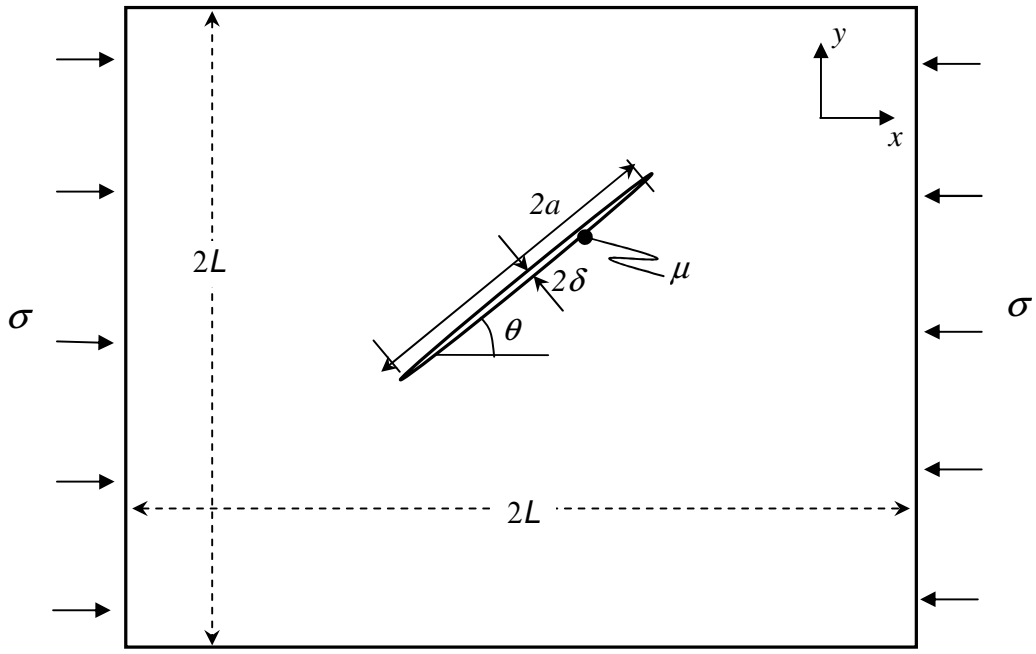

Figure 5.3. Solid ($2L \times 2L$) containing single crack subjected to compression. The crack is characterized by its length a, orientation θ, opening δ and coefficient of friction μ.

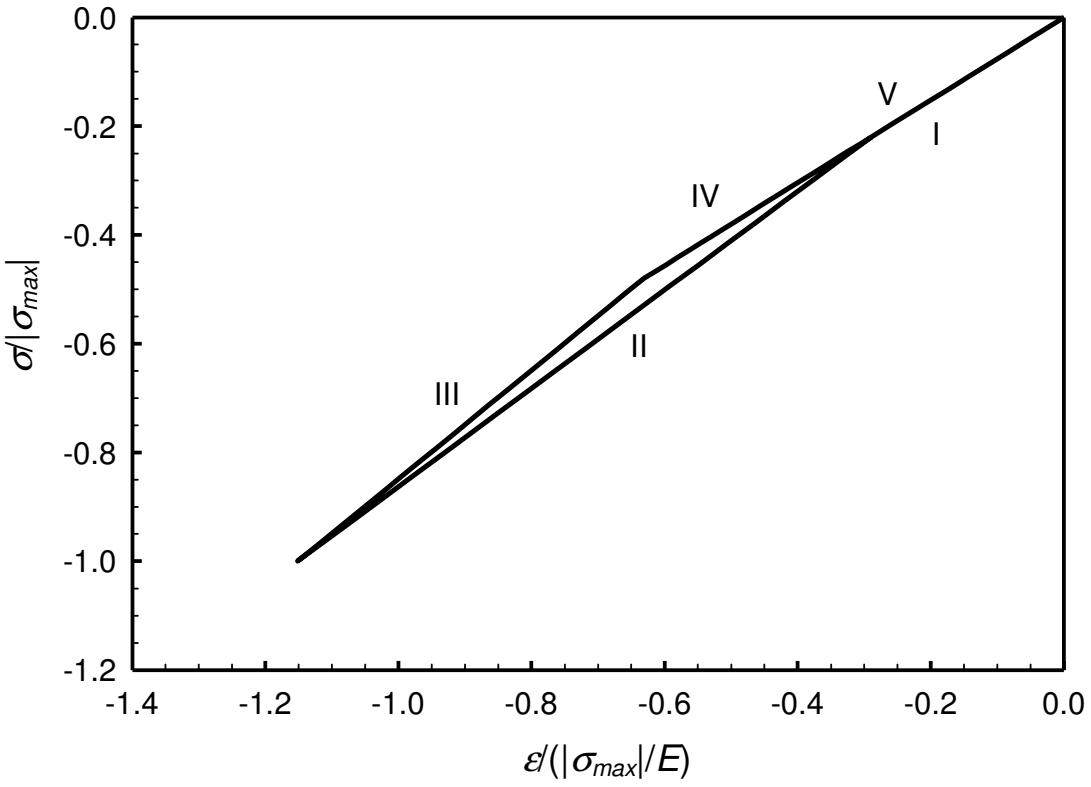

Figure 5.4. Stress strain relations of single crack with δ/a =1/200, θ=45°, a/L=0.632, μ=0.5.

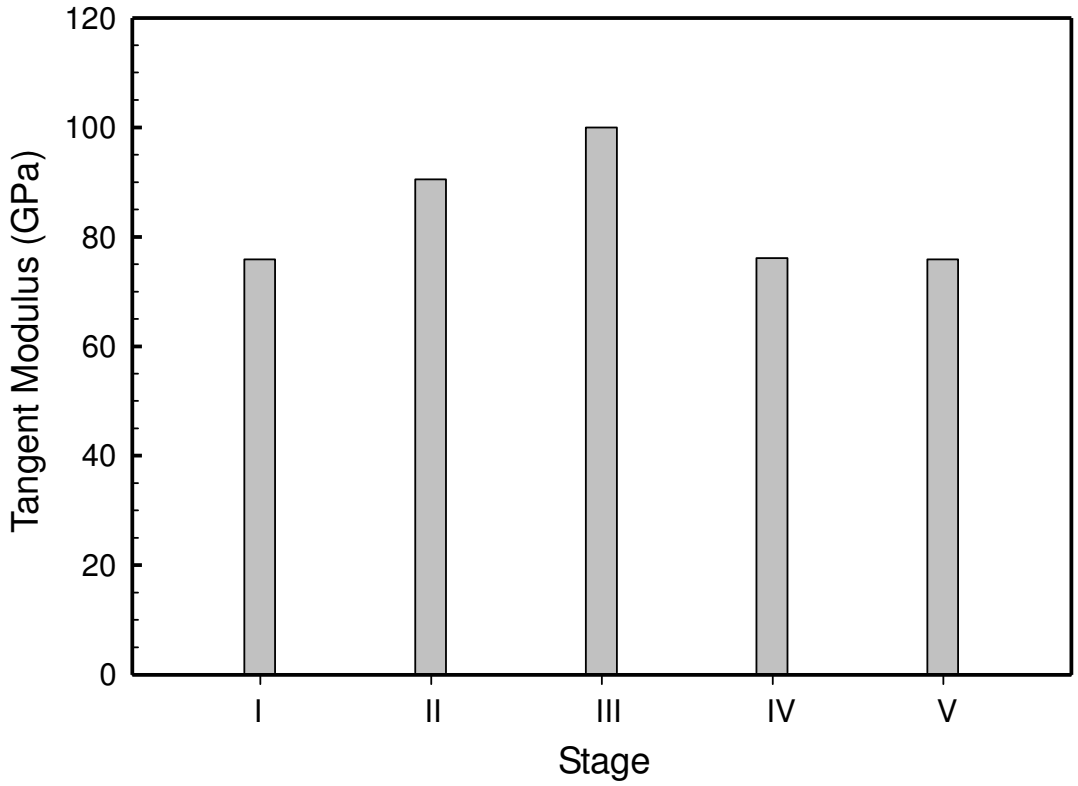

Figure 5.5. Tangent modulus during loading and unloading of single crack with δ/a =1/200, θ=45°, a/L=0.632, μ=0.5.

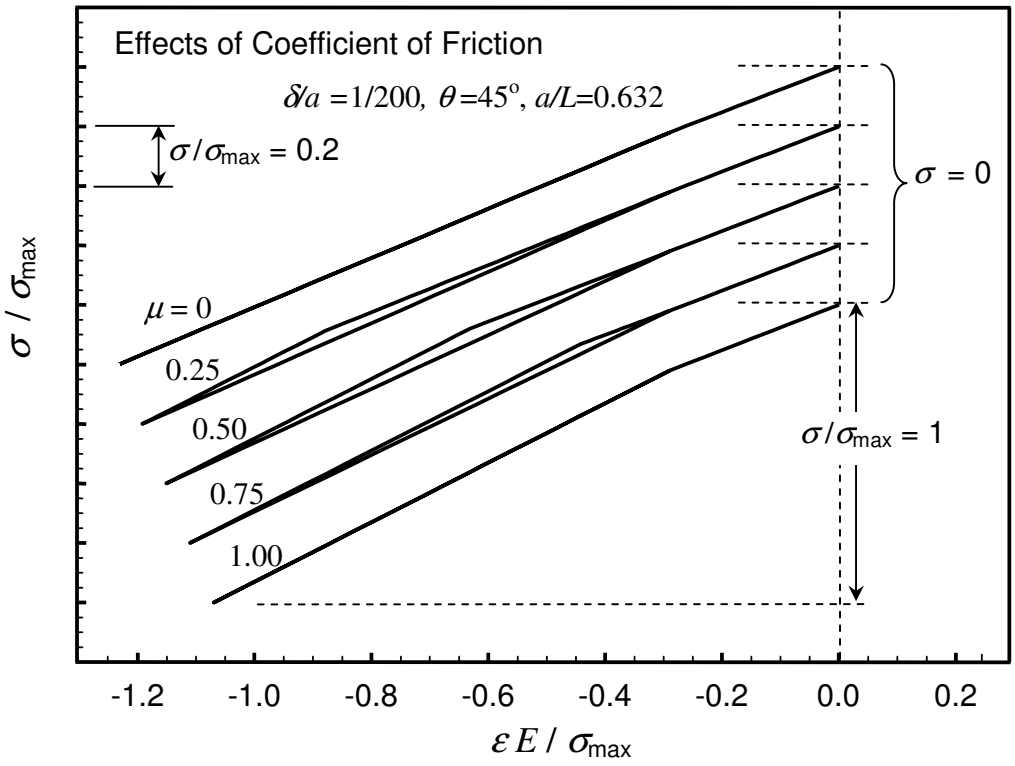

Figure 5.6. Stress strain relations of single crack with different coefficient of frictionμ.

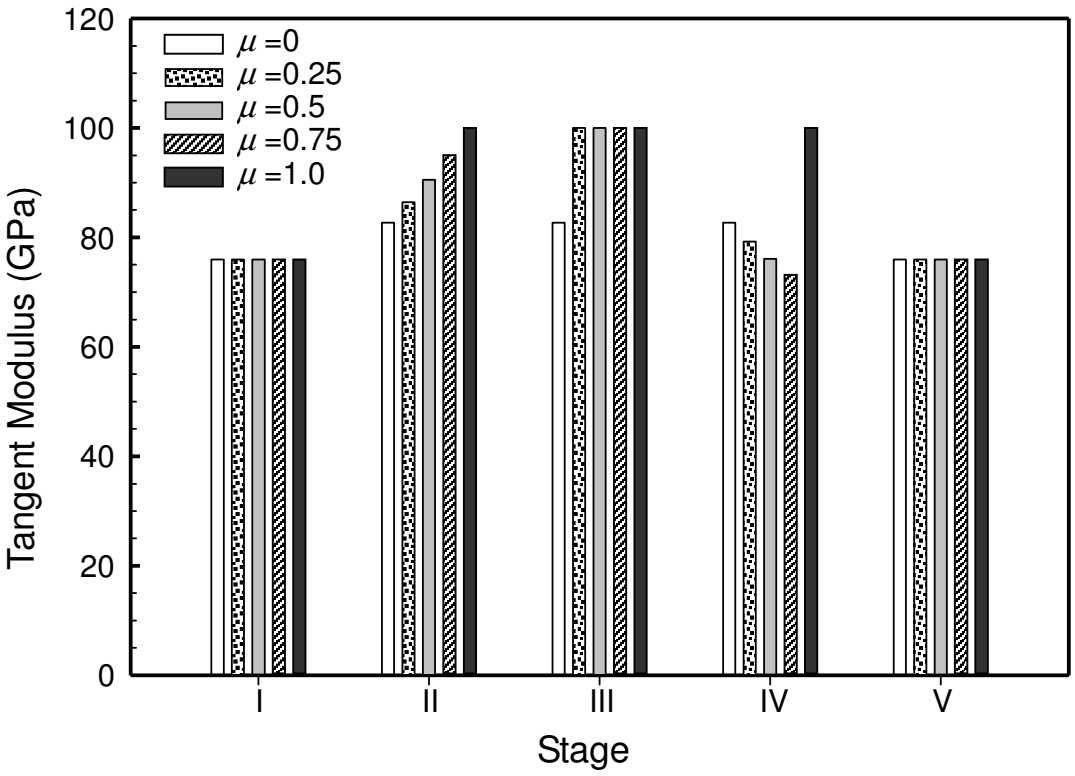

Figure 5.7. Tangent modulus during loading and unloading of single crack with different coefficient of frictionμ.

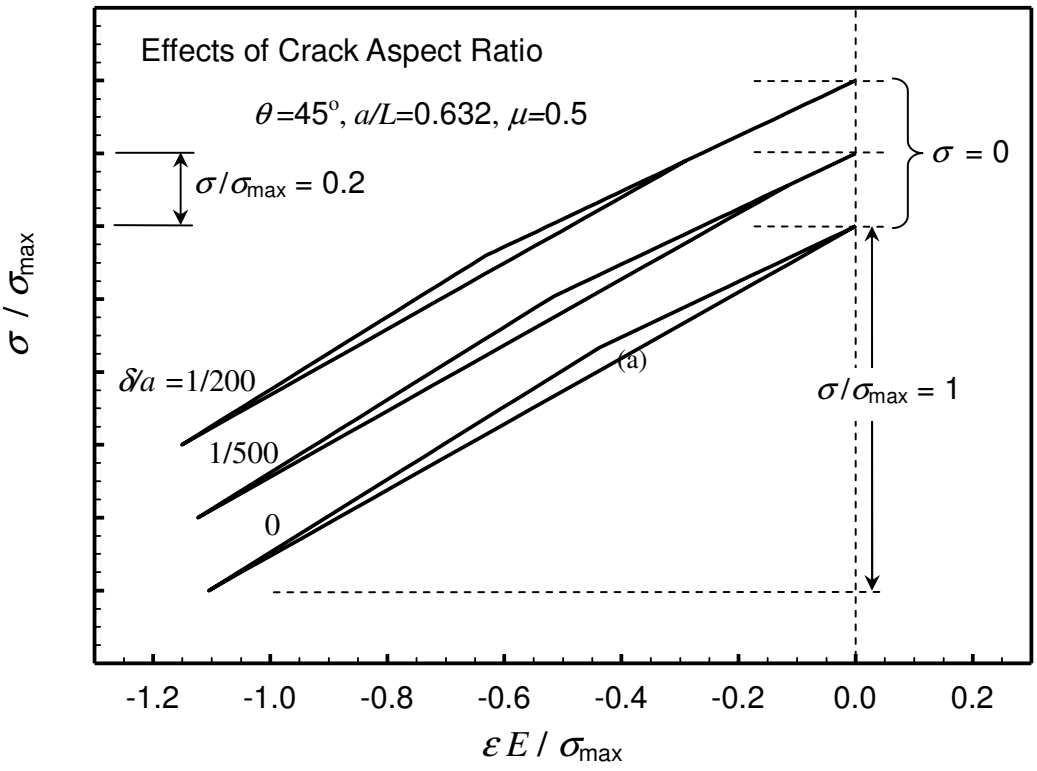

Figure 5.8. Stress strain relations of single crack with different crack aspect ratio fixed δ/a.

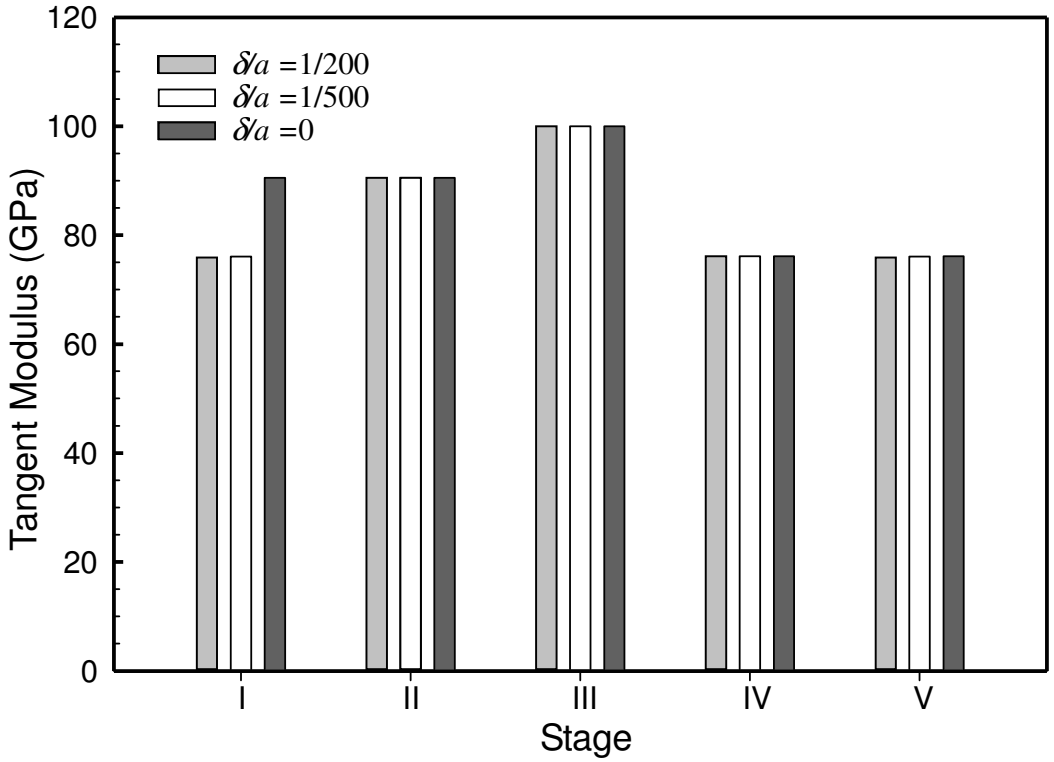

Figure 5.9. Tangent modulus during loading and unloading of single crack with different crack aspect ratio fixed δ/a.

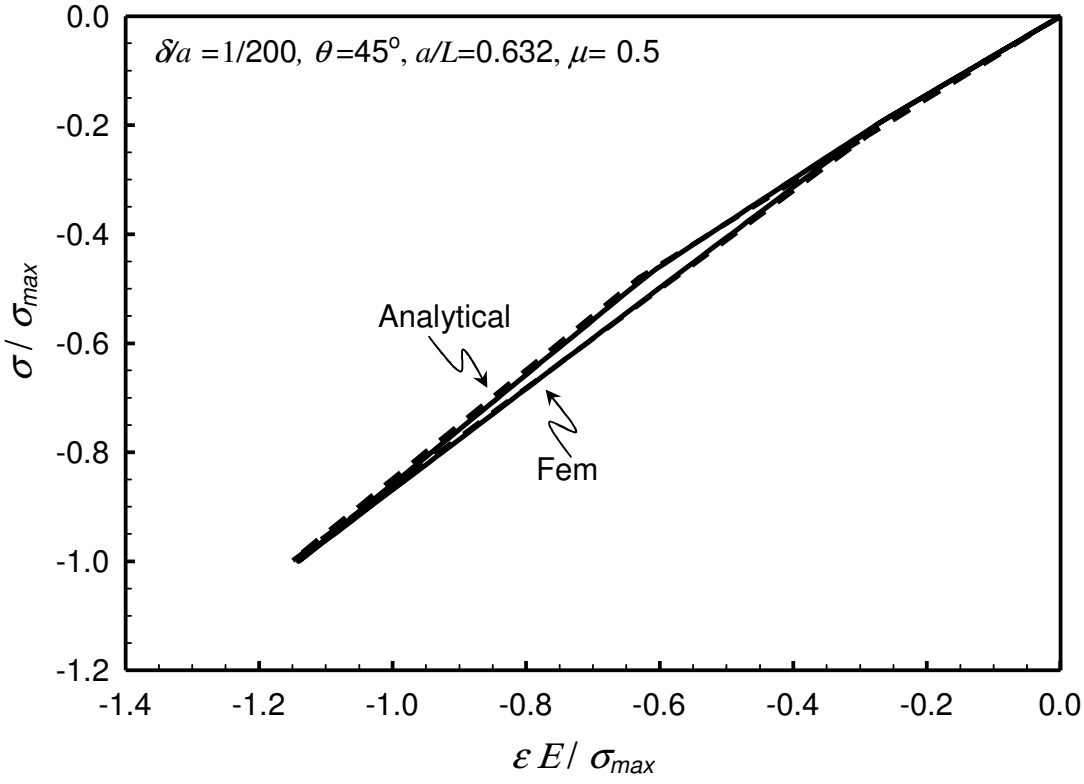

Figure 5.10. Stress strain relations of single crack of finite element modeling compared with analytical solution.

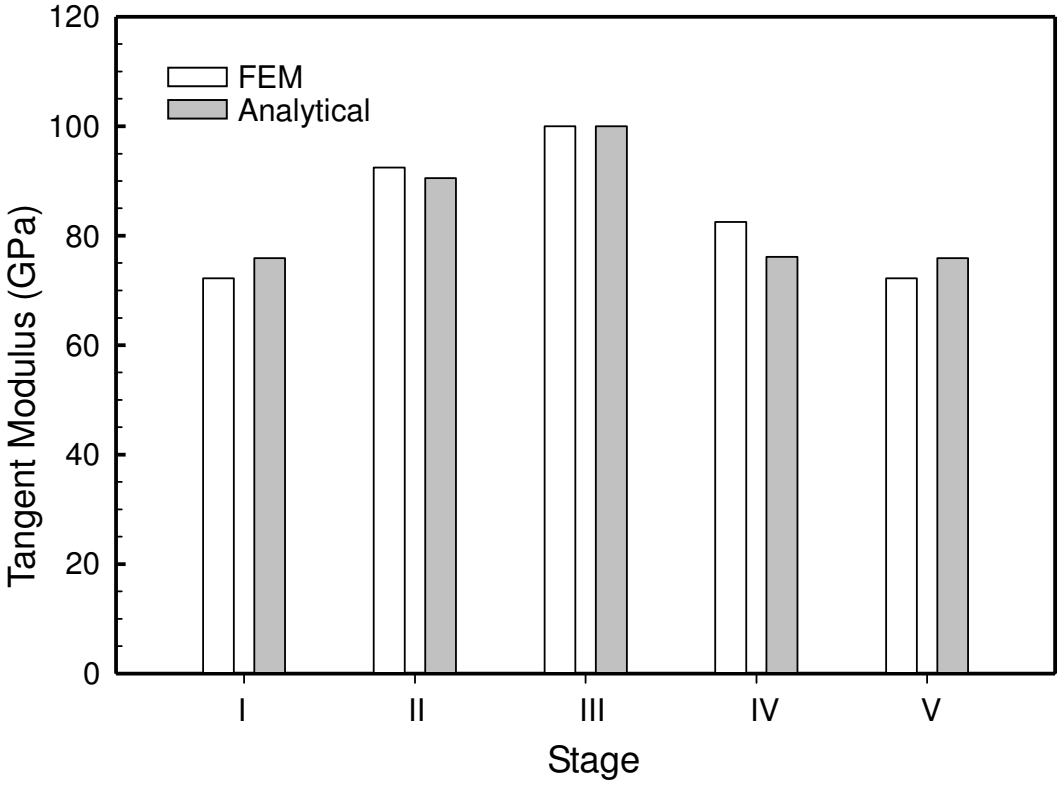

Figure 5.11. Tangent modulus during loading and unloading of single crack of finite element modeling compared with analytical solution.

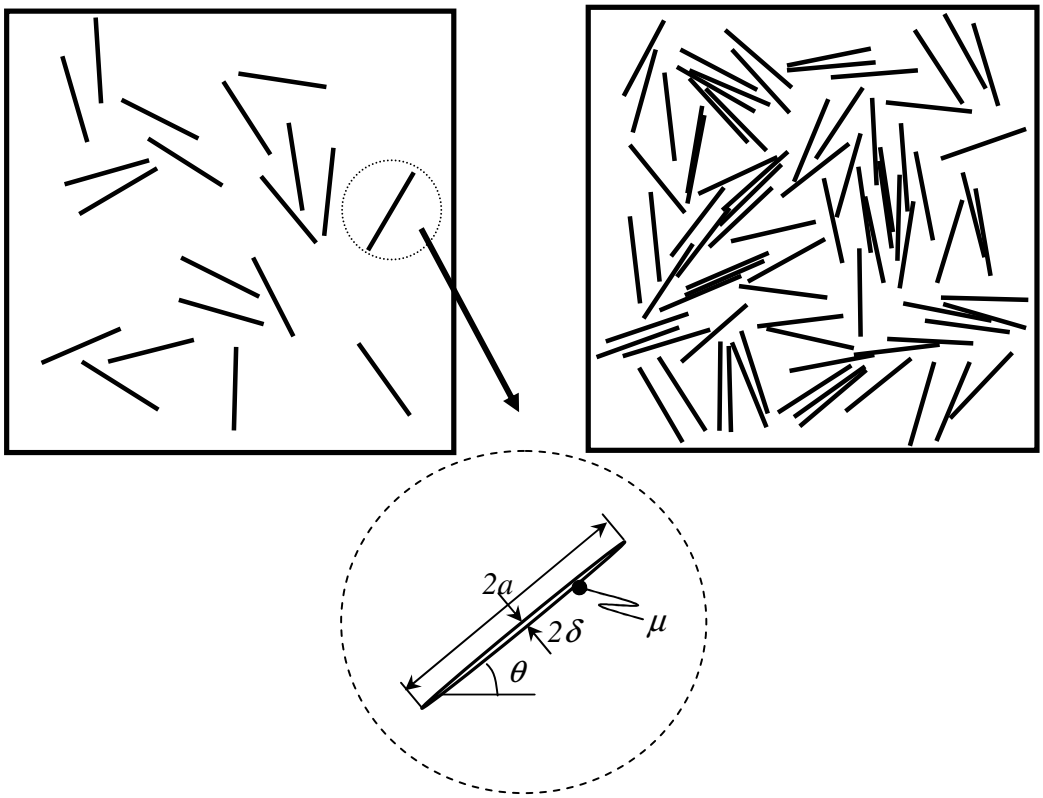

Figure 5.12. Schematic of solids containing 20 and 80 interacting cracks subjected to compression.

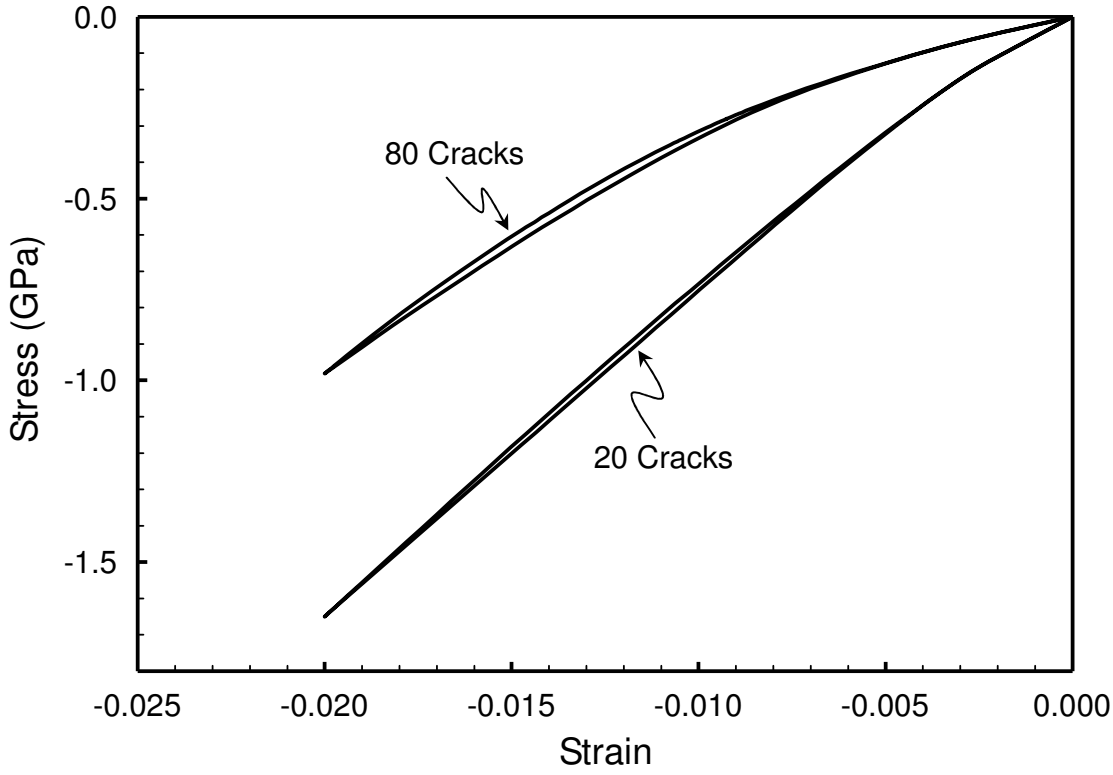

Figure 5.13. Stress strain relations of solids containing 20 and 80 interacting cracks subjected to compression.

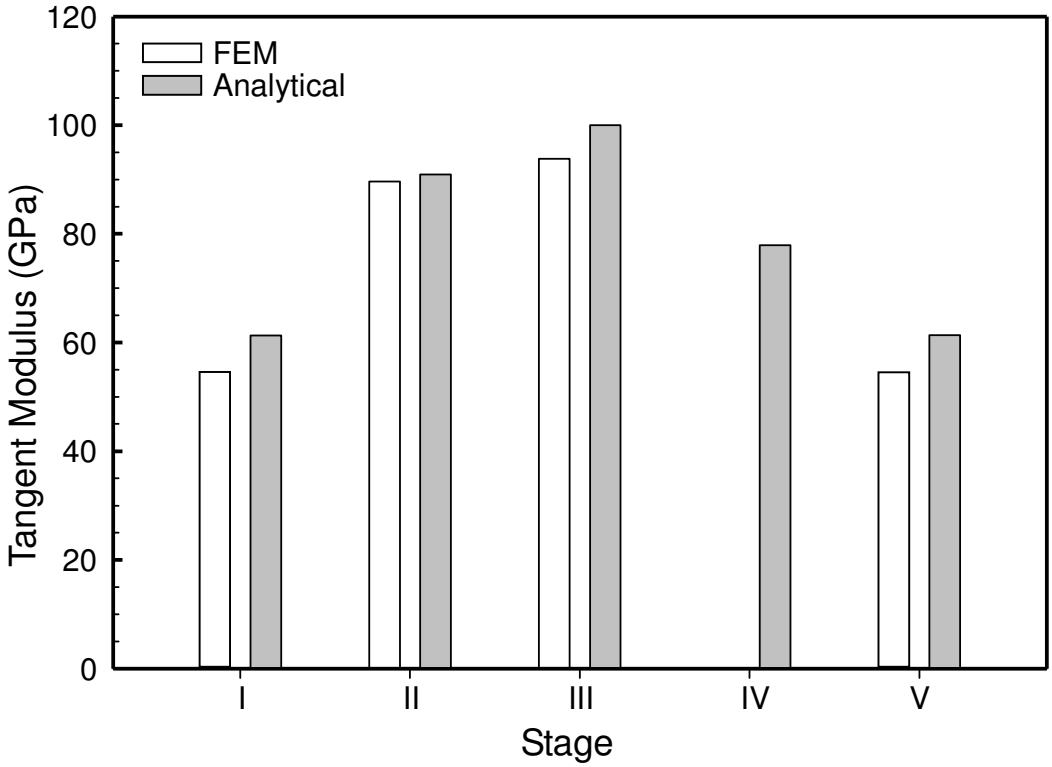

Figure 5.14. Tangent modulus during loading and unloading for 20 cracks.

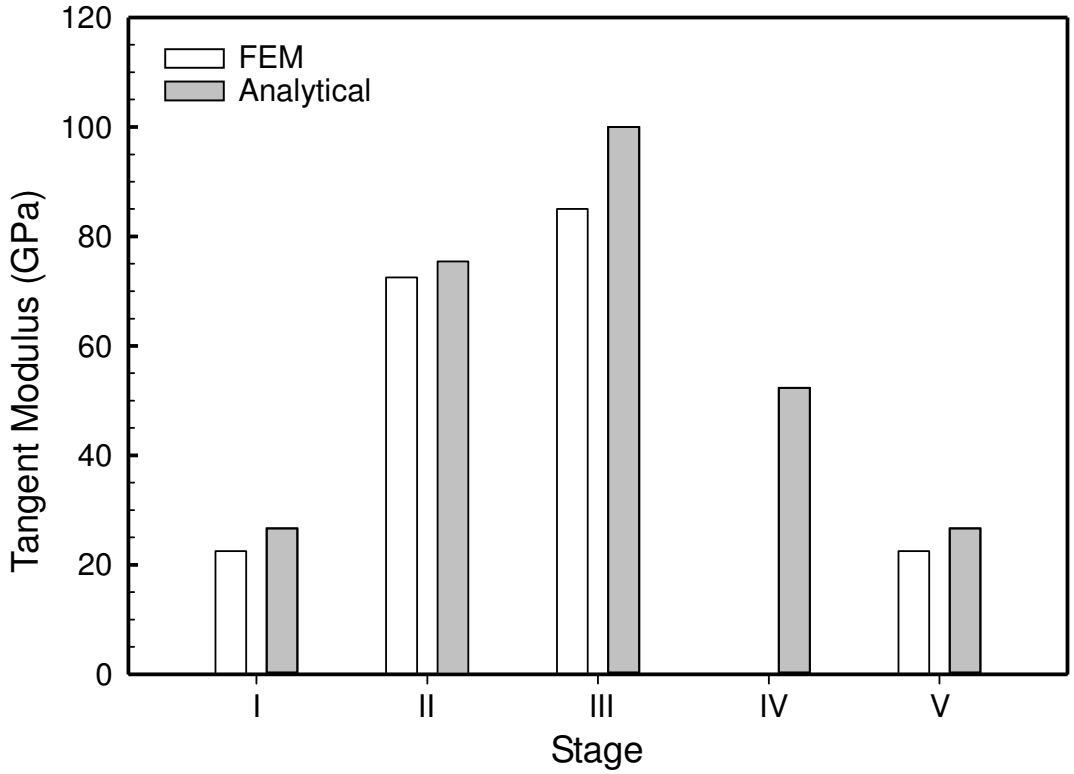

Figure 5.15. Tangent modulus during loading and unloading for 80 cracks.

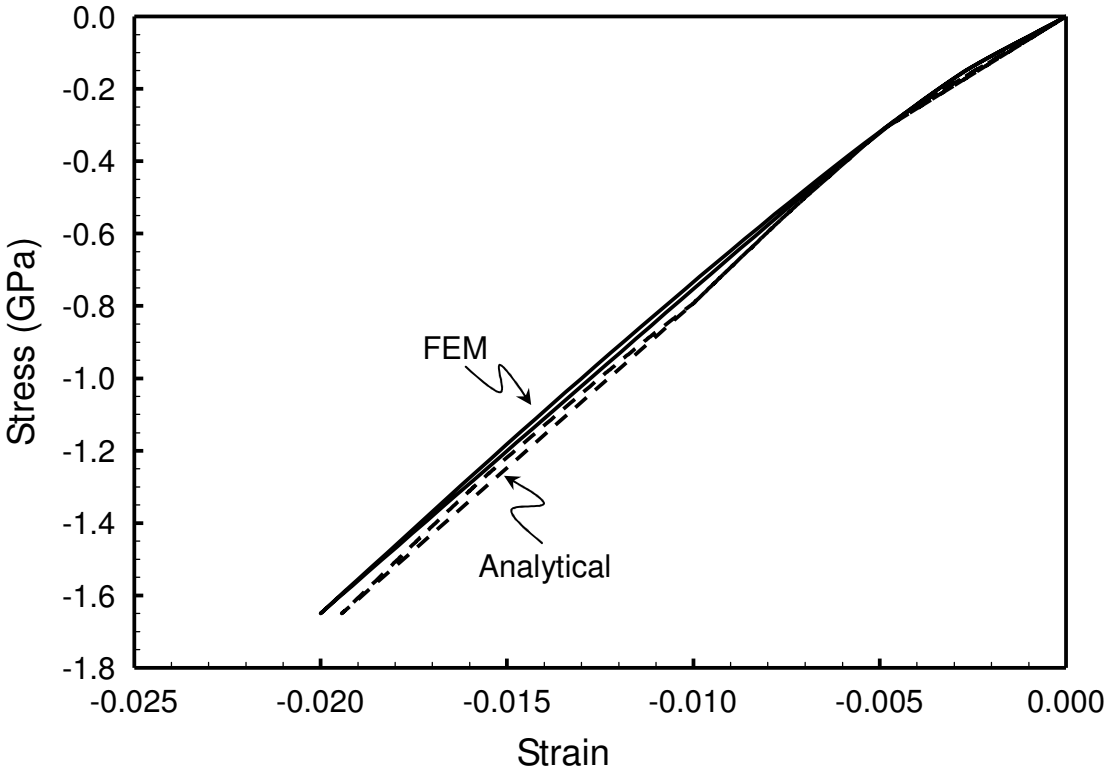

Figure 5.16. Stress strain relations of 20 cracks of finite element modeling compared with analytical solution.

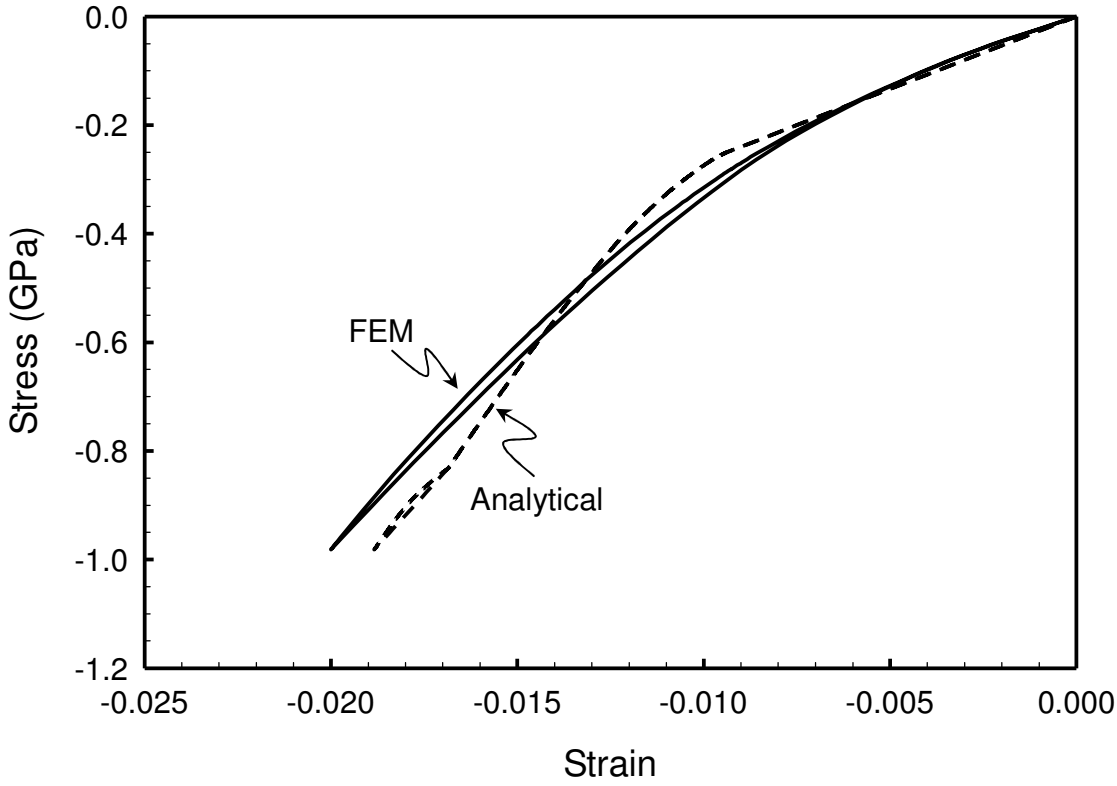

Figure 5.17. Stress strain relations of 80 cracks of finite element modeling compared with analytical solution.

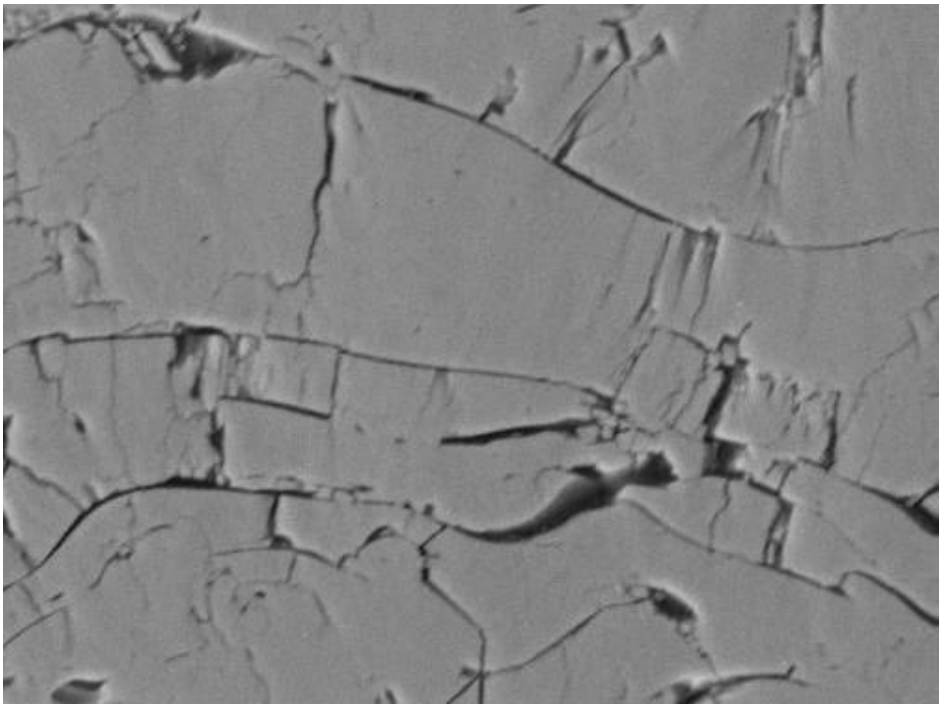

Figure 5.18. Scanning electron microscope (SEM) image of thermal spray coating.

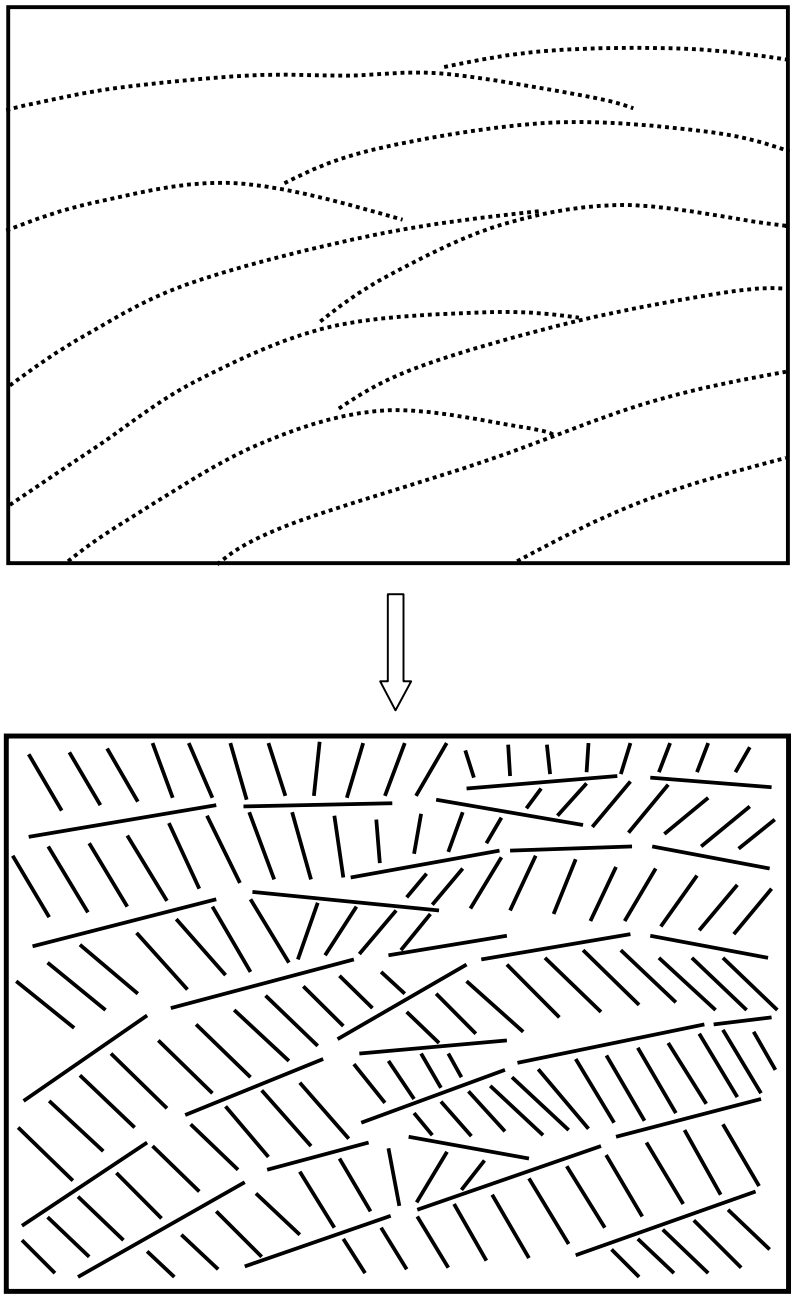

Figure 5.19. Coating containing randomly oriented cracks. Each crack is characterized by its length a, orientation θ, opening δ and coefficient of friction μ.

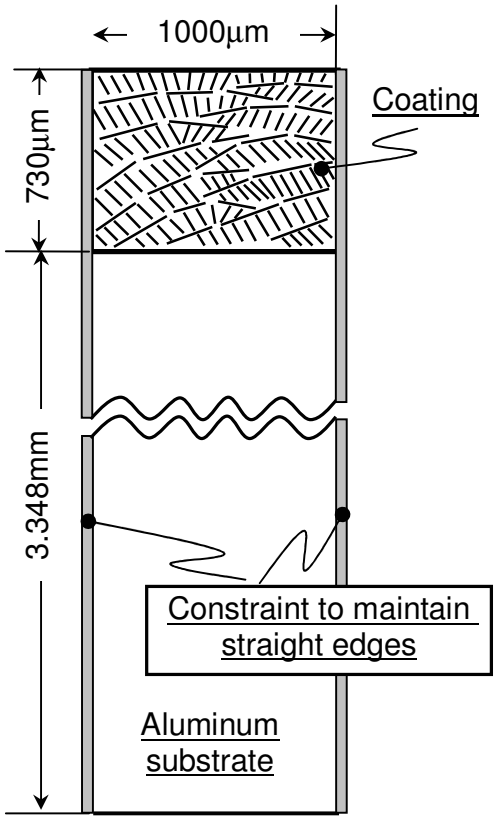

Figure 5.20. Schematic of idealized model with embedded cracks in coating. Symmetric boundary condition is prescribed to represent an infinite (horizontally) plate.

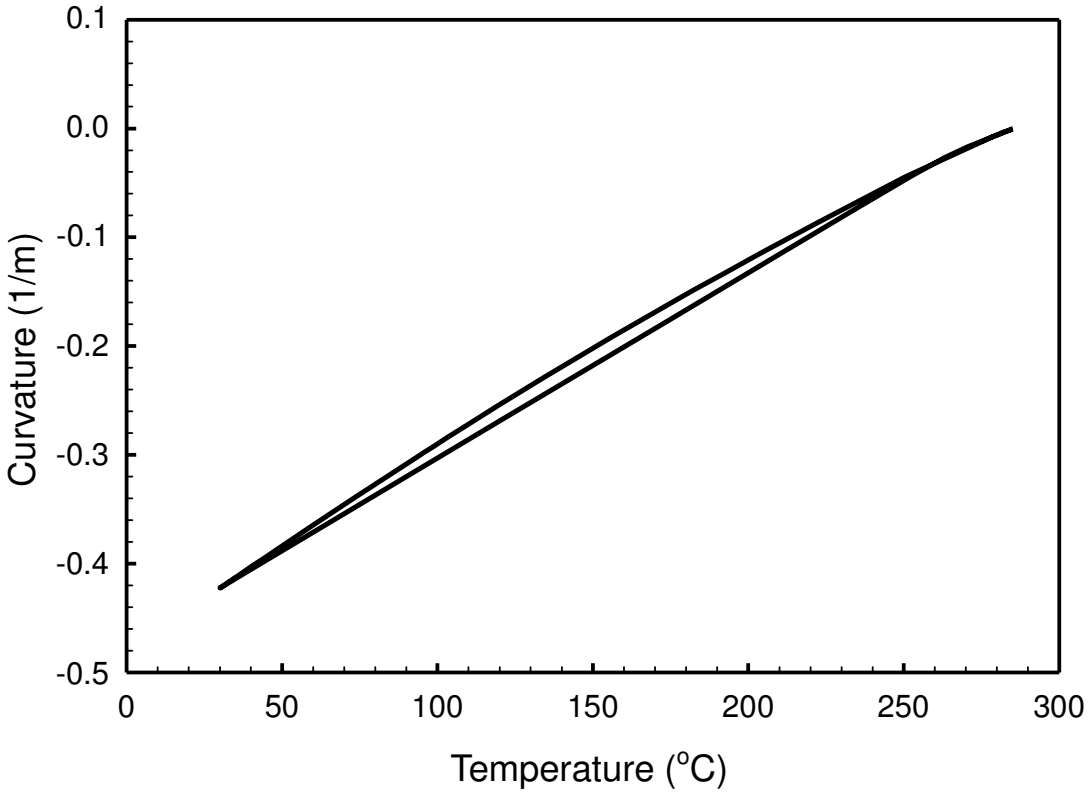

Figure 5.21. Artificially generated cyclic hysteresis and nonlinear behavior of multiple crack models with frictions. All cracks have opening (δ= 0.01μm) and friction (μ = 0.5).

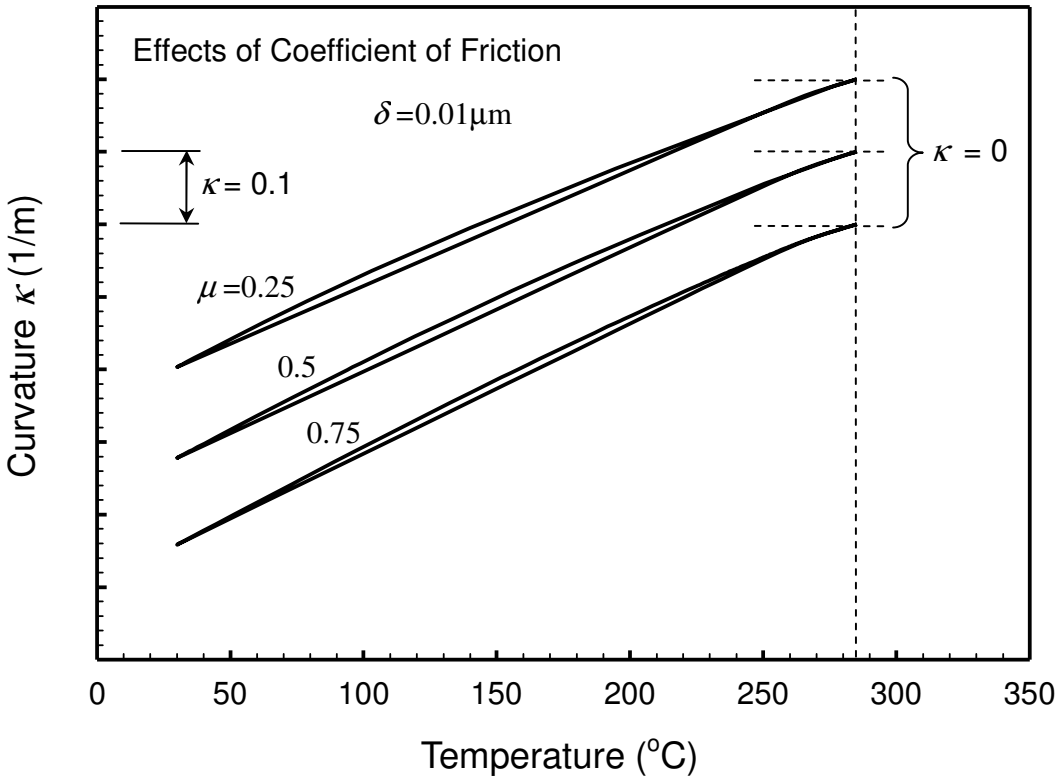

Figure 5.22. Artificially generated cyclic hysteresis and nonlinear behavior of multiple crack models with frictions. All cracks have same opening (δ= 0.01μm) but different coefficient of frictionμ.

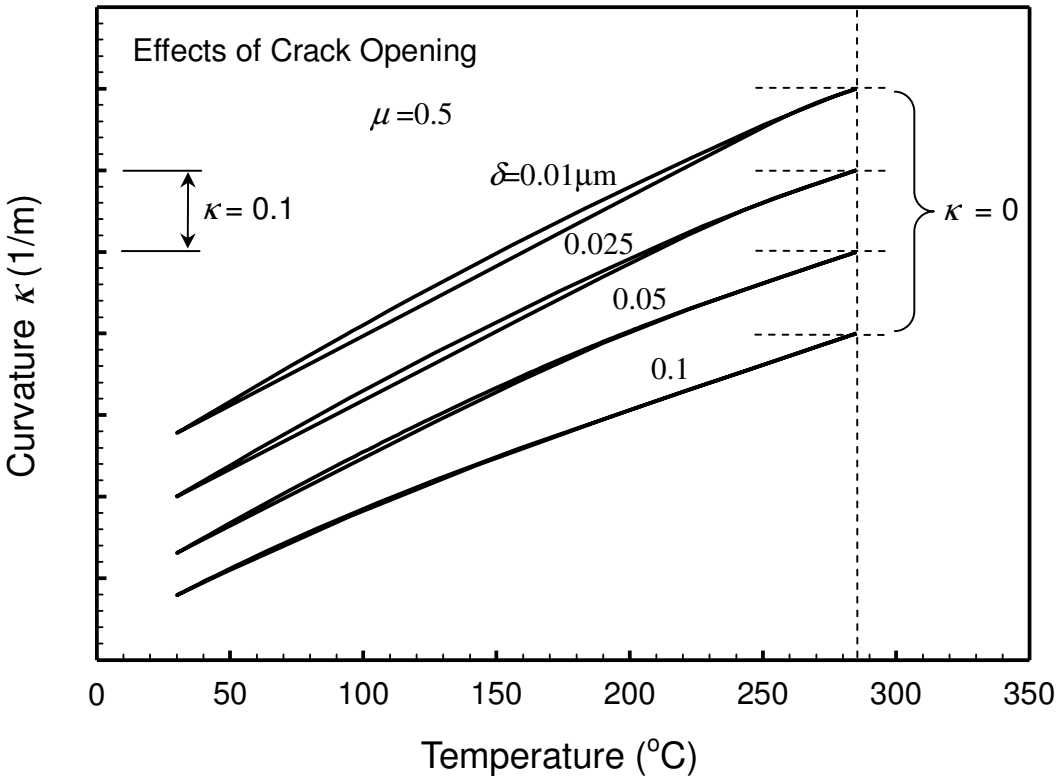

Figure 5.23. Artificially generated cyclic hysteresis and nonlinear behavior of multiple crack models with frictions. All cracks have same friction coefficient μ=0.5 but different crack opening δ.

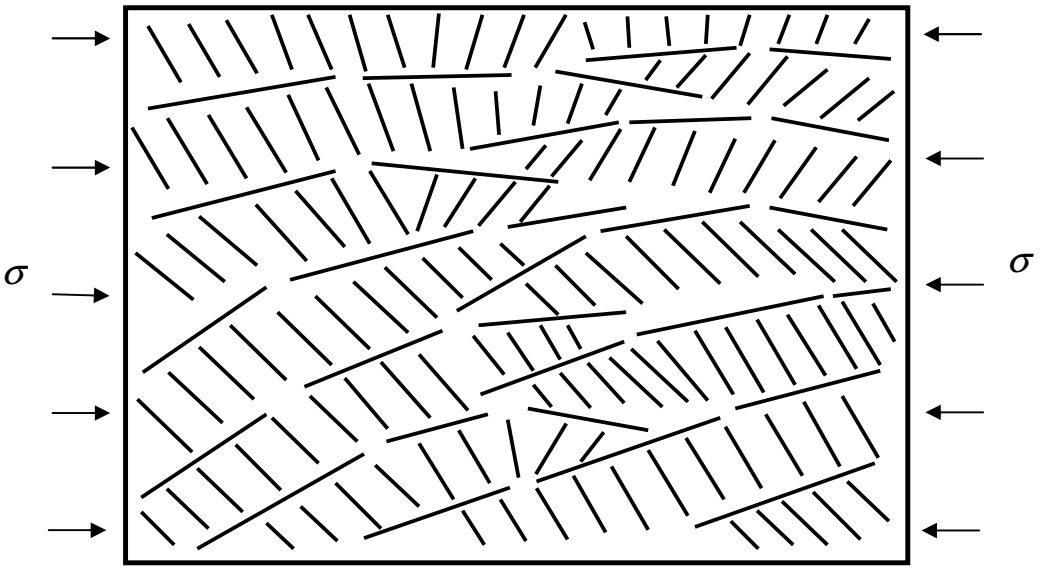

Figure 5.24. Schematic of coating under uniaxial loading with compression.

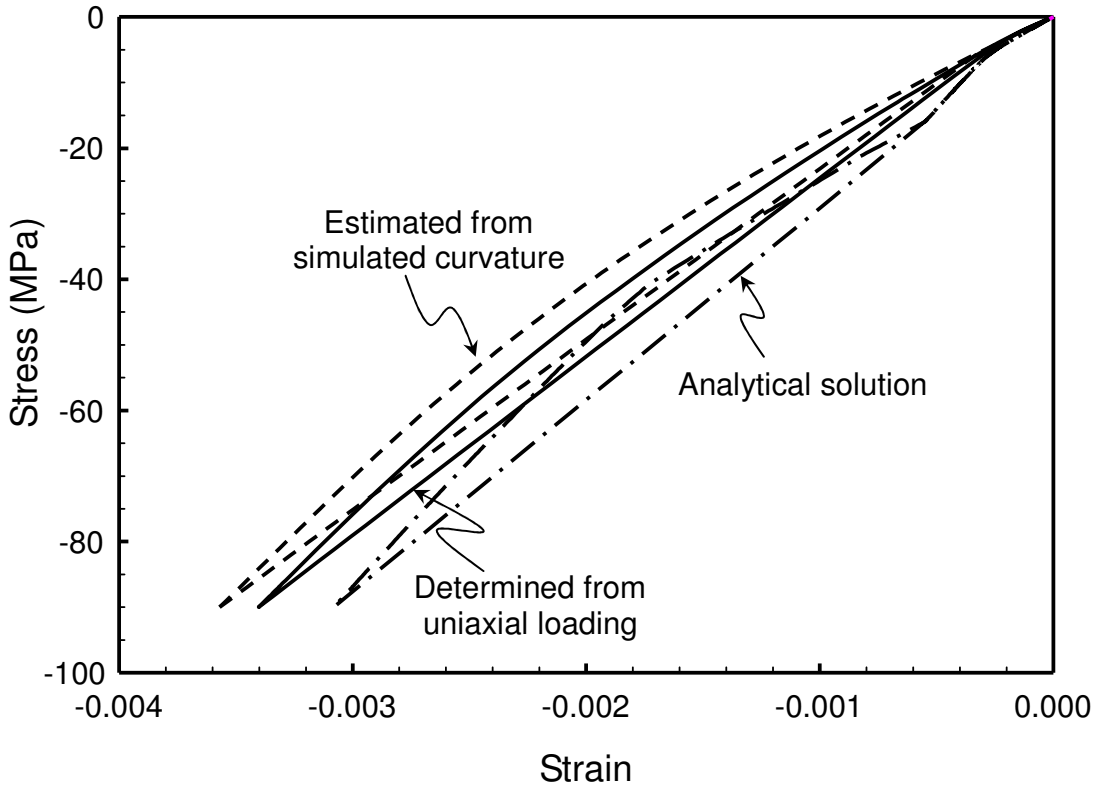

Figure 5.25. Anelastic stress strain behavior determined from simulated curvature, uniaxial loading and analytical solution for all crack with opening (δ= 0.01μm) and friction (μ = 0.5).